ScuDo
Scuola di Dottorato ~ Doctoral School
WHAT YOU ARE, TAKES YOU FAR

Doctoral Dissertation
Doctoral Program in Electical Electronic and Communication Engineer (30^{th}cycle)

Tooth-coil wound multiphase synchronous machines

By

Michela Diana

******

Supervisor(s):
Prof. P. Guglielmi, **Supervisor**
Prof. Emer. A. Vagati, **Mentor**

Doctoral Examination Committee:
Prof. Leila Parsa , Referee, University of California Santa Cruz
Prof. Francesco Cupertino, Referee, Politecnico di Bari
Prof. Carlo Concari, Università degli Studi di Parma
Prof. Michele A. Pastorelli, Politecnico di Torino
Prof. Eric G. Armando, Politecnico di Torino

Politecnico di Torino
2018

Declaration

I hereby declare that, the contents and organization of this dissertation constitute my own original work and does not compromise in any way the rights of third parties, including those relating to the security of personal data.

Michela Diana
2018

* This dissertation is presented in partial fulfillment of the requirements for **Ph.D. degree** in the Graduate School of Politecnico di Torino (ScuDo).

I would like to dedicate this thesis to my loving family

Acknowledgements

The author would like to express a special thanks to Emeritus Professor Alfredo Vagati for his mentor-ship.

The author would like to thanks the ASKOLL Holding s.r.l. company, Italy, that helped the Author in the realization of the 9-phase electric machine prototype.

Abstract

Nowadays we are witnessing a strong growth in the full electric vehicle market. In the field of traction the requirements are low weight, small dimensions and low cost, without renouncing reliability and good performances. The high power density requirement is pushing the research towards integrated drive solutions. A particular drive that allows to obtain more insightful integrated solutions is the multi-phase one. In fact, in multi-phase structures it is possible to realize a converter as a combination of standard modules with an equal subdivision of the current. The resulting power electronics modules meet the needs of an integrated solution: smaller and widely distributed.

Although road electric vehicles primarily adopt 3-phase drives, the multi-phase version could represent a good alternative not only for its integration capability but also for other features like reduced weight and volume, high efficiency, low vibrations and noise, robustness and, overall, fault tolerance. The aim of this thesis is to investigate a particular category of multiphase machines, characterized by a very simple structure that allows to match manufacturing and performance standards.

In **Chapter 1**, the subcategory of multiphase machine object of the investigation is identified. Considering a simple stator structure, as the tooth-coil wound, a general algorithm to identify the right stator-rotor coupling in multiphase machine is presented.

In **Chapter 2**, an analytical and generalized formulation of the harmonic fields at the air gap for the multi-n-phase solutions chosen is reported allowing to understand and quantify the harmonic compensation in the MMF. Starting from the Lorenz Force Law an analytical formulation of the torque and torque ripple is then proposed. The model proposed has been then verified by Finite Element Analysis (FEA).

In **Chapter 3**, the main issues tackled in the design of a nine phase machine are reported. Between the possible solutions a 9 slot 10 poles PM-inset machine has

been chosen. The chapter reports the evaluation of the performance conducted by the time stepping FEA. The chapter reports the experimental results that were conducted on a prototype. A description of the control infrastructure is reported.

In **Chapter 4**, a simple modulation strategy that allows to reduce the DC-link stress for a triple-3-phase drive is presented. The analysis of the benefits introduced by the PWM phase shifting are evaluated by steady state simulations ,using the software Pspice, in all the possible operating conditions. A worst case approach has been chosen in order to find the best angle of shifting between carriers to reduce the DC-link rms current in multi-3-phase drives. The results of the experimental validation are reported. The same analysis has been extended to sectored multiphase.

In **Chapter 5**, a mathematical model is proposed in order to evaluate the torque and the torque ripple in fractional slot tooth-coil wound (TCW) Synchronous Reluctance (SyR) machines. Considering a generic harmonic field and an ideal SyR rotor, the rotor magnetic potential is modelled and the torque equations are calculated starting from the Lorenz Force Law. Time stepping FEA results are reported in order to verify the formulations.

Appendix A reports the mathematical demonstration that defines the rotor reaction for an ideal SyR rotor together with the methodologies used to design the SyR constant permeance rotor.

Appendix B reports the manufacturing process of the machine.

Appendix C reports the COOL-TIE concept: a cooling devices for the electrical machine compatible with the power electronic integration.

Contents

List of Figures

List of Tables

Chapter 1

Multiphase motor drives

Part of the work described in this chapter has been previously published in [1]

1.1 Introduction

Multi-phase machines are the subject of considerable interest in different fields of application. The main characteristics of multi-phase machines have been well addressed in the last decades [2–4].

Real machines and converters adopting a wide number of phases can be more easily found in the large power applications, in the MegaWatt ranges, especially in the direct-drive solutions for naval traction [5–7], for power generation [8] or for wind turbines [9, 10]. In such applications, the converter redundancy, or the simple subdivision of the machines in sectors supplied by different converters, can be considered a mandatory condition due to the technological limitations.

Traditionally used to reduce the stator phase current in large power applications, multi-phase machines are now gaining a prestigious place also in the field of traction applications for their reliability, fault tolerant capability, weight and volume reduction, together with high efficiency [11–13]. In terms of reliability, multi-phase electric drive represents a very important field of investigation [2]. The chance to have the drive still working with one or more converter legs not working properly [14] is the main advantage in many large power traction applications.

Multi-phase drives, in the field of automotive application, are particularly interesting for Flywheel Alternator Starter (FAS) due to the high number of poles this application typically requires [15, 16].

On the other hand the increased degree of freedom in the control has been investigated especially for the five and seven-phases motors. Even if these machines need peculiar converters, they open the way to a wide variety of modulation strategies mainly devoted to the PWM losses reduction, still maintaining a sinusoidal control.

Another advantage of multi-phase machines with sinusoidal winding distribution is that they present an airgap field distribution with lower space-harmonic content [2]. The Magneto Motive Force (MMF) harmonic content reduction for a 5-phase Permanent Magnet (PM) coil wound machine is addressed in [4].
This compensation of the harmonic components on the MMF has a direct impact on the torque performances. In fact, by increasing the number of phases over three, it is possible to increase the torque density and to reduce the torque ripple amplitude [3, 17–20]. Many works for multi-phase motors had as subject the study of the slot-pole-phase combinations with attention to the windings factor, rotor losses, radial forces [21] and low torque ripple solutions [19, 18, 22]. In [23] an analytical and experimental evaluation of the torque harmonics components for multi-phase induction machines is proposed. The paper shows that the pulsating torque decreases in magnitude and increases in frequency as the number of phases is increased. A general expression for the harmonic field and torque ripple have been proposed too for multi-phase induction machines, two layer windings, excited by non sinusoidal current [24].
The torque's performances peculiarity for the multiphase machines will be analysed in this thesis for a very simple stator structure that could meet the manufacture needs in the automotive world. Especially in the automotive field the low production cost is one of the key point together with high performance. The actual research focus, in fact, is at those solutions that allow a simple construction, reduction in weight and dimensions, without sacrifices in terms of performance. Among all the possible solutions, we will focus on multi-n-phase drive solutions. A generalized algorithm for the definition of a tooth-coil multi-n-phase machine is presented. The algorithm allows to identify the particular subset of multi-n-phase solution that are the focus of the thesis.

1.2 Multi n phase solution

A particular subset of multi-phase drives is the multi-n-phase solution in which the phases are grouped in separated stars of n-phases. Immediate advantages in the use of multi-star motors have been well evidenced in the past [2, 25, 26]. The possible single star fault is supported in these machines with a reduced performance of the drive and, typically, the phase per unit current ripple is reduced. This, again, is a usual solution in large converter current (kAmps) applications. If the n-phase stars are supplied separately, a fault tolerant drive can be easily achieved because each star can work separately, considering a fault both in the converter or in the stator.

A second advantage is in the converter design because this solution allows for an easier integration of power converters and motors active parts from the cooling point of view. A subdivision of the current into different converter structures allows for a larger space for power losses in the converter structure leading to numbers in W/m^2 capability similar to the typical one of the electric machines. In fact, the amount of losses in converter and motor are similar in any well designed drive. Having the actual converter to realize the needed three-phase structure a much smaller cooling surface compared to the motor one, the possibility to integrate, in similar cooling system, the motor and the converter appears complex. If the converter can be structurally split, even if adopting the same amount of silicon, the cooling capability can be increased.

Another advantage in the realization of multi-n-phases machine is the chance to have different voltage levels on each n-phase system. This solution is surely interesting and it has been widely considered if proper windings and phase shift between the various n-phase system is chosen [7]. Beside these, other advantages are possible on the converter side as the reduction of DC-link stress. For multi-n-phase drives in fact it is possible to add an additional degree of freedom, the phase shifting between carriers in order to reduce the DC-link stress [27]. Chapter 4 is dedicated to the investigation of this particular aspect.

The main drawback of this multi-phase drives lay in the increased converter complexity and motor connections. Such a drawback can be reverted into an advantage considering the gained reliability and fault tolerant system. The converters for such machine need to be surely controlled with synchronous PWMs and current sampling leading to a more complex control, possibly needing FPGA modulators.

For the same reasons a larger number of measurements needs to be introduced and conditioned.

1.3 A generalized algorithm for multi-n-phase motor

The aim of this section is to define a general algorithm for the multi-n-phase machine so to have a guideline for the design of this type of machines.
The analysis is focused on an simple tooth-coil wound structure (TCW) and a general algorithm to identify the right stator-rotor coupling is obtained, following a specific rule for multi-n-phase drive.
Fractional-slot non overlapped tooth-coil windings are commonly used in Permanent Magnet (PM) machines, because of the well known advantages, due to the shorter end connections, better fill-in factor and easier and cheaper manufacturing. This algorithm was presented by the author et all in [1]. This algorithm and the definition of the parameters is the starting point for the modelling of this categories of multi-phase machines. Following the proposed rules is possible to obtain a machine with a very low torque ripple contribution. The motor structures analysed in the thesis are mainly the Permanent Magnet (PM) solutions, but the algorithm can be similarly adopted for different synchronous rotor type.

The model parameters are:

N_C: Number of Coils that constitute a star system (having always only one coil per phase)

N_S: Number of Star systems

N_P: Number of Poles (i.e. permanent magnets)

These numbers identify the *base machine*, and

N_M: Number of times the *base machine* is repeated

In the following the relationship between N_P and the total number of phases (1.1) is imposed in order to obtain a high windings factor [28].

$$N_P = N_C \cdot N_S \pm 1 \tag{1.1}$$

The need to have a total even number of poles ($N_P \cdot N_M$) in a rotating machine imposes a minimal choice for the N_M parameter.
Following the rule in (1.1), N_C coils will constitute one star, considering that the electric angle covered by the stator tooth pitch is given by (1.2).

$$\theta_C = \frac{N_P \cdot \pi}{N_C \cdot N_S} \tag{1.2}$$

Two coils of the same star are far N_S coils from each other. In fact, they are separated by an electric angle θ_{ph} multiple of $\frac{\pi}{N_C}$ as shown in (1.3).

$$\theta_{ph} = N_S \cdot \theta_C = \frac{N_P \cdot \pi}{N_C} = N_S \cdot \pi \pm \frac{\pi}{N_C} \tag{1.3}$$

If the rule (1.1) is chosen, the electric angle between two adjacent stars is θ_S as defined in (1.4).

$$\theta_S = \frac{N_P \cdot \pi}{N_C \cdot N_S} = \pi \pm \frac{\pi}{N_C \cdot N_S} \tag{1.4}$$

A star vector approach to the coil distribution would lead to similar conclusions.

The stars can be supplied in different way and different rules in the relation can be chosen, but the proposed rules allow to obtain a better winding factor. The winding factor can be calculated as the product of the pitch factor and the distribution factor. For the machine characterized by one coil per phase, the distribution factor is equal to 1 while the pitch factor for the generic harmonic h is (1.5)

$$k_p = sin\left(\frac{h\pi}{Q}\right) \tag{1.5}$$

In (1.5) Q is the number of slot/coil. The equation 1.5 results in (1.6) for the synchronous harmonic $h = p$ in the solution proposed ($p = N_P N_P/2$

$$k_p = sin\left(\frac{p\pi}{N_C N_S}\right) \tag{1.6}$$

In order to maximize the pitch factor the ratio in (1.6) must to be close to $\pi/2$. The solution $\pi/2$ is not feasible since will lead to pulsating and not rotating magnetic field. The solution $N_P = N_C \cdot N_S \pm 1$ allows to maximize the pitch factor. Examples of the applicable numbers and the resulting machines are reported in the following sections.

1.3.1 Multi 3 phase

The multi-n-phase machine as a combination of 3-phase stars, may be more attractive in an industrial environment due to the wide availability of 3-phase inverter solutions both in the power and in the control area. In fact for multiphase structures, it is possible to realize converters as a combination of different three phase converters with an equal subdivision of the currents. Within the possible structure in the multi-3-phase world, the six-phase one is the most common one and it has been applied to many different motors like induction [29, 30] or permanent magnet motors [31].

The application of the proposed algorithm for a double-3-phase machine results in a machine with parameters $N_C = 3$, $N_S = 2$, $NP = 5$ or $NP = 7$. The need to have a total even number of poles $(N_P \cdot N_M)$ in a rotating machine imposes a minimal choice for the $N_M = 2$. For the six-phase machine that follows the proposed model is possible to realize a stator structure with 12 slots and a coupled rotor with 5 or 7 polepairs. Instead, for a triple-3-phase machine $(N_C = 3, N_S = 3)$ it is possible to realize a stator structure with 9 slots and a coupled rotor with 4 or 5 polepairs $(N_M = 1)$. Another possible solution is 18 slots $(N_M = 2)$ stator structure with 8 or 10 rotor polepairs. For a quadruple-3-phase machine $(N_C = 3, N_S = 4)$ the minimum number of slots is 24 $(N_M = 2)$, in fact, this stator structure can be coupled with 11 or 13 polepairs.

Considering a triple-3-phase machine, that is the main object of the thesis interest the mentioned angles in (1.2), (1.3) and (1.4) became (1.7).

$$\begin{aligned} \theta_C &= \tfrac{10 \cdot \pi}{9} \\ \theta_{ph} &= 3\pi + \tfrac{\pi}{3} = \pi + \tfrac{\pi}{3} \\ \theta_S &= \pi + \tfrac{\pi}{9} \end{aligned} \tag{1.7}$$

Some example of the Poles-to-Coil combinations for multi-3-phase motors are summarized in Table 1.1. The table collects the value of total number of teeth (coil) N_{T_C} and N_{T_P} the total number of poles and the equivalent number q (number of slot per pole per phase) for the 3-phase counterpart.

Table 1.1 *Poles-to-Coil combinations for multi-3-phase motors according with the proposed algorithm*

Machine Description	N_{T_C}	N_{T_P}	q
$3-2-5-2$	12	10	2/5
$3-2-7-2$	12	14	2/7
$3-3-8-1$	9	8	3/8
$3-3-10-1$	9	10	3/10
$3-3-8-2$	18	16	3/8
$3-3-10-2$	18	20	3/10
$3-4-11-2$	24	22	4/11
$3-4-13-2$	24	26	4/13

Being N_{T_C} and N_{T_P} the total number of teeth and magnets, it appears immediately evident that the machines this way realized have large poles number even for the simpler structures.

The main advantage for the proposed structures is surely the easiness in the winding realization. It will be shown in the Chapter 2 that the MMF harmonic content in the $N_C - N_S$ phase star is limited and the global torque is really smooth [32, 33]. All of this is obtained still maintaining a concentrated winding stator in what is typically called a double layer type. The winding factor of the multi-3-phase solutions, designed and supplied according with the proposed rules, are generally greater than the equivalents three phase counterparts characterized by a q. From the slot winding layout in the electrical space, the windings factor for each phase has to be calculated as the ratio between the resulting electromotive force and the number of windings contribution for each phase [21, 34, 26].
For example, for the $3-3-10-1$ solution (or equivalent the $3-3-10-2$) the winding factor calculated on the synchronous harmonic is equal to 0.985 [35], [36], while for the $q_{3/10}$ solution the calculation of the winding factor for the 3-phase solutions leads to the well known result of 0.945 [37].
In this case for example the ratio between the winding factor is equal to 0.96, which can be seen as an increase in the torque density of the triple-3-phase solution by 4%, or like an 8% reduction in the copper losses at the same delivered torque.

In the Chapter 2 the characteristics of multi-n-phase machines designed with the rules proposed in the algorithm (1.1) will be analysed and their low torque ripple capabilities will be analytically proven.

1.4 Conclusions

The reasons to search for multi-phase structures are various. The main reason is the reliability and the fault-tolerant capability that can be obtained with these motors and converters. Additional degree of freedom in the control can be used to improved the performances of the drive, and the increment in the number of phase allows to obtain advantages in terms of torque ripple reduction. About all the possible solutions a particular subset of machines, the multi-n-phase, has been chosen. A generalized algorithm to identify the right stator-rotor coupling in order to obtain a tooth-coil wound machine with a very low torque ripple contribution is presented and some example of the proposed algorithm are reported. The definition of this algorithm is the starting point for the modelling of the particular categories of multiphase machines investigated in this thesis.

Chapter 2

Torque ripple modelling in multiphase SMPM motors

Part of the work described in this chapter has been previously published in [38]

2.1 Introduction

The aim of this Chapter is to offer a methodology to calculate the torque components for SMPM machines tooth-coil wound. The choices tooth-coil wound causes a lot of harmonics contribution in the harmonic content of Magneto Motive Force (MMF). For these, typically fractional slot concentrate windings are chosen. In this Chapter an analytical calculation of the MMF and its harmonic compensation in multi-n-phase solution is reported. The analysis done allows to understand and quantify the harmonic compensation in the MMF in tooth-coil multiphase machines. A formulation of the torque ripple is then proposed. The model is general and allows to understand and justify the very low torque ripple results of Finite Element Analysis (FEA) and allows to compare directly multiphase machines.

2.2 Multi Phase machine rotating magnetic fields

The calculation of the torque component starts from the calculation of the stator MMF. A generalized approach is here reported for the multi-n-phase machines that follow some specific rules proposed in Capter 1. The approach can be generalized to other machines.

In tooth-coil wound machines each coil has a rich harmonic spectrum, however, the combination of the coils harmonic contributions in a multi-n-phase structure can compensate for most of them.
It is possible to demonstrate this compensation considering the effect of each coil to the rotating magnetic field. This means to consider the magnetic field produced by all coils, distributed in the space and supplied by a proper sinusoidal current sequence.
In order to analitically solve the magnetic field distribution in the airgap, the effects of magnetic saturation is neglected and the distribution of the flux density is considered to be constant along the axial lenght. As a consequence the magnetic vector potential can be considered axially oriented and manipulated like a scalar [39]. Slot permeance variations are neglected. The origin of statoric coordinate α is set at the center of the phase 1. Like suggested in [40] phase 1, that is the origin for the mechanical and electrical references systems (α), will contribute at the firs harmonics of MMF with the component (2.1).

$$f_1^s * cos(\alpha) \tag{2.1}$$

where f_1^s is the amplitude of the MMF at the time t and α is the stator reference frame (Fig. 2.1).

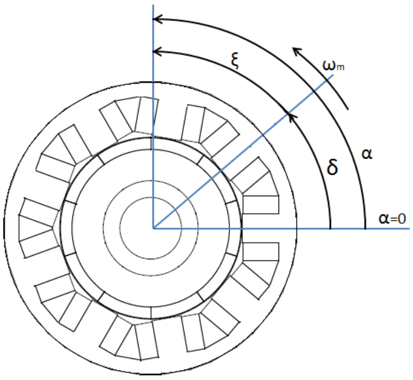

Fig. 2.1 Definition of the reference frame for the generic $N_C N_S N_P N_M$ machine: δ is the rotor position that moves at mechanical speed ω_m, α is the stator reference frame and ξ is the rotor reference coordinate.

In (2.2), (2.1) is generalized for the phase n

$$f_n^s * cos(\alpha - \alpha_n) \tag{2.2}$$

where α_n is the angular position of the axis belonging to the generic coil n. The amplitude of the MMF changes with the time according with the current variation in the coil. Then for the generic coil (2.3) results:

$$f_n^s = f_{n_{peak}}^s * cos(\omega t + \gamma - \theta_e) \tag{2.3}$$

where ω and γ are respectively the pulsation and the electric angle of the supply current, leading with respect to the $t = 0$ position, θ_e is the electric angle of the generic coil n.

Considering r, the generic harmonic order of the winding distribution, the MMF contribution of the generic coil n supplied by a sinusoidal current is expressed in (2.4)

$$\sum_{r=1}^{\infty} f_{n,r}^s cos(\omega t + \gamma - \theta_e) * cos(r(\alpha - \alpha_n)) \tag{2.4}$$

where $f_{n,r}^s$ is the amplitude of the r^{th} harmonic of the MMF produced by the generic coil n. The amplitude $f_{n,r}^s$ is given by (2.5) where $a_{n,r}^s$ is the Fourier series amplitude of the generic harmonic r of the windings distribution, N_n is the number of turn per coil and i_n is the amplitude of the current supply of the generic coil n.

$$f_{n,r}^s = a_{n,r}^s N_n i_n \tag{2.5}$$

In a symmetrical and balanced current system, the coefficients $f_{n,r}^s = f_r^s$ are equal for each coil.

To calculate the stator MMF the contribution of all N coils must be considered. The stator MMF is expressed as in (2.6).

$$f^s = \sum_{n=1}^{N} \sum_{r=1}^{\infty} f_r^s cos(\omega t + \gamma - \theta_e) * cos(r(\alpha - \alpha_n)) \tag{2.6}$$

For a multi-n-phase machine that follows the rules proposed in Chapter 1, it is possible to calculate (2.6) by substituting (2.7). The resulting stator MMF expression

(2.8) is given.

$$\begin{aligned} &N = N_C \cdot N_S \cdot N_M \\ &\theta_e = (n-1)\cdot\theta_S \\ &\alpha_n = \tfrac{(n-1)2\pi}{N} \end{aligned} \tag{2.7}$$

$$\begin{aligned} f^s = \sum_{n=1}^{N}\sum_{r=1}^{\infty} f_r^s \cos(\omega t + \gamma - (n-1)\theta_S) * \\ \cos r(\alpha - \frac{(n-1)2\pi}{N}) \end{aligned} \tag{2.8}$$

The stator MMF in (2.8) can be now decomposed in two rotating fields, direct (2.9) and reverse (2.10), provided that conditions (2.13) ,(2.14) are verified.

$$\begin{aligned} f^{s_d} = \sum_{n=1}^{N_C N_S N_M}\sum_{r=1}^{\infty} \frac{1}{2} f_r^s \cos((\omega t + \gamma - r\alpha) - \\ (n-1)(\pi \pm \frac{\pi}{N_C N_S}) + r\frac{2\pi(n-1)}{N_C N_S N_M}) \end{aligned} \tag{2.9}$$

$$\begin{aligned} f^{s_r} = \sum_{n=1}^{N_C N_S N_M}\sum_{r=1}^{\infty} \frac{1}{2} f_r^s \cos((\omega t + \gamma + r\alpha) - \\ (n-1)(\pi \pm \frac{\pi}{N_C N_S}) - r\frac{2\pi(n-1)}{N_C N_S N_M}) \end{aligned} \tag{2.10}$$

The amplitudes of these rotating fields are equal to $N_C N_S N_M/2$ times the MMF amplitude of the r harmonic belonging to the single phase (f_r^s).

To show this, equations (2.9), (2.10) can be written like in (2.11) and (2.12) to highlight the arguments of the two sinusoidal functions.

$$\begin{aligned} f^{s_d} = \sum_{n=1}^{N_C N_S N_M}\sum_{r=1}^{\infty} \frac{1}{2} f_r^s \cos((\omega t + \gamma - r\alpha) - \\ 2\pi(n-1)(\frac{N_M(N_C N_S \pm 1) - 2r}{2N_C N_S N_M})) \end{aligned} \tag{2.11}$$

$$f^{s_r} = \sum_{n=1}^{N_C N_S N_M} \sum_{r=1}^{\infty} \frac{1}{2} f_r^s \cos((\omega t + \gamma + r\alpha) - 2\pi(n-1)(\frac{N_M(N_C N_S \pm 1) + 2r}{2 N_C N_S N_M})) \tag{2.12}$$

In order to have a generic rotating field of order r, the relationship (2.13), for the direct sequence, or (2.14), for the reverse one, must be verified.

$$\frac{N_M(N_C N_S \pm 1) - 2r}{2 N_C N_S N_M} = integer \tag{2.13}$$

$$\frac{N_M(N_C N_S \pm 1) + 2r}{2 N_C N_S N_M} = integer \tag{2.14}$$

In this case, the contributions to stator MMF of each phase have the same angular displacement and are additive. Equation (2.13) and (2.14) are verified for the orders r for which the contributions to the stator MMF of the single phase have same angular displacement and are additive. It is worth noticing that the r harmonics that contribute to non-zero harmonic fields are slot harmonics. Once known the parametric model, it is possible to forecast the harmonic spectrum of the rotating fields in any multi-n-phase machine.

A graphical explanation of the formula is given in Fig. 2.2 for a machine $3-3-10-1$. The generic harmonic of the pulsating field of the single phase is decomposed in its direct component (green arrow) and in its reverse component (purple arrow). Summing the contribution for each coil some of that results in a zero sum, other sum each other in order to generate a rotating magnetic field.

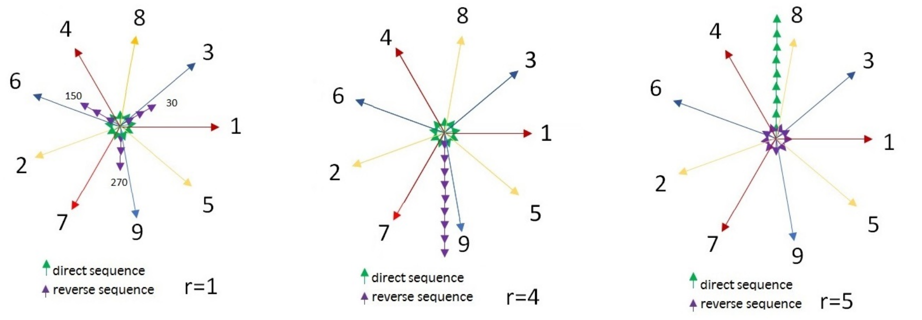

Fig. 2.2 Direct (green) and reverse (purple) f^s component for the harmonic order $r = 1, 4, 5$ in $3-3-10-1$ machine

2.3 Torque ripple modelling

In the previous section the harmonic distribution of the stator MMF has been presented for a multi-n-phase coil wound motor. In this section the methodology that leads to the evaluation of the torque ripple harmonic contributions is reported for a generic N_C, N_S, N_P, N_M Surface Mounted Permanent Magnet (SMPM) multi-n-phase motor.

Considering an isotropic machine, as the SMPM is, the reluctance torque component is negligible. Cogging torque is not considered.
The instantaneous torque can be calculated by considering the Lorentz force law [41] as in (2.15).

$$T_e = r_g l \int_{2\pi} B_g \mathrm{d}f_s = r_g l \int_0^{2\pi} B_m \frac{\mathrm{d}f_s}{\mathrm{d}\xi}\mathrm{d}\xi \tag{2.15}$$

where r_g is the radius at the air gap, l is the stack length, f^s is the stator MMF and B_g is the flux density at the air gap. It can be substituted by the flux density due to the magnet B_m since, for a SMPM machine, the armature reaction field do not contributes to the torque. ξ is the rotor reference coordinate.

The harmonic distribution of the stator MMF (2.8) can be expressed like in (2.16) as a series of non-zero harmonic fields at the air gap,

$$f^s = \sum_{k=0}^{\infty} f^s_{rd_k} cos(\omega t + \gamma - r_{d_k}\alpha) + f^s_{rr_k} cos(\omega t + \gamma + r_{r_k}\alpha) \tag{2.16}$$

where $f^s_{rd_k}$ and $f^s_{rr_k}$ are the amplitudes of the non-zero harmonic fields at the air gap (equal to $\frac{N_C N_S N_M}{2} f^s_r$) and r_{d_k} and r_{r_k} are, respectively, the non-zero direct and reverse corresponding harmonic orders for which (2.13) and (2.14) are verified.
The expressions of r_{d_k} and r_{r_k} are reported in (2.17) and (2.18).

$$r_{d_k} = k(N_s N_C N_M) + \frac{N_M(N_C N_S \pm 1))}{2} \quad k = 0,1,2,3... \tag{2.17}$$

$$r_{r_k} = k(N_S N_C N_M) - \frac{N_M(N_C N_s \pm 1))}{2} \quad k = 0,1,2,3... \tag{2.18}$$

Considering the reference frame in Fig. 2.1, with a rotor that moves in synchronous operation with the first direct stator harmonic, (2.16) can be written in the rotor reference frame as in (2.19) if the rotor is aligned to $\alpha = 0$ axis at $t = 0$. The derivative expression of (2.19) is reported in (2.20). The parameter $p = N_P/2$ is the polepairs.

$$\begin{aligned}
f^s = &\sum_{k=0}^{\infty} f^s_{rd_k} cos(\omega t + \gamma - r_{d_k}(\xi + \frac{\omega t}{p}))+ \\
&f^s_{rr_k} cos(\omega t + \gamma + r_{r_k}(\xi + \frac{\omega t}{p})) \\
= &\sum_{k=0}^{\infty} f^s_{rd_k} cos((1 - \frac{r_{d_k}}{p})\omega t - r_{d_k}\xi + \gamma)+ \\
&f^s_{rr_k} cos((1 + \frac{r_{r_k}}{p})\omega t + r_{r_k}\xi + \gamma)
\end{aligned} \tag{2.19}$$

$$\begin{aligned}
\frac{\mathrm{d}f_s}{\mathrm{d}\xi} = &\sum_{k=0}^{\infty} f^s_{rd_k} r_{d_k}\, sin((1 - \frac{r_{d_k}}{p})\omega t - r_{d_k}\xi + \gamma)- \\
&f^s_{rr_k} r_{r_k} sin((1 + \frac{r_{r_k}}{p})\omega t + r_{r_k}\xi + \gamma)
\end{aligned} \tag{2.20}$$

For a given SMPM machine, it is assumed the magnets flux density to be a square wave. Its Fourier series is given in (2.21).

$$B_m(\xi) = \sum_{h \neq 2,4,6...}^{\infty} b_h \cos(hp\xi) \tag{2.21}$$

Substituting in (2.15) equations (2.20) and (2.21) it is possible to recognize the effect of the interaction of B_m with the direct and reverse components of f^s. Considering the Werner's formula, the instantaneous torque is given by (2.22).

$$\begin{aligned}
Te = &\sum_k \sum_h \frac{1}{2} r_g l * \\
&(\int_{-\pi}^{\pi} f^s_{rd_k} r_{d_k} b_h \sin\left[(1 - \frac{r_{d_k}}{p})\omega t - (r_{d_k} \pm ph)\xi + \gamma\right] \mathrm{d}\xi \\
&- \int_{-\pi}^{\pi} f^s_{rr_k} r_{r_k} b_h \sin\left[((1 + \frac{r_{r_k}}{p})\omega t + (r_{r_k} \mp ph)\xi + \gamma)\right] \mathrm{d}\xi)
\end{aligned} \tag{2.22}$$

Only the stator and rotor harmonics that have the same orders interact to give a torque component. The ones producing a torque component are the h, r_k values for which (2.23) is valid.

$$
\begin{aligned}
& r_{d_k} \mp ph = 0; \\
& r_{r_k} \pm ph = 0;;
\end{aligned}
\tag{2.23}
$$

Among these, the h, r_k for which continuous torque occurs, are the ones that follow (2.24) or (2.25).

$$
\begin{cases}
r_{d_k} \mp ph = 0; \\
(1 - \frac{r_{d_k}}{p}) = 0
\end{cases}
\tag{2.24}
$$

$$
\begin{cases}
r_{r_k} \pm ph = 0; \\
(1 + \frac{r_{r_k}}{p}) = 0;
\end{cases}
\tag{2.25}
$$

As a consequence, considering a machine with $N_P = N_C N_S + 1$, the continuous torque occurs for $r_{d_k} = ph$ with $h = 1$ (or $r_{r_k} = ph$ and $h = 1$ if $N_P = N_C N_S - 1$). The torque, then, follows equation (2.26).

$$
\begin{aligned}
Te = \frac{1}{2} r_g l \int_{-\pi}^{\pi} f^s_{rd_0} r_{d_0} b_1 \sin\gamma \ \mathrm{d}\xi \\
= \pi r_g l f^s_{rd_0} r_{d_0} b_1 \sin\gamma
\end{aligned}
\tag{2.26}
$$

The torque ripple, instead, occurs when (2.27) or (2.28) are valid and $h \neq 1$.

$$
r_{d_k} = ph \rightarrow h = \frac{r_{d_k}}{p} \tag{2.27}
$$

$$
r_{r_k} = ph \rightarrow h = \frac{r_{r_k}}{p} \tag{2.28}
$$

It follows that, considerings (2.17) and (2.18), the order h for which torque ripple occurs can be calculated as (2.29) and, considering the rules in (2.30) and (2.31), it is possible to obtain the closed expression (2.32).

$$
h = \frac{k(2N_M N_S N_C) \pm N_M (N_C N_S \pm 1)}{2p} \tag{2.29}
$$

$$
(N_C N_S \pm 1) = N_P \tag{2.30}
$$

$$
N_P N_M = 2p \tag{2.31}
$$

$$
h = \frac{k(N_M N_S N_C)}{p} \pm 1 \tag{2.32}
$$

Considering $N_M = 1$ and $N_M = 2$, in order h to be an integer (2.33) must be verified. Then the rotor harmonic h for which torque ripple occurs can be calculated as in (2.34). If $N_M = 1$ in order h to be an odd number m must assume only even value.

$$k = mp \qquad m = 1, 2, 3.. \tag{2.33}$$

$$h = m(N_M N_S N_C) \pm 1 \tag{2.34}$$

For the generic $N_C N_S N_P N_M$ motor, only the rotor harmonic h matching (2.32) produces torque ripple pulsating at the harmonic i (2.35) on the mechanical period where ± is a function of the interaction with the direct or reverse sequence.

$$i = p(h \pm 1) \tag{2.35}$$

In the analysed stator MMF harmonic distribution, for the same (k, m) combination, if the harmonics h ($h \neq 1$) meets an r_{d_k} the following one ($h + 2$) meets an r_{r_k} and vice-versa.
For each $m > 0$ there are 2 contribution to torque whose pulsation and phase are a function of r and γ. Following these rules the first harmonic that gives a torque ripple can occur at very high frequency.

2.4 Application of the model

This section is focused on the application of the proposed model to two specific multi-n-phase machines:

- $3-3-10-1$ machine characterize by $N_C = 3$, $N_S = 3$, $N_P = 10$,$N_M = 1$
- $3-4-13-2$ machine characterized by $N_C = 3$, $N_S = 4$, $N_P = 13$, $N_M = 2$

The machine, defined as 3-3-10-1, is depicted in Fig. 2.3a. The machine phasor diagram is shows in Fig. 2.3b. The winding distribution of a generic coil for the $3-3-10-1$ machine is depicted in Fig. 2.4. Its harmonic spectrum is very rich and is reported in Fig. 2.5. Most of the harmonic present in the spectrum compensate each other. For example for the harmonic order $r = 1$ direct and inverse sequences have both a null resultant. For $r = 4$ the contributions to the direct sequence is null and only the reverse sequence remains. The opposite happens for $r = 5$. When all

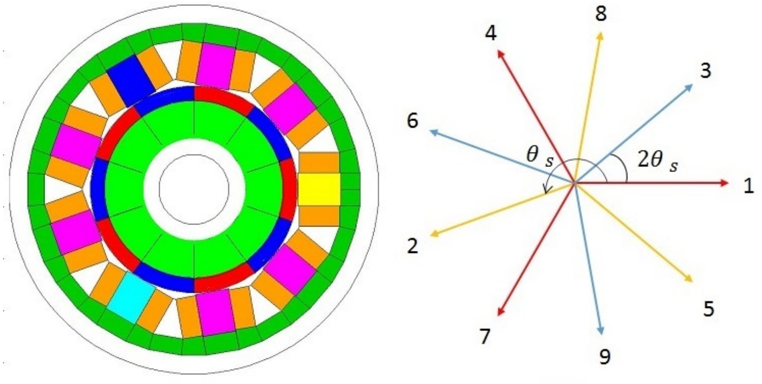

(a) (b)

Fig. 2.3 3-3-10-1 machine: a) motor structure, yellow, blue and cyan teeth identify the first 3-phase contribution b) Phasor diagram 3-3-10-1 motor structure in which the number at the end of the phasors represents the sequential numbering of the coils starting from the yellow one.

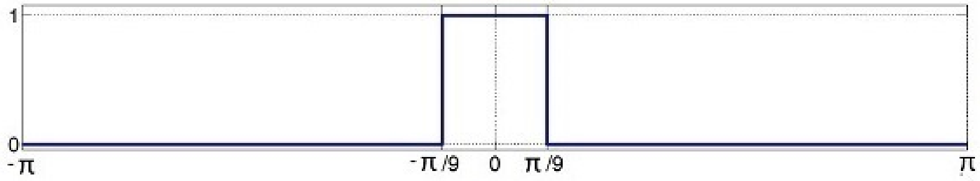

Fig. 2.4 a) 3-3-10-1 machine: winding distribution to the generic coil normalized for the number of turns per coil

harmonics orders are considered the stator MMF spectral distribution is calculated resulting like in Fig. 2.6. The same result should be obtained with (2.17), and (2.18) applied to the 3-3-10-1 machine considering only the positives results, that is (2.36) that are slot harmonics [4].

$$\begin{cases} r_{d_k} = 9k+5 \\ r_{r_k} = 9k-5 \end{cases} \tag{2.36}$$

The amplitude of each r_k is proportional to the amplitude of the corresponding Fourier series coefficient for the single coil ($a^s_{n,r}$) as in (2.37) for the 3-3-10-1 machine.

$$\begin{aligned} f^s r_{d_k} &= \tfrac{9}{2} N_n i_n a^s_{n,r_{d_k}} = \tfrac{9}{2} N_n i_n \tfrac{2}{r_{d_k}\pi} sin(r_{d_k}\tfrac{\pi}{9}) \\ f^s r_{r_k} &= \tfrac{9}{2} N_n i_n a^s_{n,r_{r_k}} = \tfrac{9}{2} N_n i_n \tfrac{2}{r_{r_k}\pi} sin(r_{r_k}\tfrac{\pi}{9}) \end{aligned} \tag{2.37}$$

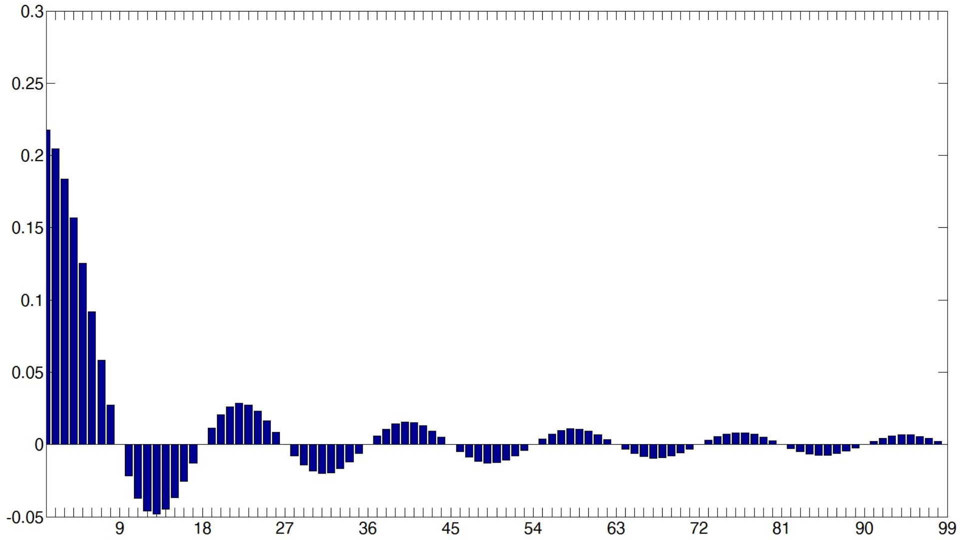

Fig. 2.5 3-3-10-1 machine: MMF harmonic component of the 3-3-10-1 machine with $N_n = 1$ and $i_n = 1$. .

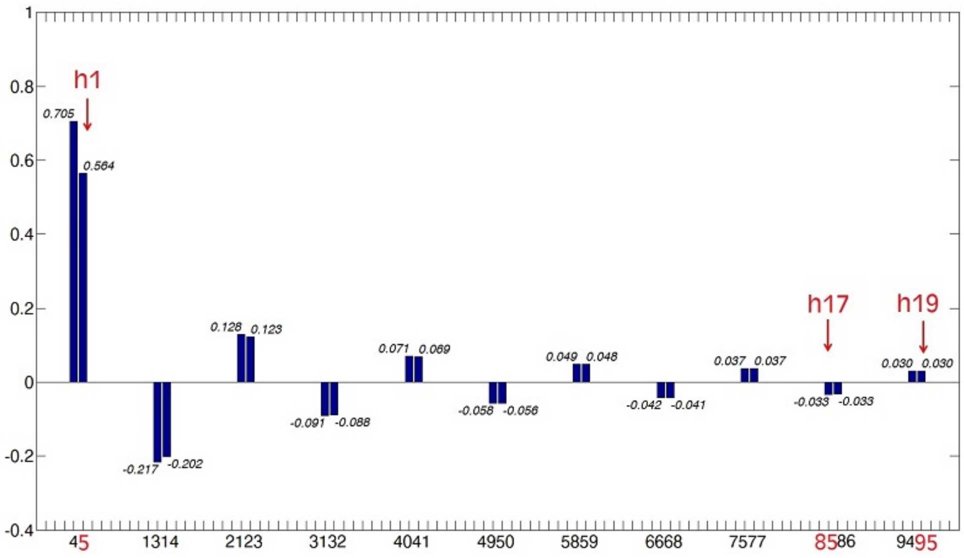

Fig. 2.6 3-3-10-1 machine: MMF harmonic component of the 3-3-10-1 machine with $N_n = 1$ and $i_n = 1$. In red the orders that contribute to continuous and ripple torque.

For the 3-3-10-1 machine, (2.21) became (2.38).

$$B_m(\xi) = \sum_{h \neq 2,4,6\ldots}^{n} b_h \cos(5h\xi) \tag{2.38}$$

Being a SMPM machine the coefficient b_h can be expressed as in (2.39) where B is the square wave amplitude of the flux density due to the magnets.

$$b_h = (-1)^{\frac{h-1}{2}} \frac{4}{h\pi} B \tag{2.39}$$

The interaction between the 5^{th} direct stator harmonic and the 1^{st} rotor harmonic order provides continuous torque. Considering (2.40) the mean torque is (2.41).

$$\begin{cases} r_{d_k} = ph \rightarrow h = 1 \\ r_{d_k} = p = 5 \end{cases} \tag{2.40}$$

$$Te = \pi r_g l f^s_{rd_0} 5 b_1 \sin\gamma \tag{2.41}$$

The harmonic orders h, r for which torque ripple occurs are summarized in (2.42). Under the hypothesis that h should be only an odd numbers the m must assume only even number.

$$\begin{cases} h = 9m \pm 1 \\ r_k = ph = 5(9m \pm 1) \end{cases} \tag{2.42}$$

The resulting torque ripple orders of the mechanical revolution are defined in (2.43).

$$i = 5(h \pm 1) \tag{2.43}$$

In Tab. 2.1 the orders h, k, r, the stator MMF and flux density harmonics components (normalized to those that provide continuous torque), and the corresponding torque contributions are reported. From Tab. 2.1 the torque ripple dependence on the current argument gamma is evidenced. For $\gamma = 90°$ the two contributions to the same ripple order (e.g. 18^{th}) are out of phase and this reduces the ripple content. Of course, this is no more true if some flux weakening is driven. In Fig. 2.6 the (r, h) couples that contribute to the torque (continuous and ripple) are highlighted in red.

Same considerations are valid for any multi-n-phase machine defined following the rule in (1.1). As an example, for the 3-4-13-2 machine the harmonic spectrum of the stator MMF is characterized by positive results in (2.44) and is reported in Fig.2.7

$$\begin{cases} r_{d_k} = 24k + 13 \\ r_{r_k} = 24k - 13 \end{cases} \tag{2.44}$$

Table 2.1 *Torque harmonic pulsation for the* $3-3-10-1$ *machine*

m	h	k	r	$\frac{f^s_{rd,i_k}}{f^s_{r_{d_0}}}$	$\frac{b_h}{b_1}$	Torque pulsation
0	1	0	5	+1	+1	$sin\gamma$
2	17	10	85	-0.056	+0.059	$-sin(18\omega t+\gamma)$
2	19	10	95	+0.051	-0.053	$-sin(18\omega t-\gamma)$
4	35	20	175	-0.027	-0.028	$-sin(36\omega t+\gamma)$
4	37	20	185	+0.026	+0.027	$-sin(36\omega t-\gamma)$
6	53	30	265	-0.011	+0.024	$-sin(54\omega t+\gamma)$
6	55	30	275	+0.010	-0.023	$-sin(54\omega t-\gamma)$

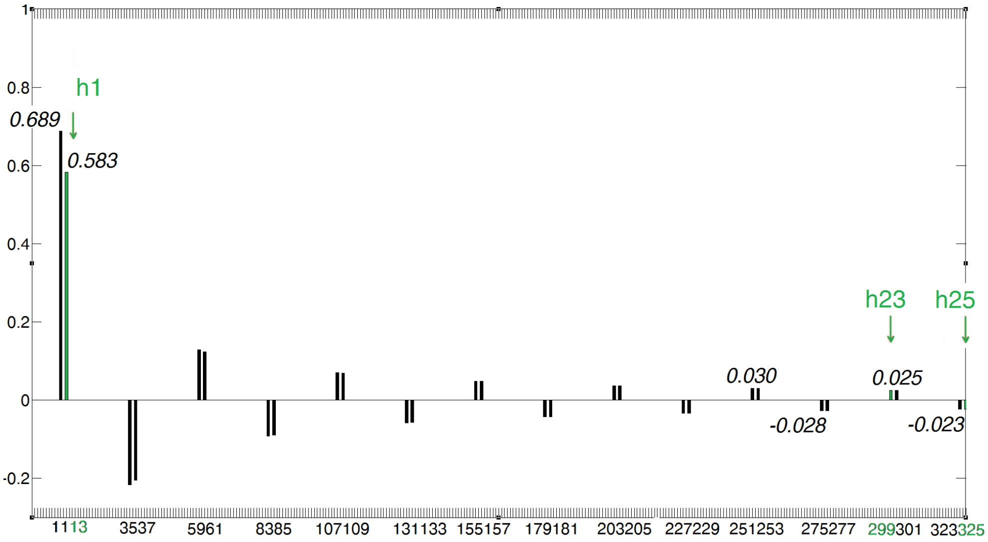

Fig. 2.7 3-3-10-1 machine: MMF harmonic component of the 3-4-13-2 machine with $N_n = 1$ and $i_n = 1$. In green are evidenced the orders that contribute to torque components.

The amplitude of the harmonics r can be evaluated like in 2.45

$$\begin{aligned} f^s r_{d_k} &= \tfrac{24}{2} N_n i_n a^s_{n,r_{d_k}} = \tfrac{24}{2} N_n i_n \tfrac{2}{r_{d_k}\pi} sin(r_{d_k} \tfrac{\pi}{24}) \\ f^s r_{r_k} &= \tfrac{24}{2} N_n i_n a^s_{n,r_{r_k}} = \tfrac{24}{2} N_n i_n \tfrac{2}{r_{r_k}\pi} sin(r_{r_k} \tfrac{\pi}{24}) \end{aligned} \tag{2.45}$$

The amplitude of the rotor harmonics h can be evaluated like in 2.39. Among all the harmonics the couples h, r that interact for the ripple generation are defined in (2.46). The harmonic order of the torque ripple occurs at the frequency (2.47). For

$m = 0$, ($h = 1$, $r = 13$) the mean torque results.

$$\begin{cases} h = 24m \pm 1 \\ r = ph = 13(24m \pm 1); \end{cases} \tag{2.46}$$

$$i = 13(h \pm 1); \tag{2.47}$$

2.5 Validation

In the previous section two examples of the application of the model have been presented, focusing on the stator MMF and torque harmonic order components. This section is dedicated to the verification of the torque model by FEA.

2.5.1 3-3-10-1 SMPM

The 3-3-10-1 machine under test is shown in Fig. 2.3a and the motor dimension are collected in Tab.2.2. The rotor interpolar width has been minimized in order to obtain a squared rotor flux density distribution. The machines are supplied according to Chapter 1. The torque evaluation is achieved by processing the results of a 2D-FEMM simulation along a complete electric turn and a torque angle of 90 electrical degree. In Fig. 2.8 the flux density map is reported in one of the calculated points. Simulation and model results are reported in Fig. 2.9 and in Tab. 2.3. In Tab. 2.3 only the torque harmonic components taken into account by the model are reported. Otherwise, all the other harmonics that occur from the FEA have a value lower than 0.1% of the continuous torque. The second line of Tab. 2.3 reports the value

Table 2.2 *Motors Dimensions*

Machine	3-3-10-1	3-4-13-2
External diameter	140mm	219mm
Internal diameter	77,8mm	158mm
Airgap	0,5mm	0,5mm
Active length	100 mm	100mm
$N_n * i_n$	1054 A	471 A

achieved by the model. It is worth noticing that the value of flux density B used in the calculation of (2.39) plays a key role in the correct evaluation of the torque and has been identified by FEA.

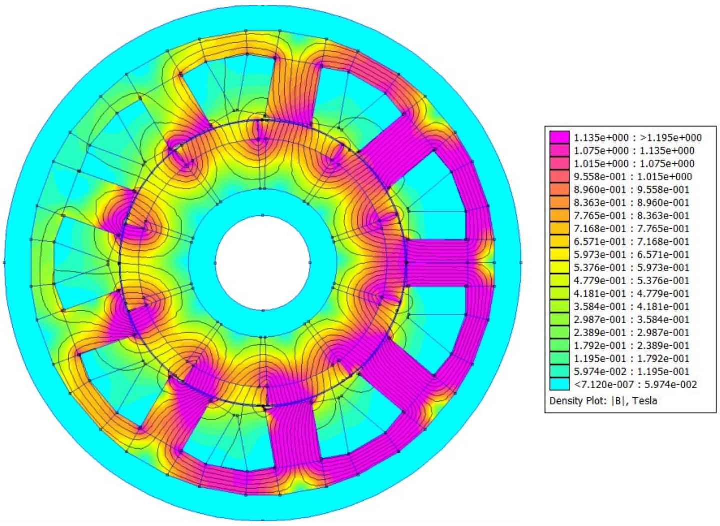

Fig. 2.8 Simulation results: 3-3-10-1 motor cross section flux density distribution at full load FEMM 2D solution.

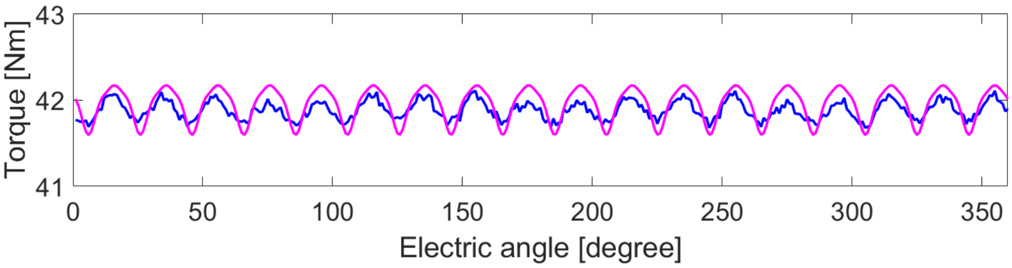

Fig. 2.9 Instantaneous torque expressed in Nm on the electric period: 3-3-10-1 motor simulation results (blue line) and model results (pink line).

2.5.2 3-4-13-2 SMPM

The simulation has been repeated for the 3-4-13-2 machine in Fig. 2.11 with dimensions collected in Tab.2.2. The torque behaviour along one electrical degree is reported in Table 2.4 collects the torque informations for the simulation and the modelling.

Table 2.3 *Mean torque and the rms torque ripple harmonic expressed in Nm for the* 3-3-10-1 *motor*

Harmonic order	0	18	36	54
9-Phase Simulation	41.8781	0.1360	0.064	0.0082
9-Phase Model	41.9508	0.2583	0.06381	0.0282

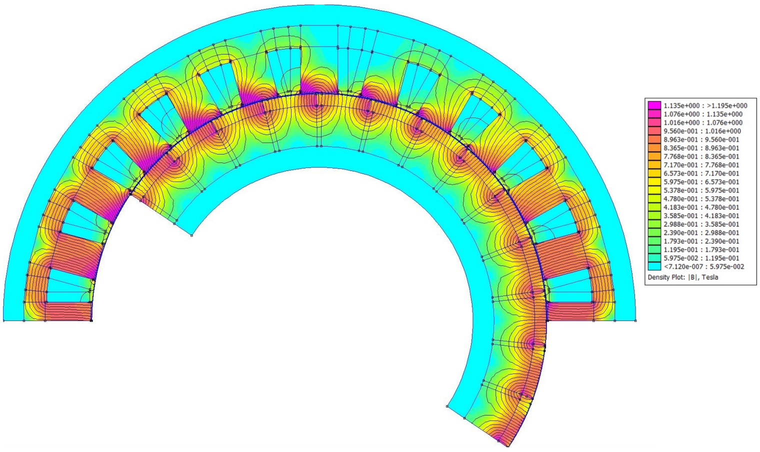

Fig. 2.10 Simulation results: 3-4-13-2 motor cross section flux density distribution at full load FEMM 2D solution.

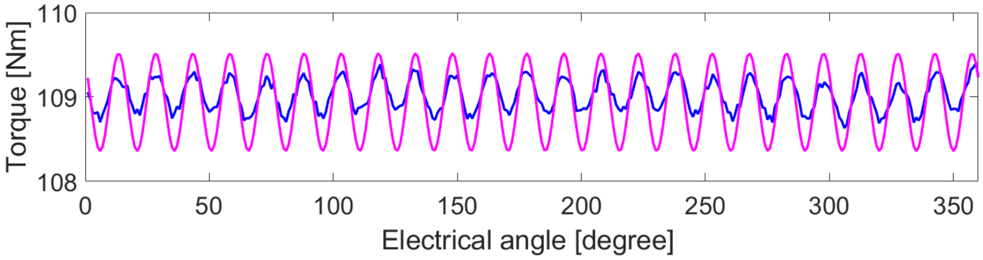

Fig. 2.11 Instantaneous torque expressed in Nm on the electric period: 3-4-13-2 motor simulation results (blue line) and model result (pink line).

Table 2.4 *Torque harmonic components expressed in Nm for the* 3-4-13-2 *motor*

Harmonic order	0	24
12-Phase Simulation	109.026	0.2408
12-Phase Model	108.9398	0.5740

2.6 Conclusions

In this chapter a torque modelling for multi-n-phase machine that follows the rules proposed in the previous chapter has been presented. In this chapter has been demonstrate how, following the proposed rules, it is possible to built a very simple structure machine with a cleaner stator MMF spectrum with advantages in terms of magnetic circuit load capability. The cleaner stator MMF spectrum has a direct impact on the torque ripple. A torque ripple harmonic formulation make available a simple predicting formula, allowing to instantly compare multi-n-phase machines. The proposed model has been validated by simulation results for two multiphase machine. The torque rms ripple value for 3-3-10-1 machine and 3-4-13-2 machine simulated is less than 0.33% of the mean torque if the electric angle is chosen equal to 90 degree. The approach used in the torque calculation allows to understand the mechanism of torque ripple production and how it depends on the electric angle of the supply current. The very low value of the torque ripple found in the reported simulations can be only partially explained by the model that overestimate the torque ripple. Moreover an additive effect is found in the rectified tooth shaping chosen. This argument will be analysed more in detail in the next chapter.

Chapter 3

Design of a 9 phase machine with a very simple structure

3.1 Introduction

The aim of the research was to investigate the advantages introduced by Multiphase synchronous machines with a simple structure, mainly focusing on the advantages in terms of torque performances. The stator structure chosen was the tooth-coil wound because of its realization and maintenance. In this chapter, the design of the machine is reported.

The context is the one of the automotive application. Multiphase machines are welcome in high pole-pairs structures such as the direct drive solutions for flywheel starter alternator or in high frequency traction machines.
The chapter presents the design of a 20kW, 8000rpm motor for traction application based on concentrated windings stator structures.
Tooth-coil windings are appreciated for their easy realization and maintenance prospective. The choices tooth-coil wound causes a lot of harmonics contribution in the harmonic content of Magneto Motive Force (MMF) but thanks to the combination multiphase-machine/ tooth-coil-wound it is possible to obtain a simple structure machine with a limited harmonic spectrum in the MMF.

The machine design was validated by Finite Element Analysis (FEA). The design started from the stator analyses. The torque performances were evaluated by FEA considering a classical Surface Mounted Permanent Magnet (SMPM) rotor. Then a

PM-inset rotor was analysed and the performances are reported. The machine 9-slot 9-coil inset 10 pole rotor was realized and then tested in order to validate the results. More details about the manufacturing process are reported in the Affendix B.

3.2 Stator Design and preliminary studies

The concentrated winding stator introduces performance benefit, like simple construction, reduction of frontal connections and the related Joule losses reduction, and the constant power speed range can be properly increased thanks to the high MMF harmonic contribution that affects the stator inductance. [42].

The machine design constraints are given by the allowable volume. A ring shape is chosen whose dimensions are shown in Table 3.1

Table 3.1 *Motor data for the design*

External Diameter	142	mm
Internal Diameter	79.66	mm
Airgap	0.5	mm
Active lenght	101	mm
PM remanence 20°	1.2	T
Current density	13	A/mm^2
Total number of Teeth	9	–
Total Number of PM	$8-10$	–

Among the multi-n-phase solutions, the multi-3-phase is one of the most interesting because of the availability of 3-phase commercial inverters.

Regarding all the possible solutions, the design focuses on the solution that allows to obtain the lowest number of slots. A triple-3-phase machine ($N_C = 3, N_S = 3$) has then been selected. Both solutions $N_P = 10$ or $N_P = 8$ can be chosen. Being N_P an even number the minimum number of base machines is $N_M = 1$. In order to better clarify the concept, lets calculate the numbers of slot for a double-3-phase machine ($N_C = 3, N_S = 2$) designed according to the rules proposed in Chapter 2. In this case, being N_P an odd number, the minimum number of base machines is $N_M = 2$. Then the double-3-phase solution lead to a machine design with a greater number of slots compared to the triple-3-phase machine solution. The proposed triple-3-phase structure in the 3-phase version, can be seen as an extension of the

$q = 3/10$ (or $q = 3/8$) fractional slot two layer windings motor that is known to be a low torque ripple solution.
The stator structure proposed is the coil wound one as depicted in Fig.3.1.

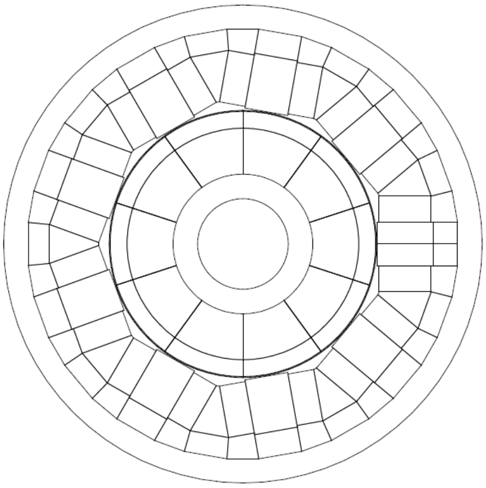

Fig. 3.1 Stator structure proposed.

As previous mentioned, thanks to the combination multiphase-machine/tooth-coil-wound it is possible to obtain a limited harmonic spectrum in the MMF. In the Subsection 3.2.1 the analysis of the MMF for the stator proposed is reported.

3.2.1 MMF

In the Chapter 2, the parametric model to define the machine has been presented together with the mathematical rules to recognize the torque ripple orders for an SMPM machine. In this section the model is applied to the specific triple-3-phase solution characterized by $N_C = 3, N_S = 3$.

Considering this triple-3-phase machine the quantities defined in (1.2), (1.3), (1.4) result in (3.1)

$$\begin{gathered} \theta_C = \tfrac{10\cdot\pi}{9} \\ \theta_{ph} = 3\pi + \tfrac{\pi}{3} = \pi + \tfrac{\pi}{3} \\ \theta_S = \pi + \tfrac{\pi}{9} \end{gathered} \tag{3.1}$$

The stator structure presented in Fig.3.1, is supplied by a symmetrical star in which each phase is displaced by the characteristic angles in (3.1). Applying the equation (2.13) and (2.14) the harmonic orders that contribute to the rotating magnetic field are identified in 3.2 and 3.3.

$$r_{d_k} = k(9) + 5 \quad k = 0, 1, 2, 3... \tag{3.2}$$

$$r_{r_k} = k(9) - 5 \quad k = 1, 2, 3, 4... \tag{3.3}$$

The harmonic that results from 3.2 contributes to the direct sequence of the MMF and the harmonic that results from 3.3 contributes to the reverse sequence harmonic. The resulting MMF harmonic spectrum is reported in Fig.3.2. The harmonics that contribute to the rotating field are only slot harmonics. The same stator can be combined with a 4 pole pairs rotor or with the 5 pole pairs rotor. In Fig.3.2 are highlighted the harmonic components of the MMF that can interact with the $4p$ rotor's harmonic (in green) and with the $5p$ rotor's harmonic (in red) in order to produce torque components.

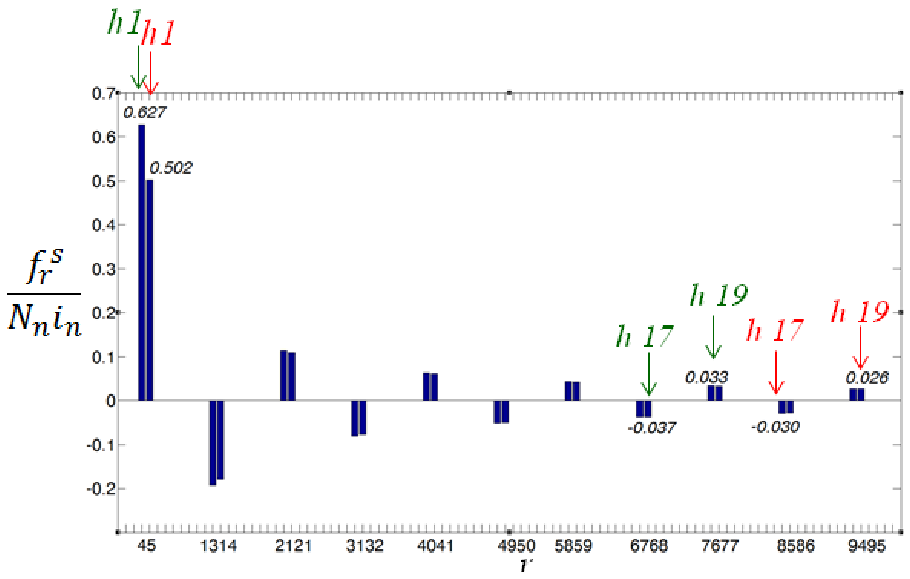

Fig. 3.2 MMF harmonics in the triple-3-phase tooth-coil machine.

According to (2.32) and (2.35) the first harmonic order of the torque ripple is $18th$ on the electric period for the SMPM solution. For the combination stator-rotor solution proposed high frequency torque ripple is expected. In the next subsection, some preliminary torque performances are evaluated by FEA for simplified SMPM rotor in the $4p$ and $5p$ version. In order to understand the potentiality of the structure an IPM version was also considered. In the Section 3.4 the performance analysis is reported for the designed real machine.

3.2.2 Preliminary simulations

Imposing the same stator, it is possible to build different multi-n-phase motors solutions, adopting different rotor types.
In the following section the torque produced by $5p$ pairs and $4p$ motor combinations supplied with the same stars and same current density, are compared. According to the nomenclature introduced in Chapter 2 we talk of $3-3-10-1$ if the $5p$ rotor is considered and $3-3-8-1$ machine if the $4p$ rotor is considered. The analysis is conducted by time stepping FEA 2D simulations on one mechanical revolution and focused on the torque performances. The software used is FEMM 4.2. Due to the asymmetry in the stator, all the machine must be simulated in the 2D plane. With the aim of comparison, for each rotor solution, the same machine structure has been also simulated with the current supply of a 3-phase q=3/10 (or q=3/8) machine.

The simulations were performed for motors with dimensions reported in 3.2. The peak phase's current amplitude was settled to $25A$.

Table 3.2 *Motor Dimensions*

External diameter	140	*mm*
Internal diameter	77,8	*mm*
Airgap	0,5	*mm*
Active length	100	*mm*

SMPM 3-3-10-1 and 3-3-8-1 machines

Time stepping simulations were executed along one mechanical revolution for the $3-3-10-1$ machine and for the $3-3-8-1$. The flux density plots are reported in Fig.3.3 for the $3-3-10-1$ and for the $3-3-8-1$ machine. The torque results in Nm are reported in Fig.3.4. The torque of the triple-3-phase motor is shown by green lines. The torque for the same motor structure wound like a 3-phase $q=3/10$ (or $q=3/8$) machine with the same current densities and torque angles is also reported by blue lines. The torque ripple is very low and spans from 1.64% to 0.69% of the mean torque for the $3-3-10-1$ solution and from 2.45% to 1.38% of the mean torque for $3-3-8-1$ solution, always occurring at a mechanical frequency $18p$ for the triple-3-phase one. A $6p$ harmonic order occurs for the 3-phase solutions. This machine already presents a low torque ripple but its performances can be improved in the multi-n-phase configuration.

In the analyses done it is possible to see typical benefit of multiphase machines. The most significant component of the torque ripple moves at higher frequency and the torque mean value increases due to the greater winding factor [20]. Moreover, the absence of the sixth ripple harmonic will certainly reduce the core loss content.

Mean torque is greater in the triple-3-phases than in their 3-phase counterparts because of the greater windings factor. The torque contributions in more detail are reported in Tab. 3.4 for all simulated machines.

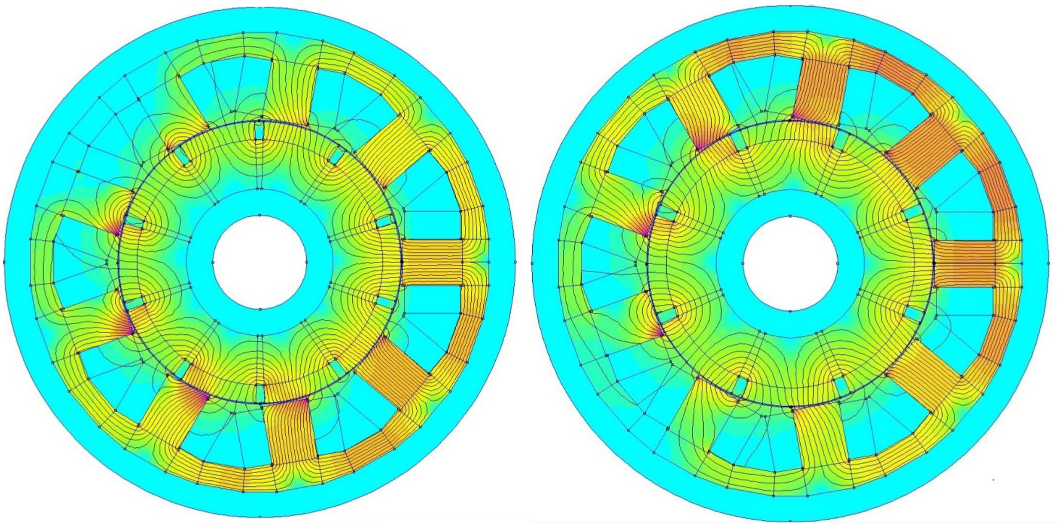

Fig. 3.3 Flux density plot: on the left simulation result for $3-3-10-1$ SMPM, on the right simulation result for $3-3-8-1$ SMPM. Highest mean induction on the teeth $|B| = 1.44T$.

Brush-less PM-inset 3-3-10-1 machine and IPM 3-3-8-1 machine

The low torque ripple benefits from the proposed structure and the possible extension of the model to other rotors design are shown by coupling the chosen stator structure with an Permanent Magnet (PM)-inset and with an Interior Permanent Magnet (IPM) rotor. For small size high speed applications where the PM bandage wants to be

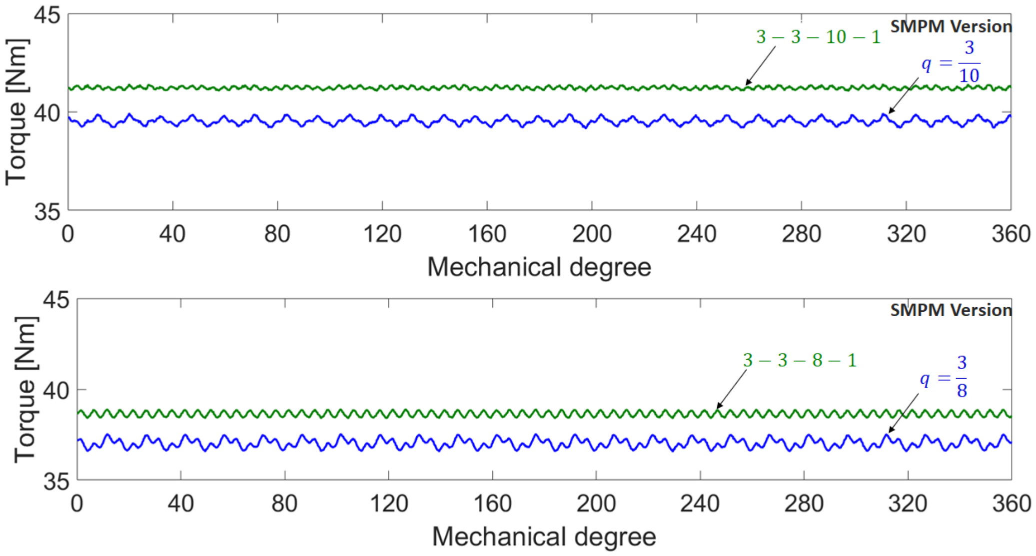

Fig. 3.4 Simulation results (Nm vs mechanical degree on one mechanical turn): torque evolution for SMPM $3-3-10-1$ and $3-3-8-1$ machines (green lines) and their three phase counterpart (blue lines).

avoided, a magnets inset rotor design can be useful. A simplified PM-inset structure is simulated and the flux density plot is reported on the left picture of Fig.3.5. In Fig.3.5 is also reported, on the right, the flux density solution for the $3-3-8-1$ IPM machine. The choice of 8 as the number of poles is done because of the more realistic mechanical design. Considering the machine dimensions in Tab.2.2 the 8 poles solution allows to obtain a feasible flux guide shape. The machines have the same dimensions with respect to the SMPM machines previously simulated and are supplied in the same way. The analysis of the torque ripple is extended considering the equivalent 3-phase counterparts. The results are reportet in Fig.3.6.

Also for PM-Inset solution, the first component of the torque ripple occurs at the $18p$ mechanical harmonic (top picture of Fig.3.6). The ripple is 0.9% of the mean torque but a reduction of the 6.7% on the mean torque occurs.

For the IPM version a significant contribution of $2,67\%$ still occurs at $18p$ harmonic order but also a $9p$ harmonic occurs. Comparing the 3-phase solution with the triple-3-phase one it is possible to outline a reduction of the torque ripple from 8.79% to 2.72% and the increase in the mean torque.

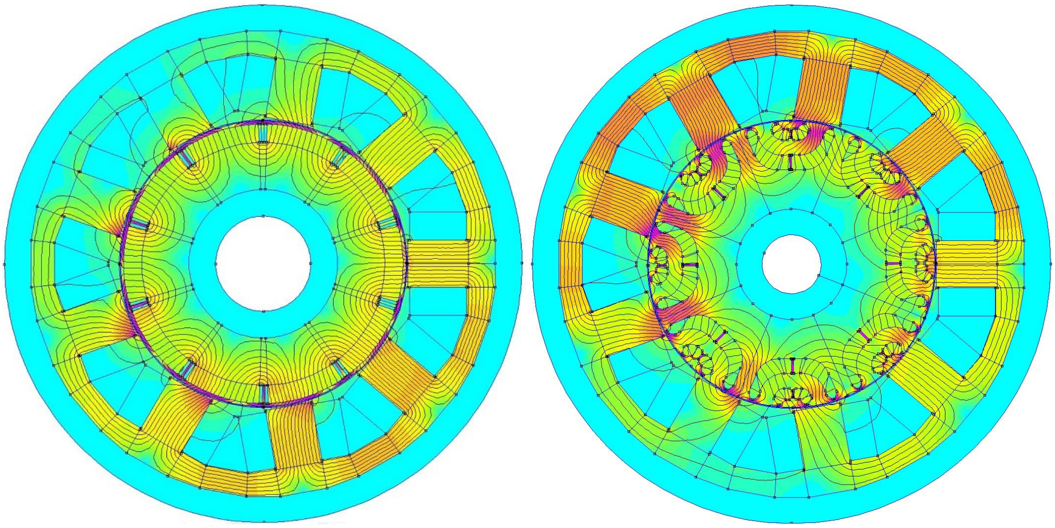

Fig. 3.5 Flux density plot: on the left picture simulation result for $3-3-10-1$ PM-Inset (highest mean induction on the teeth $|B| = 1.39T$), on the right picture simulation result for $3-3-8-1$ IPM version (Highest mean induction on the teeth $|B| = 1.68T$).

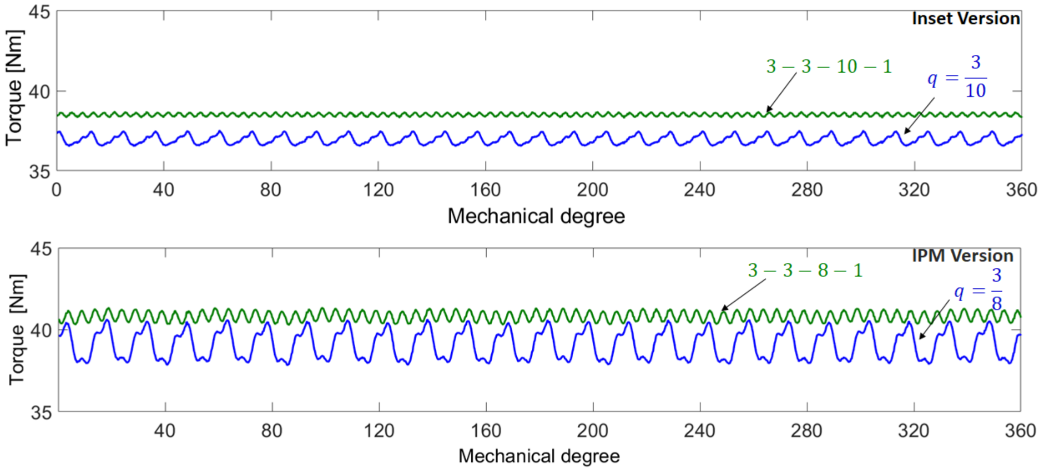

Fig. 3.6 Simulation results (Nm vs mechanical degree one mechanical turn): the green lines represent torque evolution for PM-Inset $3-3-10-1$ (up) and for an IPM $3-3-8-1$ machines (down). Blue lines identifies their three phase counterparts.

Torque evolution under fault conditions

To complete the analysis made in the previous sections some fault conditions have been considered.

The fault conditions analysed are the converters faults. At a single leg fault the disconnection of the related 3-phase converter follows. No changes in the current

TABLE 3.2.b *Simulation results: the table collects the mean torque and the peak-to-peak torque ripple harmonic on the mechanical period expressed in Nm for the 3-3-10-1 and 3-3-8-1 versions in healthy case, under stars faults together with 3-phase counterparts.*

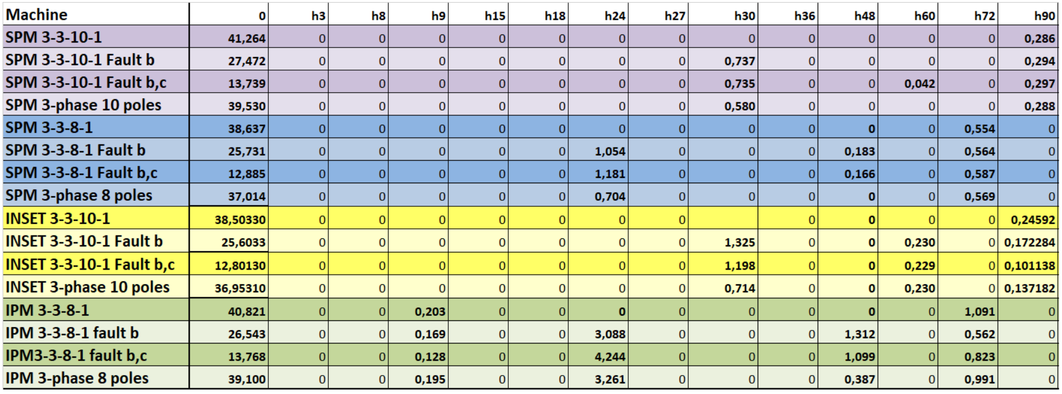

Machine	0	h3	h8	h9	h15	h18	h24	h27	h30	h36	h48	h60	h72	h90
SPM 3-3-10-1	41,264	0	0	0	0	0	0	0	0	0	0	0	0	0,286
SPM 3-3-10-1 Fault b	27,472	0	0	0	0	0	0	0	0,737	0	0	0	0	0,294
SPM 3-3-10-1 Fault b,c	13,739	0	0	0	0	0	0	0	0,735	0	0	0,042	0	0,297
SPM 3-phase 10 poles	39,530	0	0	0	0	0	0	0	0,580	0	0	0	0	0,288
SPM 3-3-8-1	38,637	0	0	0	0	0	0	0	0	0	0	0	0,554	0
SPM 3-3-8-1 Fault b	25,731	0	0	0	0	0	1,054	0	0	0	0,183	0	0,564	0
SPM 3-3-8-1 Fault b,c	12,885	0	0	0	0	0	1,181	0	0	0	0,166	0	0,587	0
SPM 3-phase 8 poles	37,014	0	0	0	0	0	0,704	0	0	0	0	0	0,569	0
INSET 3-3-10-1	38,50330	0	0	0	0	0	0	0		0	0	0	0	0,24592
INSET 3-3-10-1 Fault b	25,6033	0	0	0	0	0	0	0	1,325	0	0	0,230	0	0,172284
INSET 3-3-10-1 Fault b,c	12,80130	0	0	0	0	0	0	0	1,198	0	0	0,229	0	0,101138
INSET 3-phase 10 poles	36,95310	0	0	0	0	0	0	0	0,714	0	0	0,230	0	0,137182
IPM 3-3-8-1	40,821	0	0	0,203	0	0	0	0	0	0	0	0	1,091	0
IPM 3-3-8-1 fault b	26,543	0	0	0,169	0	0	3,088	0	0	0	1,312	0	0,562	0
IPM3-3-8-1 fault b,c	13,768	0	0	0,128	0	0	4,244	0	0	0	1,099	0	0,823	0
IPM 3-phase 8 poles	39,100	0	0	0,195	0	0	3,261	0	0	0	0,387	0	0,991	0

control are provided in the remaining inverters. The three stars are considered independent from each other and with separated center taps. Under the hypothesis that each star is connected to a 3-phase converter the number of admissible star faults is two.

Under fault the stator MMF harmonic compensation is less efficient and the harmonic spectrum is enhanced by other non-zero terms. In Fig.3.7 it is possible to compare the stator MMF harmonic contribution for the triple 3-phase machine for no fault operation (green), single inverter fault operation (yellow) and double inverter fault operation (red). As a result, the harmonic contribution to torque ripple becomes more important for faulted cases. In Fig.3.8 and in Fig.3.9 are reported the torque behaviours for the single inverter fault (yellow line) and double inverter fault (red line) respectively for the SMPM $3-3-10-1$ machine and for the IPM $3-3-8-1$. The detailed harmonic spectra of the torques for all the solutions are reported in Table 3.2.b for all the solutions analysed. The mean torque is reduced near to $2/3$ and $1/3$ of the full torque for single and double inverter fault respectively as expected.

3.2.3 Tooth shaping

The decision to design a stator structure with open slots is in principle related to the manufacturing simplicity. An open slot solution is also desirable in order to reduce the mutual inductance between phases and between stars in the machine.

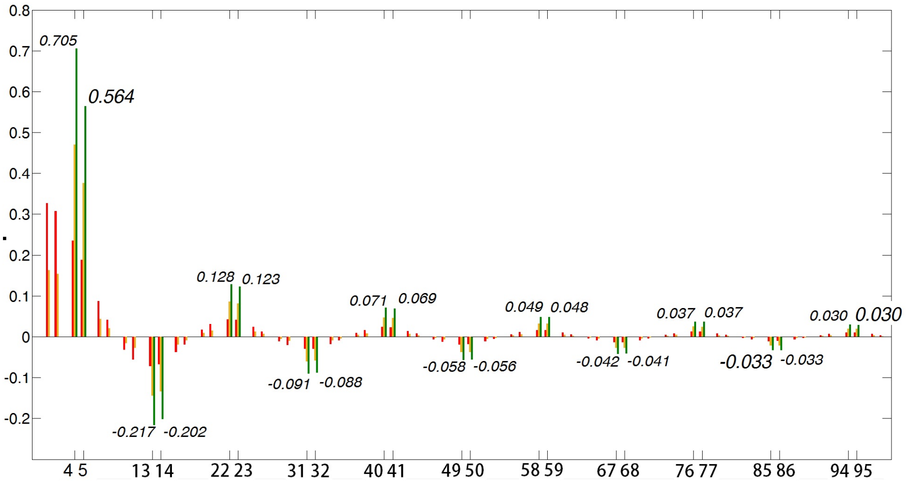

Fig. 3.7 Stator MMF harmonic spectrum for the triple 3-phase machine in normal operation (green), single inverter fault operation (yellow), double inverter fault one (red). The amplitudes are calculated considering a single turn per coil supplied by $1A$ current.

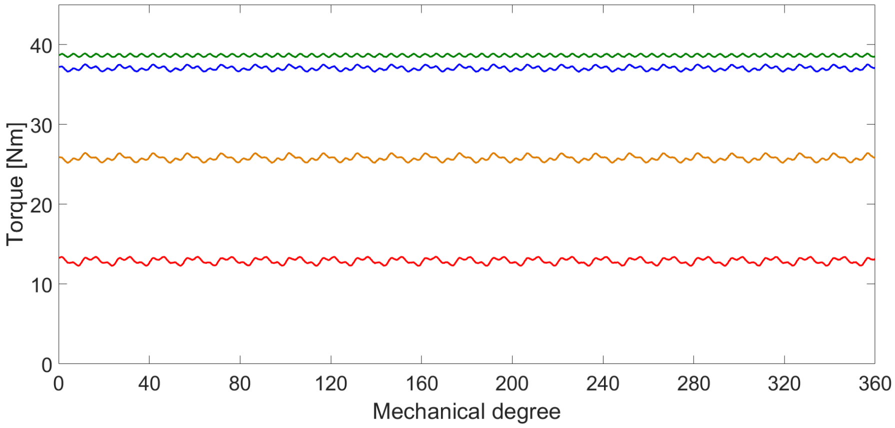

Fig. 3.8 Simulation results (Nm vs mechanical angle): torque evolution for SMPM $3-3-10-1$ machine in normal operation (green), single inverter fault operation (yellow), double inverter fault one (red) and its three phase counterpart (blue).

The very low value of the torque ripple found in the reported simulations can be only partially explained by the amplitudes and signs of the harmonic components of the stator MMF and flux density due to the magnets. The torque coefficients in equation (2.22) are, roughly, inversely proportional to the harmonic order. In fact, being the b_h coefficient and $f^s_{r d_k}$ $f^s_{rr_k}$ in (2.22) both inverse proportional to the harmonic order, a further multiplication by the harmonic order itself comes from (2.15). As a consequence, the two contributions to 18th torque ripple harmonic look still quite large, as $1/17$ and $1/19$ of the mean torque. However, it has be shown in

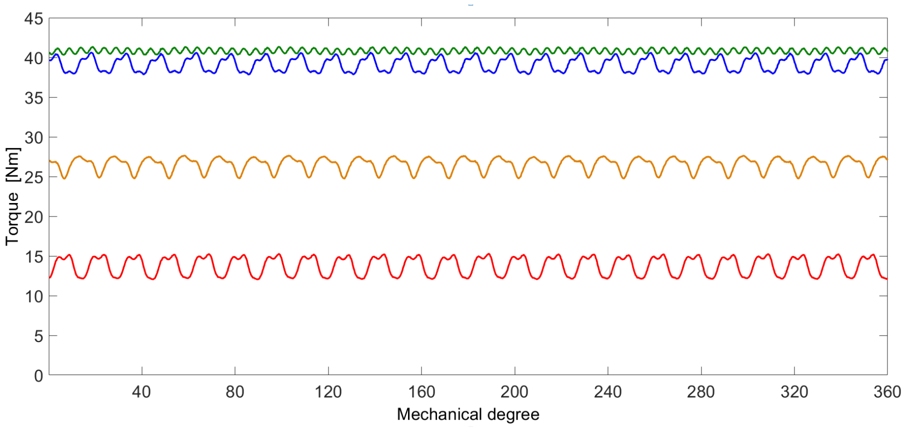

Fig. 3.9 Simulation results (Nm vs mechanical angle): torque evolution for IPM $3-3-8-1$ machine in normal operation (green), single inverter fault operation (yellow), double inverter fault one (red) and its three phase counterpart (blue).

[43] that they are out of phase, at least when a current angle $\gamma = 90$ is applied. As a consequence, the expected peak to peak ripple can be near to 1.2%.

Moreover an additive effect is found in the tooth shoe shaping pointed out in Fig.3.10**a**.

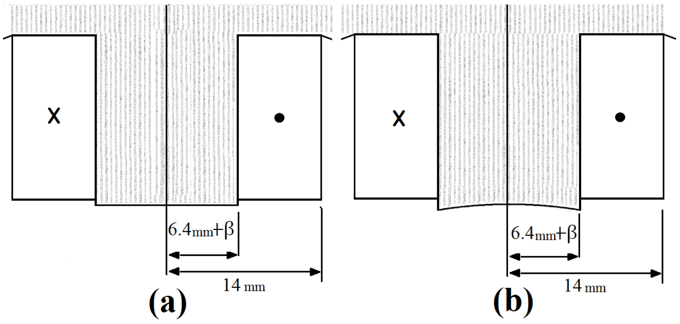

Fig. 3.10 Tooth shoe shaping: (**a**) tooth shoe rectified, (**b**) constant air gap tooth shaping. β is the tooth width variation in mm

To show this, a further simulation has been performed, by considering a different constant air gap tooth shoe as shown in Fig.3.10**b**. As a result, the 18th harmonic peak-to-peak torque ripple is increased from 0.69% (tooth **a**) to 2.31% (tooth **b**). This assesses that the impact of the tooth shaping is relevant in reducing the torque ripple. In addition, the tooth shaping helps in reducing the ripple sensitivity to tooth width, which has a non negligible effect on the torque ripple itself, as it would be expected from the quite high order of the considered MMF harmonics.

Table 3.3 *Torque and peak-to-peak torque ripple for different tooth shoe shaping for 3-3-10-1 solution*

Shaping	β	$Tnom[Nm]$	$Tripple18p[Nm]$	%
a	0	41.3	0.286	0.69
a	+0.4mm	40.8	0.350	0.85
a	−0.4mm	39.6	0.175	0.44
b	0	42.3	0.978	2.31
b	+0.4mm	42.8	1.19	2.80
b	−0.4mm	41.2	0.424	1.03

To show this, reference can be made to Table.3.3 where different tooth widths are reported, for both tooth shapes **a** and **b** in Fig.3.10, together with the related torque values. As it can be seen the peak-to-peak torque ripple varies between 0.44% and 2.80% by varying shoe type and tooth width (considering a 1° variation). Mean torque also varies with tooth width, than a compromised solution has been adopted for the final design.
In the following, main reference will be made to the stator in Fig.3.1 and tooth type **a** in Fig.3.10.

3.2.4 Forces

It is well noticing that the three phase conterparts of the proposed structures is one of the not recommended in terms of radial forces due to the asymmetry in the machine layout [44] and it is characterized by vibration mode 1 [45]. These behaviour has been analyzed by Prof. Zhu et all in [46] for the three phase solution. In this subsection the radial forces are evaluated for the proposed multiphase structure, in order to understand the differences compared to the three phase counterparts. The evaluation of the Unbalanced Magnetic Forces (UMF) by FEM analysis has been conducted for the $3-3-10-1$ machine and for the $3-3-8-1$ machine and or their 3-phase counterparts. The results of the radial forces in their x and y components are reported in Fig.3.11 over 360 electrical degree (the same forces system occurs two times during the mechanical period).

As in the three phase version, the solution $3-3-10-1$ has a smaller contribution of the first radial force harmonic compared to the $3-3-8-1$. As a consequences in the next only the 10 poles solution is analysed.

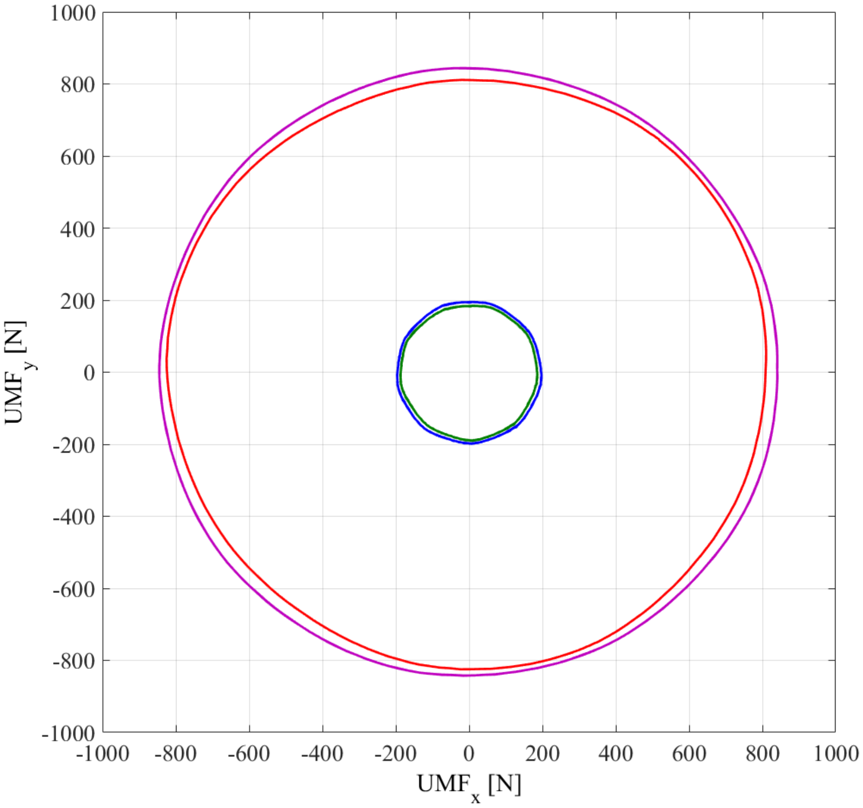

Fig. 3.11 UMF for $q = 3/10$ (green ring) $3-3-10-1$ machine (blue ring) $q = 3/8$ (red ring) and $3-3-8-1$ (purple ring).

3.3 Rotor design

In the preliminary analyses a simplified inset rotor has been considered. In this section a real rotor design is analysed and the results collected. An inner PM-inset rotor with the magnets drowned under the rotor surface is proposed. Preliminary analyses of the load lines for the magnet are reported. The effect of the proposed structure is analysed considering three different permanent magnets configurations. Then mechanical feasibility of the structure is analysed and the results are here reported.

3.3.1 Material properties

The magnet chosen is a NdFeB 38UH magnet. The load lines for the classical SMPM version can be evaluated, under the hypothesis of infinite permeability, by to the definition of the flux density of the magnet like in (3.4).

$$B_m = \frac{H_c lm - N_s i}{\dfrac{Hcl_m}{B_r} - \dfrac{A_m l_g}{A_g \mu_0}} \tag{3.4}$$

In 3.4 H_c is the coercive force l_m is the length of the magnet in the direction of the flux N_s is the number of turn per coil i is the current in the coil B_r is the remanent flux density A_m is the surface of the magnet l_g is the length of the air gap A_g is the air of the air gap and μ_0 is permeability of the material in the vacuum. The parameter for the calculation are reported in the Table 3.4.

The load lines for different value of length of the air gap and for different current value are reported in Fig. 3.12 and Fig. 3.13.

3.3.2 External ring effect

We chosen a PM-Inset solution for the rotor in order to avoid bandaging of the magnets. The solution proposed presents an housing slot for the magnets by means of an external ring on the magnets surface. The cross section of the rotor is reported in Fig. 3.14.

Table 3.4 *Data Table*

H_c	$860-915$	kA/m
B_r	$1.22-1.26$	T
μ_0	$4\pi 10^{-7}$	H/m
l_m	$4*10^{-3}$	m
A_m	$2.4*10^{-3}$	m^2
l_g	$0.5-1.2*10^{-3}$	m
A_g	$(2.4592-2.4812)*10^{-3}$	m^2
N_s	42	-
i	$0-25$	A

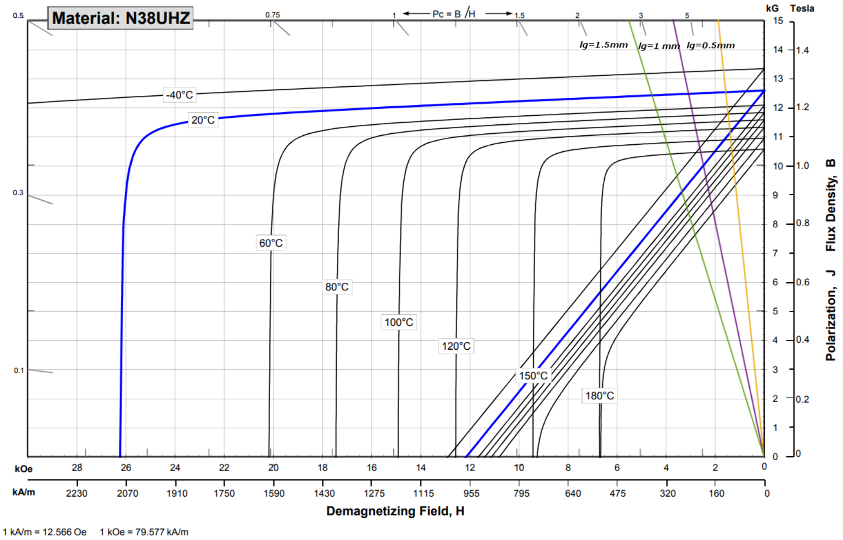

Fig. 3.12 Demagnetization curves for NdFeB 38UH and load line for different values of l_g at $i=0$.

The effect of the external ring was evaluated by FEA, collecting the informations of the flux densities on the rotor surface in the case of rotor surrounded by air and in the case of rotor surrounded by an iron ring. We conducted 2D simulations considering three different magnets design:

- array of magnets: 5 magnet side by side for each pole
- magnets with radial magnetization
- magnets with parallel magnetization

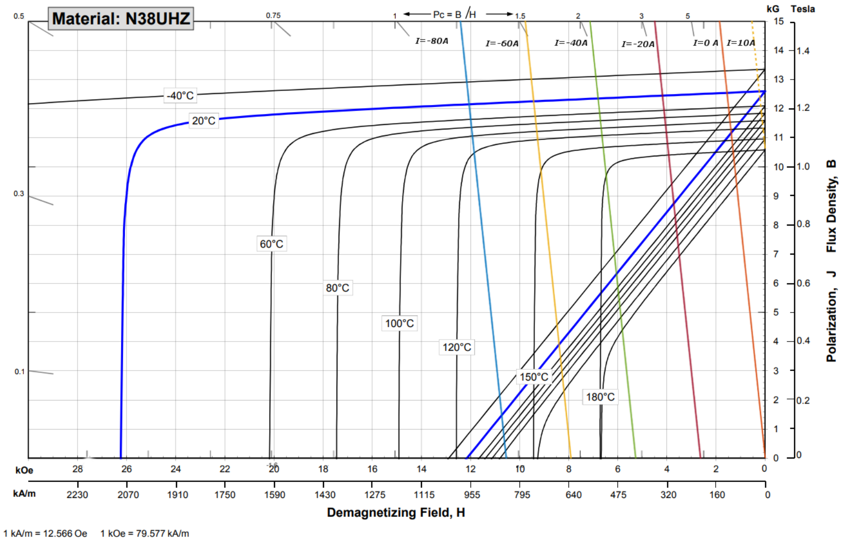

Fig. 3.13 Demagnetization curves for NdFeB 38UH and load line for different values of i.

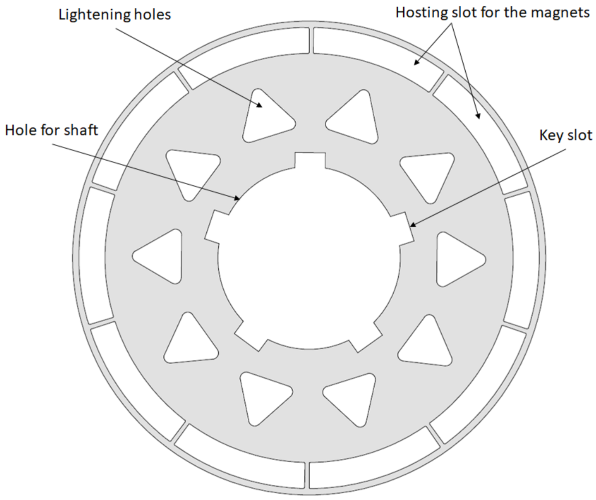

Fig. 3.14 PM-Inset rotor solution.

and the flux density on the rotor surface is collected. The results were also compared with the classical surface mounted permanent magnets rotor. In order to make the results comparable all the rotor had the same external dimensions and the magnets had the same areas.

Array of magnets

The particular rotor design chosen allows to use commercial magnets that don't need further customization. In fact, in each housing slot it is possible to insert a row of magnets side by side like in Fig. 3.15. Here the analysis is reported for a row of five magnets. This row can then be repeated in the axial dimension of the rotor. The rotor was analysed by 2D FEM and the flux density plot is reported in the left picture of Fig. 3.16 for a rotor surrounded by air, and in the right picture of Fig. 3.16 for the rotor surrounded by an iron. The first case means to consider the rotor by itself. In the second case it is possible to understand the rotor behaviour without consider stator anisotropy. It is worth to notice that the magnet were appositely considered inserted in unsymmetrical way in order to emulate some errors that can occurs during assembly. The normal flux density was evaluated on the external ring surface for both the solutions and the results are reported in Fig. 3.17 The same results of Fig. 3.17 are reported with more detail in the left picture of Fig. 3.18 for the rotor surrounded by air and in the right picture of Fig. 3.18 for the rotor surrounded by iron. In Fig. 3.18 the normal flux densities are reported for material M250-35A (blue line) and for M300-35A5 (green line).

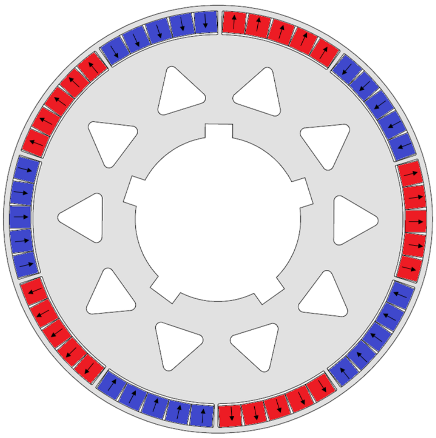

Fig. 3.15 Array of magnets solution: cross section of the inset rotor solution with a row of five magnet for each rotor's housing slot.

Radial magnetization

The external ring effect is here analysed for customized magnet with radial magnetization. We conduct simulations with a single magnet with radial magnetization in

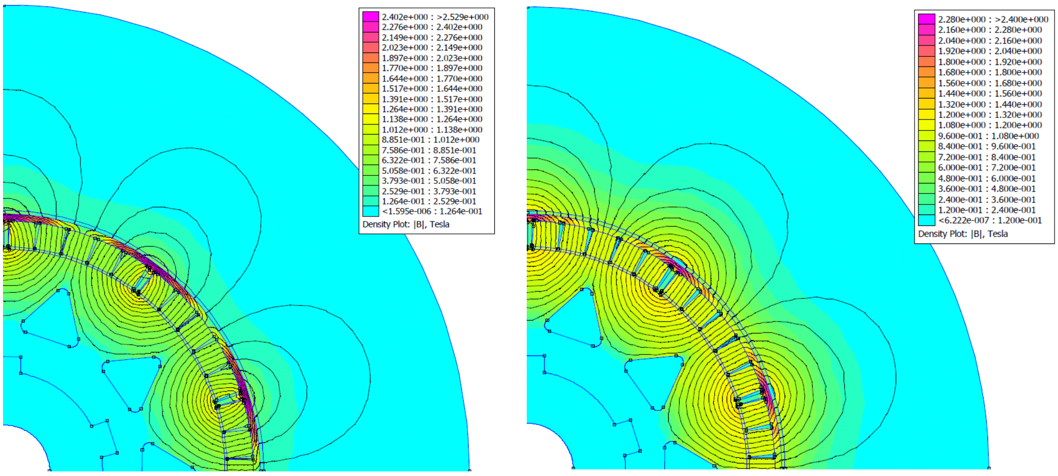

Fig. 3.16 Array of magnets solution: flux density plot for inset rotor with a row of 5 magnets in each rotor's slot. On the left the flux density plot for the rotor surrounded by air, on the right is reported the flux density plot when the rotor is surrounded by iron. Materials are M250-35A (IEC 60404-8-4:1998) for the iron and NdFeB 38UH for the magnets

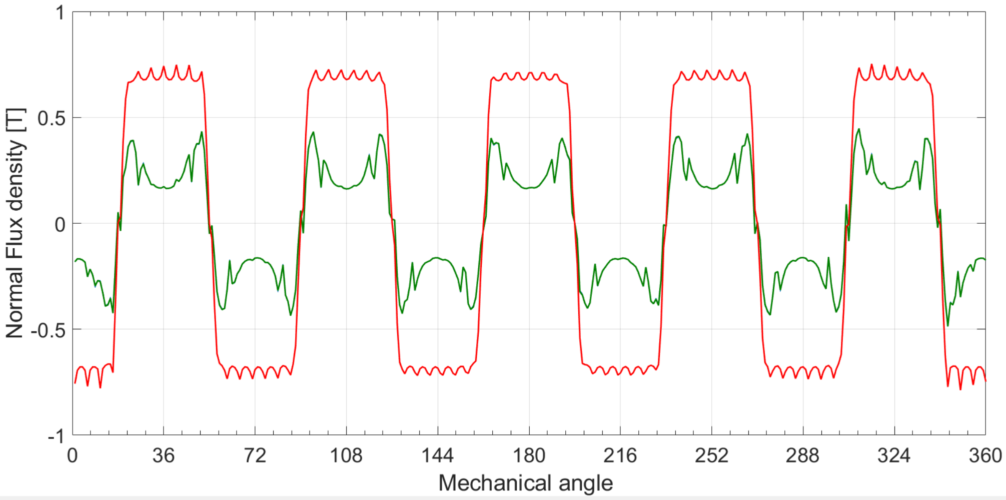

Fig. 3.17 Array of magnets solution: normal flux density on the whole rotor surface. Green line is the normal flux density for the rotor surrounded by air. Red line is the normal flux density for the rotor surrounded by iron.

each housing slot like in Fig. 3.19. The rotor was analysed by 2D FEM and the flux density plot is reported in the left picture of Fig. 3.20 for a rotor surrounded by air, and in the right picture of Fig. 3.20 for the rotor surrounded by an iron. According to the analysis previous reported, the normal flux density was evaluated on the external ring surface for both the solutions and the results are reported in Fig. 3.21. The same results of Fig. 3.21 are reported with more detail in Fig. 3.22 for the rotor surrounded

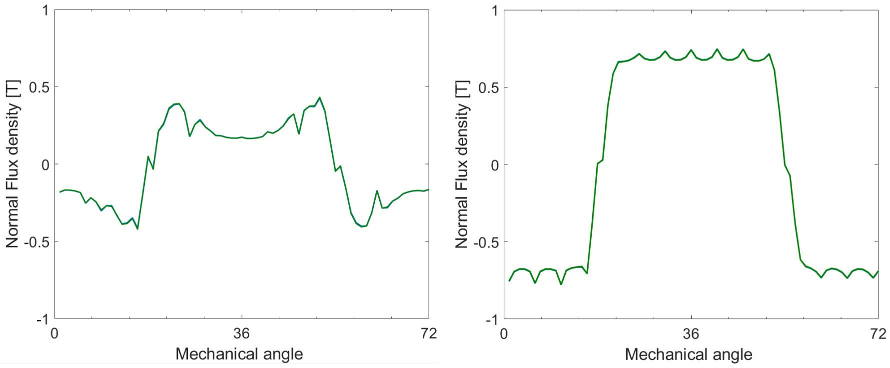

Fig. 3.18 Array of magnets solution: normal flux density for inset rotor with a row of 5 magnets in each rotor's slot. On the left picture the rotor is considered surrounded by air, , on the right one the iron is surrounded by iron. The normal flux density is calculated along 72 mechanical degree (two poles). The results are reported for the material M250-35A (blue line) and for M300-35A5 (green line).

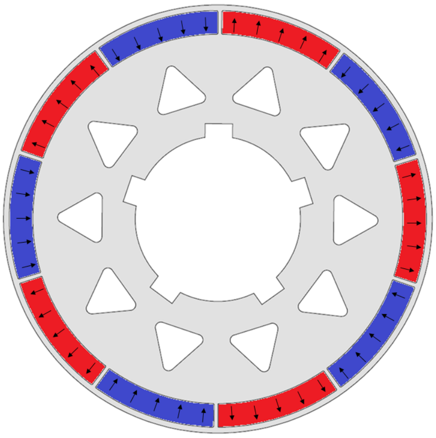

Fig. 3.19 Radial magnetization solution: cross section for PM-inset rotor with radial magnets for each rotor's housing slot.

by air (left picture) and for the rotor surrounded by iron (right picture). In Fig. 3.22 the normal flux density are reported with more detail for material M250-35A (blue line) and for M300-35A5 (green line). In Fig. 3.22 it is worth noticing the effect of the iron segment across two magnets.

Parallel magnetization

The effect of the external ring has been also analysed for magnets with parallel magnetization. The cross section of the PM-inset rotor used for the 2D FEA simulation

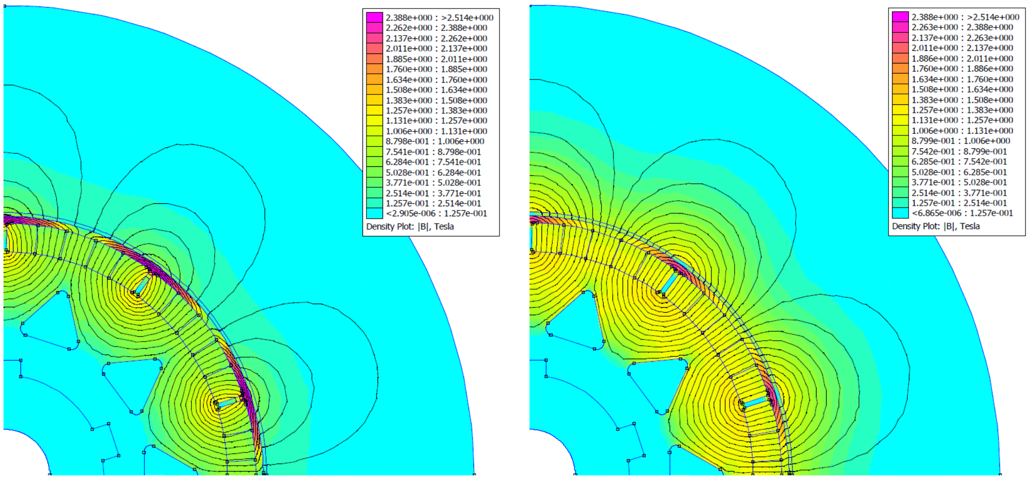

Fig. 3.20 Radial magnetization solution: Flux density plot for PM-inset rotor with radial magnets. On the left the flux density plot for the rotor surrounded by air, on the right is reported the flux density plot when the rotor is surrounded by iron. Materials are M250-35A (IEC 60404-8-4:1998) for the iron and NdFeB 38UH for the magnets

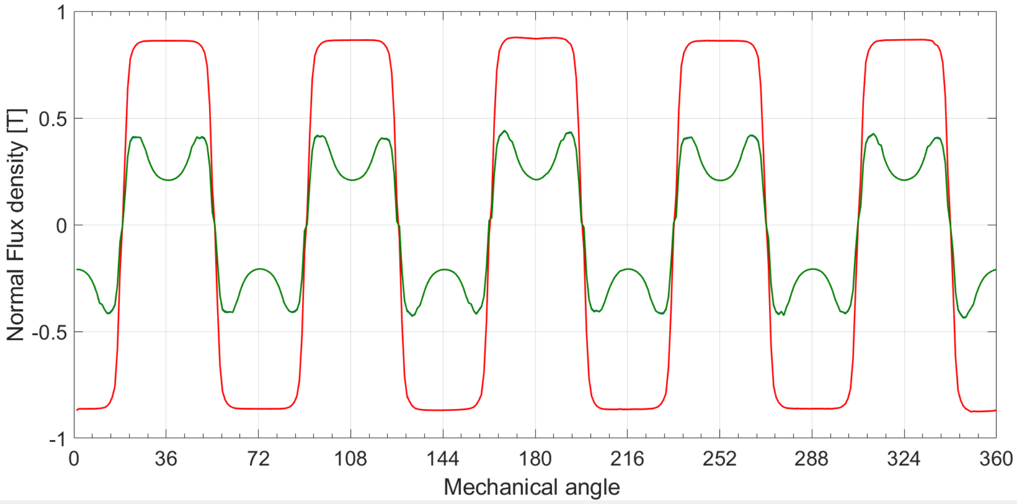

Fig. 3.21 Radial magnetization solution: normal flux density on the whole rotor surface. Green line is the normal flux density for the rotor surrounded by air. Red line is the normal flux density for the rotor surrounded by iron.

is reported in Fig. 3.23. The rotor is equipped by parallel magnetized permanent magnet. The flux density plot is reported in the left picture of Fig. 3.24 for the PM-inset rotor surrounded by air, and in the right picture of Fig. 3.24 for the rotor surrounded by an iron. According to the analysis previous reported, the normal flux density was evaluated on the external ring surface for both the solutions and the

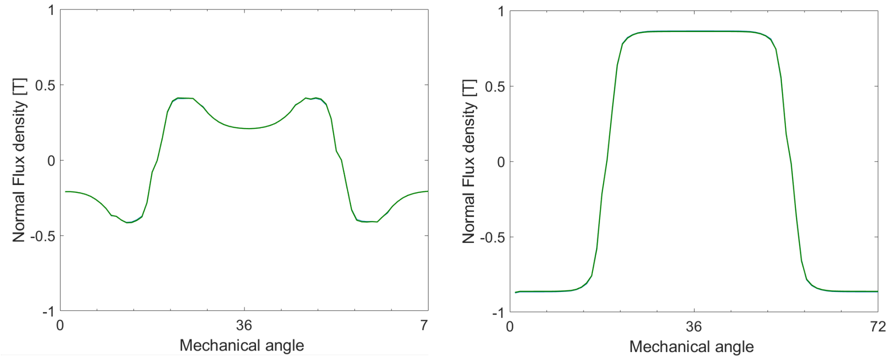

Fig. 3.22 Radial magnetization solution: normal flux density for PM-inset rotor surrounded by air (left picture) and for the rotor surrounded by iron (right picture). The normal flux density is calculated along 72 mechanical degree (two poles). The results are reported for the material M250-35A (blue line) and for M300-35A5 (green line).

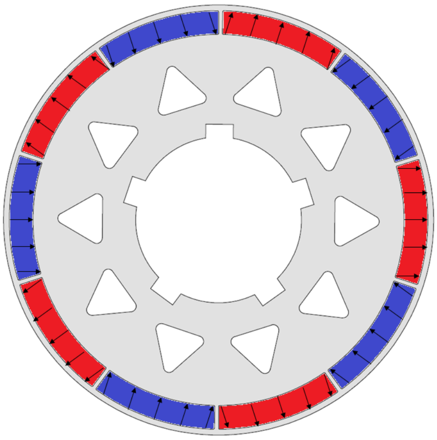

Fig. 3.23 Parallel magnetization solution: inset rotor with parallel magnetizations magnets for each rotor's housing slot.

results are reported in Fig. 3.25. The same results of Fig. 3.25 are reported with more detail in Fig. 3.26 for the rotor surrounded by air (left picture) and for the rotor surrounded by iron (right picture). In Fig. 3.26 the normal flux densities are reported for material M250-35A (blue line) and for M300-35A5 (green line).

Comparison

With the aim to compare the results obtained for the different magnets solution, the normal flux densities are reported in Fig. 3.27. In these pictures, the normal flux density evaluated on the rotor surface for a classical surface mounted permanent

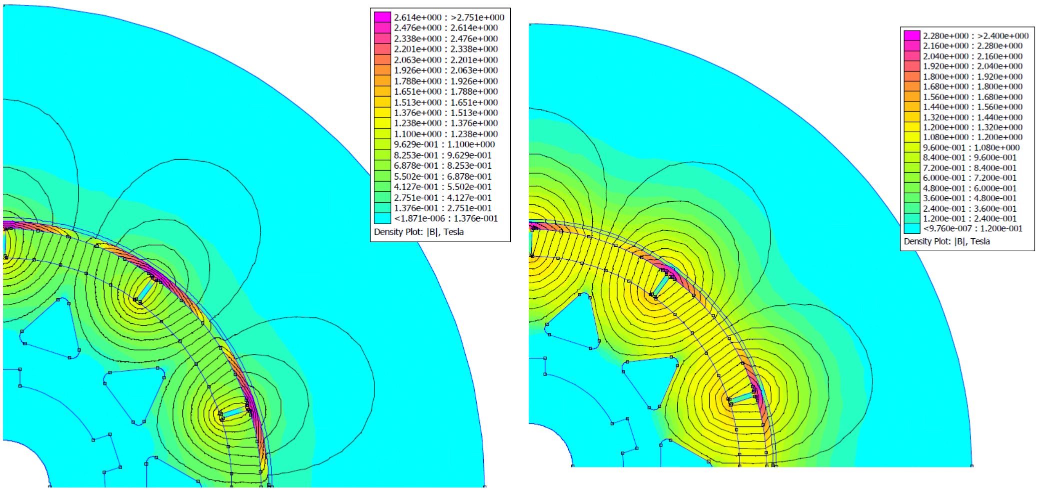

Fig. 3.24 Parallel magnetization solution: Flux density plot for PM-inset rotor with parallel magnetization magnets. On the left the flux density plot for the rotor surrounded by air, on the right is reported the flux density plot when the rotor is surrounded by iron. Materials are M250-35A (IEC 60404-8-4:1998) for the iron and NdFeB 38UH for the magnets

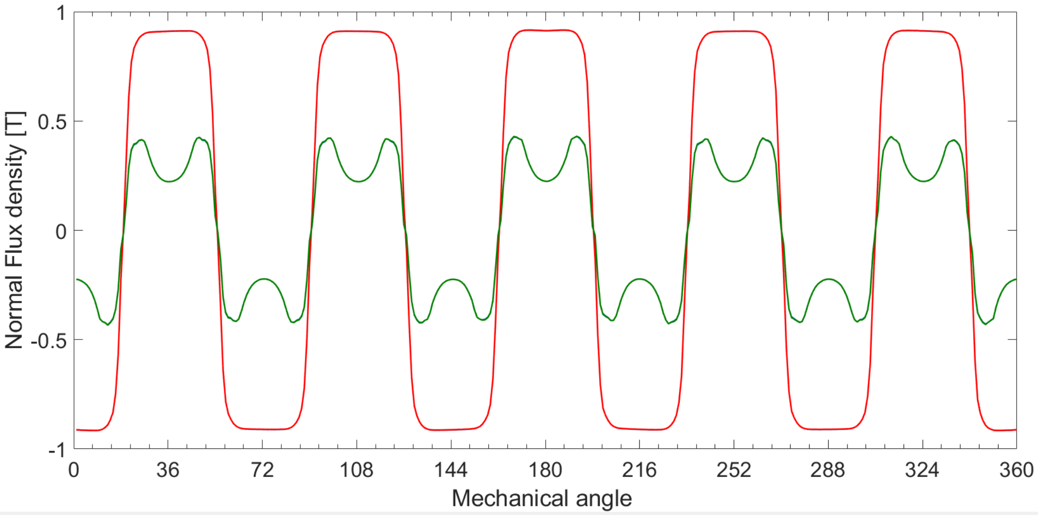

Fig. 3.25 Parallel magnetization solution: normal flux density on the whole rotor surface. Green line is the normal flux density for the rotor surrounded by air. Red line is the normal flux density for the rotor surrounded by iron.

magnet is also reported. The area of the magnets used in the SMPM, parallel, and radial magnetization solution is the same.

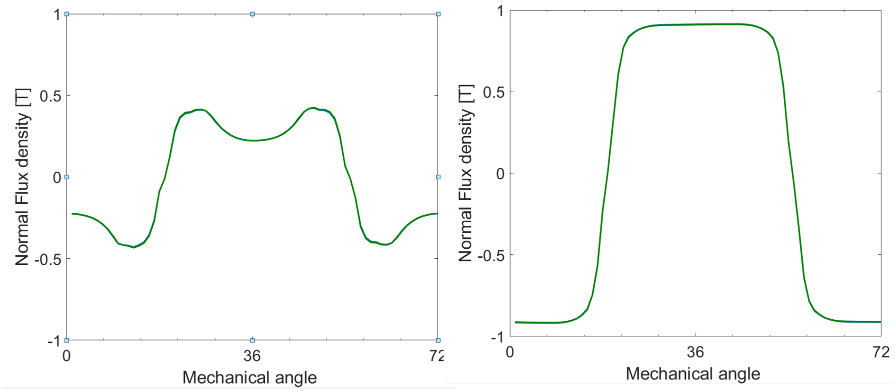

Fig. 3.26 Parallel magnetization solution: normal flux density for PM-inset rotor surrounded by air (left) and for PM-inset rotor surrounded by iron (right). The normal flux density is calculated along 72 mechanical degree (two poles). The results are reported for the material M250-35A (blue line) and for M300-35A5 (green line).

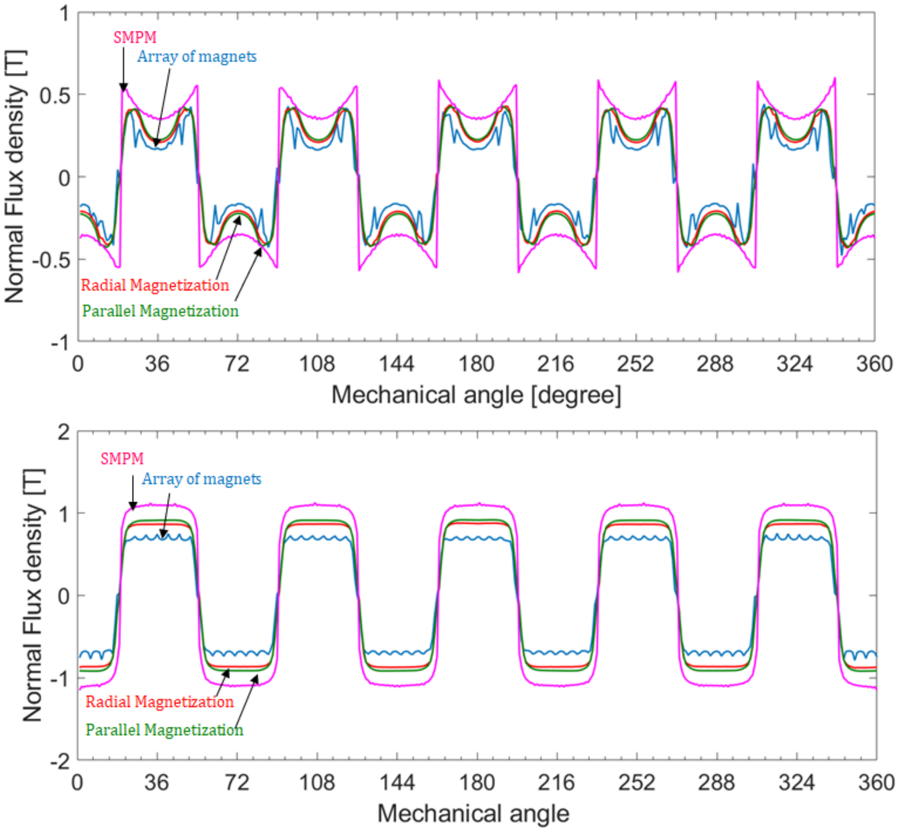

Fig. 3.27 Normal flux density for inset rotor surrounded by air along the rotor surface (up picture) and surrounded by iron along the rotor surface (down picture) for: magnets array solutions (blue line), radial magnetization (red line), parallel magnetization (green line), classical surface mounded (pink line).

3.3.3 Mechanical stress

The mechanical feasibility of the external ring was tested by FEA by using the simulation tool of the software SOLIDWORKS. A centrifugal force from 0 to 34.600 rpm was applied and the equivalent tensile stress (Von Mises stress), resultant of the displacement (URES) and the equivalent strain (ESTRN). The Von Mises Stress represent the ratio between the applied force and the area, the URES measures the displacement from the initial location of each element, and the strain (ESTRN) measure the change in length from applied force respect to the original length. It is worth noticing that the ratio between strain and stress is the Elastic Modulus or Young's Modulus. The highest tensile stress occurs in the piece of iron across two hosting slot. The yield strength is $4.5 * 10^8 N/m^2$. The main results are here reported Fig. 3.28, Fig. 3.29 Fig. 3.30 for a speed of 8.000 rpm. The maximum value of the equivalent equivalent tensile stress, URES and ESTRN were collected for different speeds and the results are reported in Fig. 3.31 and in Fig. 3.32. The dots identify the simulated results and the lines are obtained applying a cubic spline data interpolation to the simulation data. The red dots identify the speed for which the yield strength occurs. The factor of safety, that is the ratio between the maximum stress that the rotor can withstand and the maximum stress it will be subjected, at 8.000 rpm, that

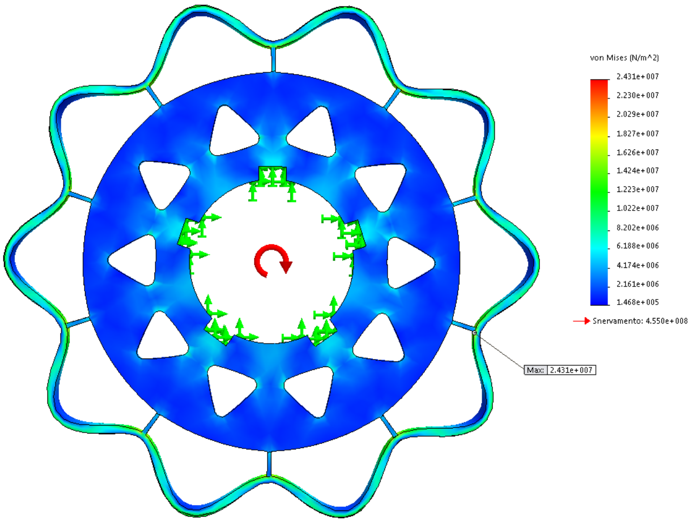

Fig. 3.28 Equivalent tensile stress plot for the M250-35A inset rotor under centrifugal force of 8.000 rpm

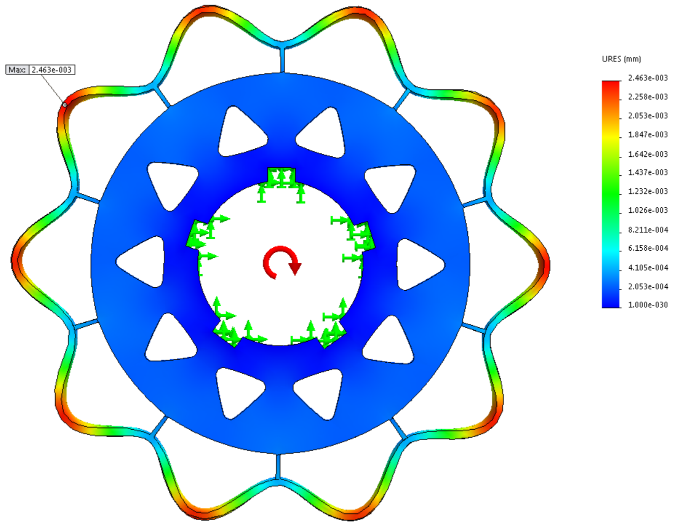

Fig. 3.29 Displacement from the initial location of each element plot for the M250-35A inset rotor under centrifugal force of 8.000 rpm

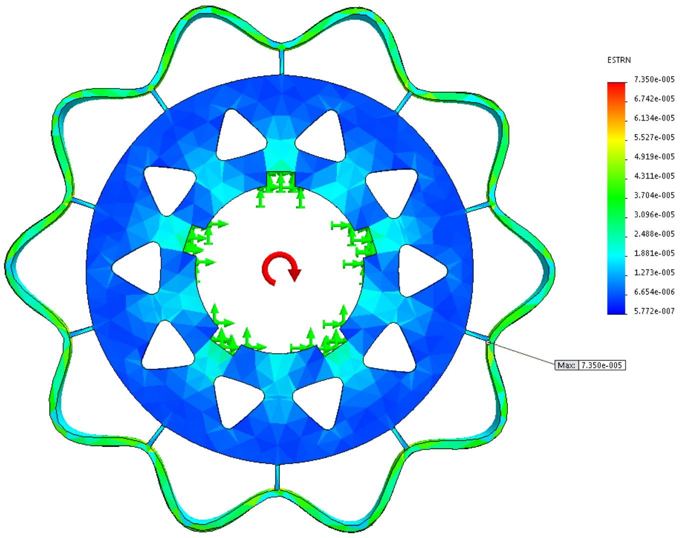

Fig. 3.30 Equivalent strain plot for the M250-35A inset rotor under centrifugal force at 8.000 rpm

is the maximum speed for the drive, is very high and no further verification were executed.

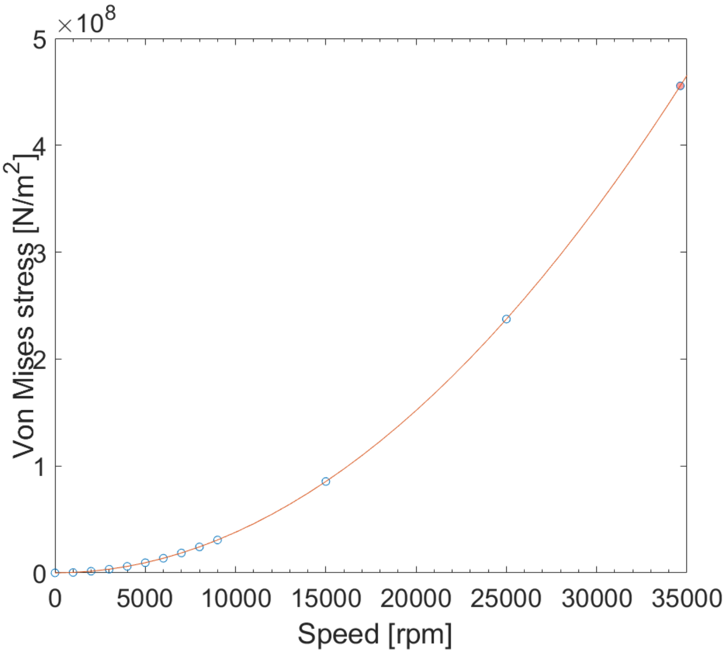

Fig. 3.31 Maximum equivalent tensile stress for the M250-35A inset rotor under centrifugal force for a speed that varies from 0 to 35.000 rpm

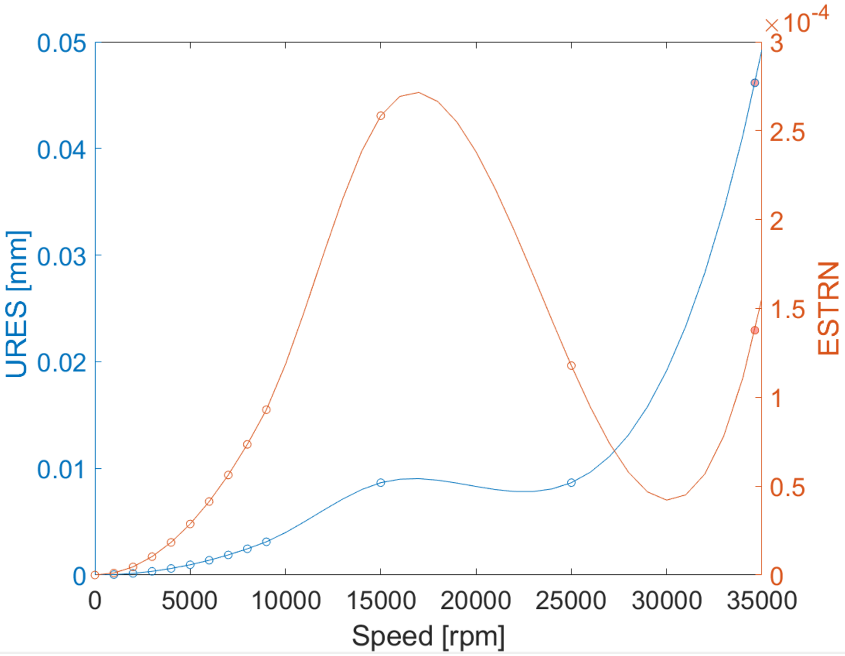

Fig. 3.32 Maximum URES (blue line) and maximum ESTRN (red line) for M250-35A inset rotor under centrifugal force for a speed that varies from 0 to 35.000 rpm

3.4 Performances

In the section 3.3, three different magnet configuration are considered for the rotor sheet in Fig. 3.14:

- array of magnets
- magnets with radial magnetization
- magnets with parallel magnetization

This section reports the performances expected from the three PM-inset magnets variant. The results are compared with the results of a classical SMPM solution. The machine machines are simulated in 2D simulation with FEMM 4.2 software. The entire machine must to be simulated due to the stator asymmetry. Time stepping simulation have been carried along 360 electrical degree, for the evaluation of the torque performances and fluxes and across 360 mechanical degree for the evaluation of the cogging torque. The main simulation results that are going to be considered are:

- linked flux spectrum
- mean torque
- ripple torque

The simulation were conducted for different current value and the results are collected.

3.4.1 Linked fluxes

The PM linked flux with each phases in the electric period at zero current is reported in Fig. 3.33 for the PM-inset solution with parallel magnetization. The PM linked flux spectrum of the single phase is reported in detail in the right picture of Fig. 3.33. The comparison between the harmonic spectra of the PM flux linkages at zero current for each tested solutions is reported in Fig. 3.34.

The same analysis is conducted at the nominal current in order to shown the sinusoidal behaviour of the flux linkage (Fig. 3.35). Fig. 3.35 shows the flux linkage with the nine phases at the nominal current and the harmonic spectrum of the flux linkage with the first phase for the PM-Inset parallel magnetization solution. The comparison between the harmonic spectra of the flux linkages at the nominal current for each tested solutions is reported in Fig. 3.36.

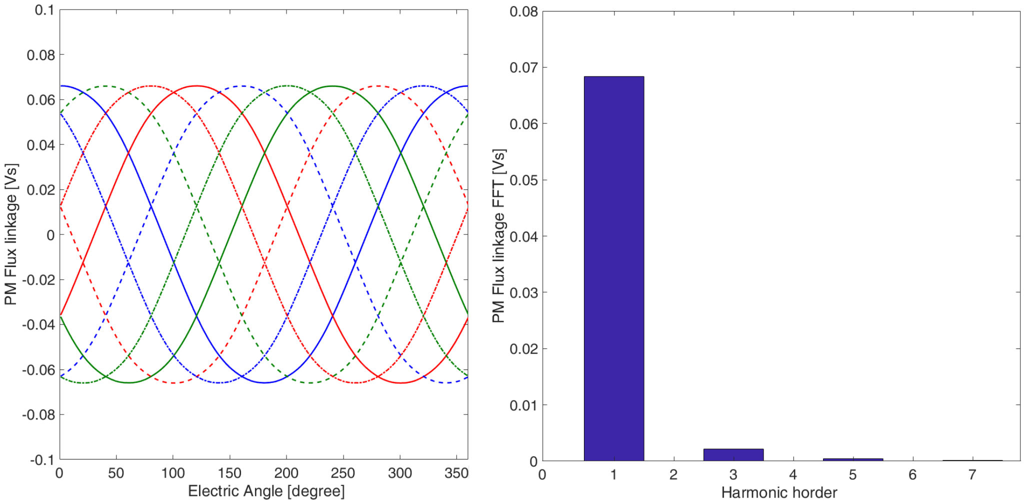

Fig. 3.33 PM-Inset Parallel Magnetization: On the left pictures the PM flux linkage with the nine phases, on the right the harmonic spectrum of the PM flux linkage with the first phase.

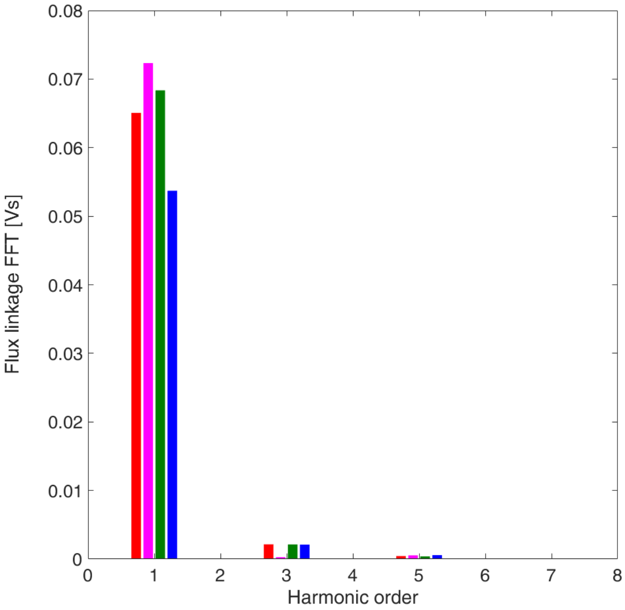

Fig. 3.34 FFT PM-flux linkage with the phase 1 comparison between solution at zero current: PM-inset with array of magnets(blue line), radial magnetization (red line), parallel magnetization (green line) and for the classical SMPM (pink one)

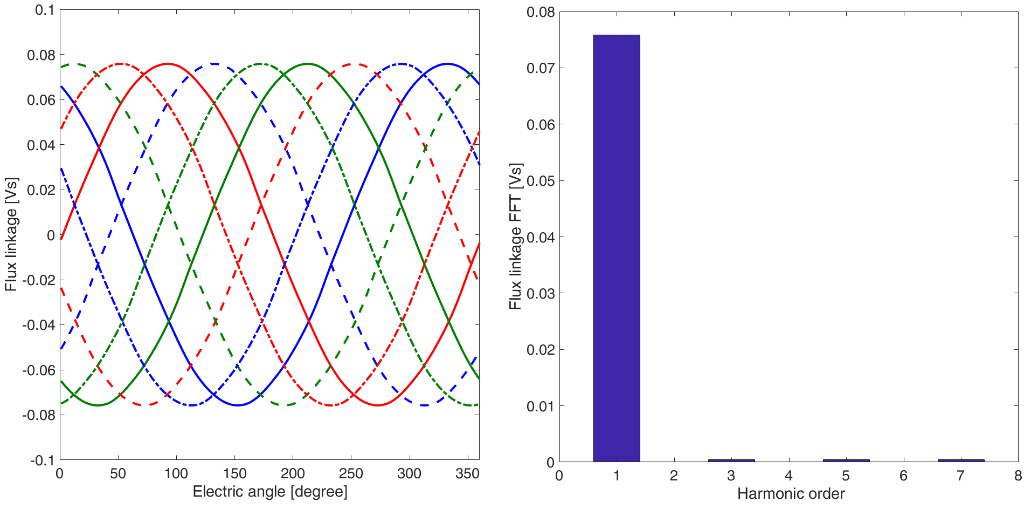

Fig. 3.35 PM-Inset Parallel Magnetization: On the left pictures the flux linkage with the nine phases at the nominal current, on the right picture the harmonic spectrum of the flux linkage with the first phase.

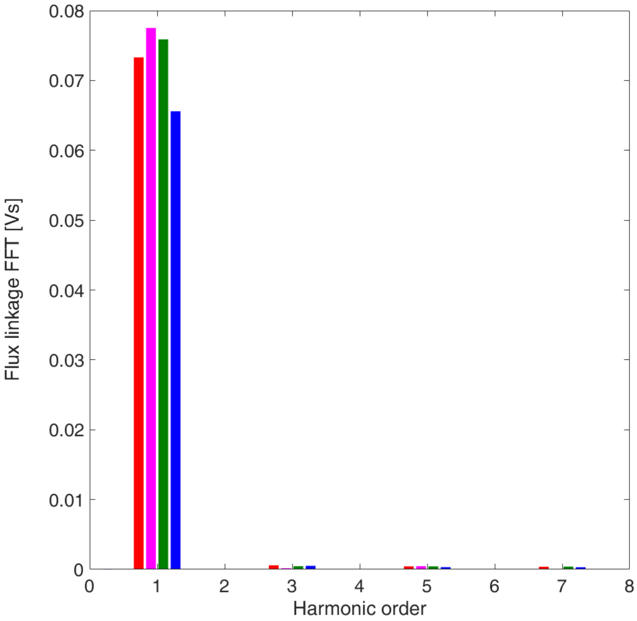

Fig. 3.36 FFT PM-flux linkage with the phase 1 comparison between solution at the nominal current: PM-inset with array of magnets(blue line), radial magnetization (red line), parallel magnetization (green line) and for the classical SMPM (pink one)

3.4.2 Torque performance

The mean torque for different currents value is reported in Fig.3.37 for each analysed solution. The current value is varied from 0.1 to 1.3 times the nominal current. As demonstrate from the preliminary analyses in the section 3.2.2 the main contribution of torque ripple occurs at the frequency 18^{th} on the electric period also for the PM inset version. Fig.3.38 and Fig.3.39 report, for each solution analysed, the values of the 18^{th} harmonic of the torque ripple vs different currents value. The torque performances at the nominal current are reported in Fig.3.41. In Fig.3.41 is reported

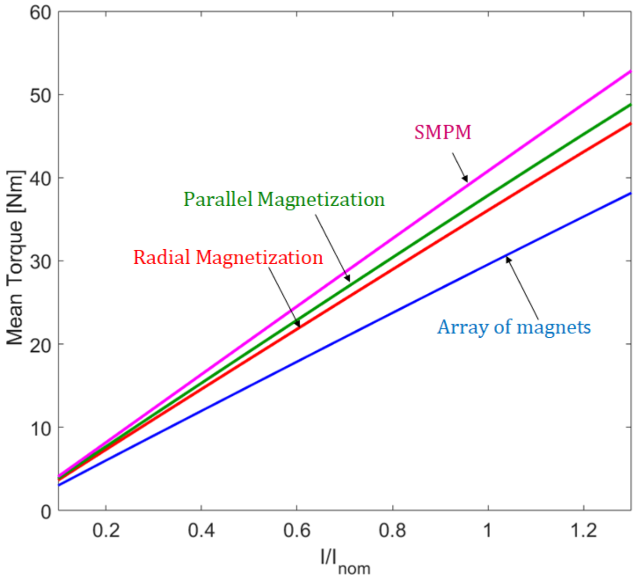

Fig. 3.37 Mean Torque [Nm] vs % of the nominal current for the solution PM-inset with array of magnet(blue line), radial magnetization (red line), parallel magnetization (green line) and for the classical SMPM (pink one).

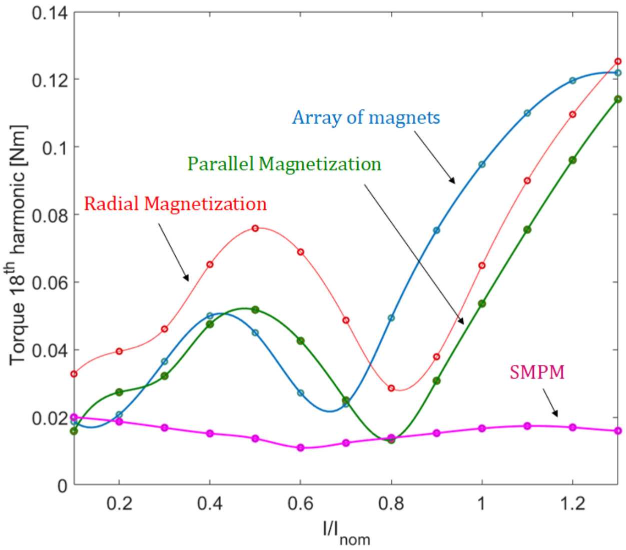

Fig. 3.38 18th torque component [Nm] vs % of the nominal current for the solutions: PM-inset with array of magnet(blue line), radial magnetization (red line), parallel magnetization (green line) and for the classical SMPM (pink one).

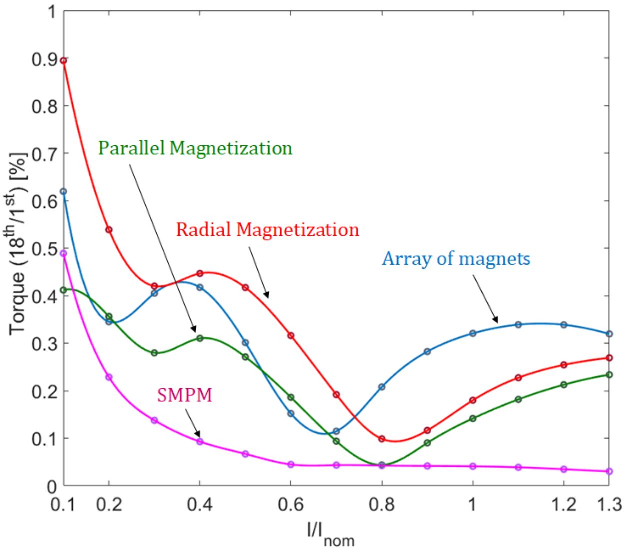

Fig. 3.39 18th torque component in % of the mean torque vs % of the nominal current for the solutions: PM-inset with array of magnet(blue line), radial magnetization (red line), parallel magnetization (green line) and for the classical SMPM (pink one).

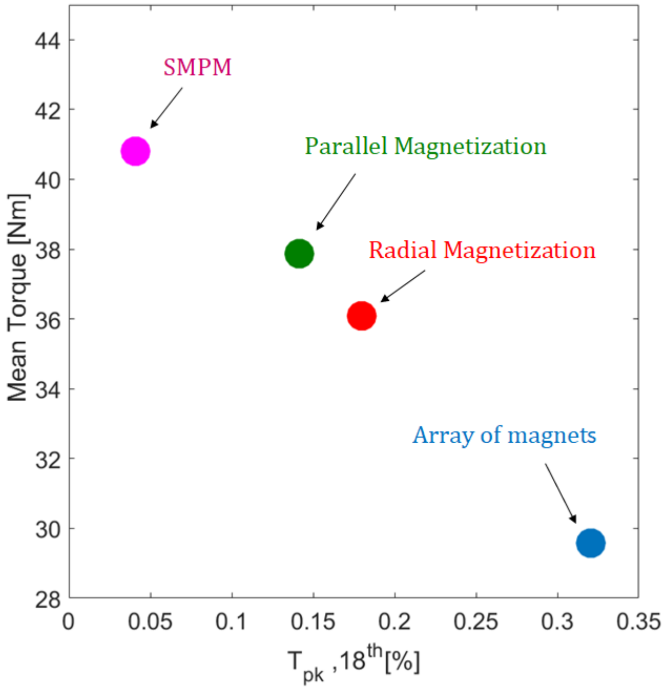

Fig. 3.40 Mean torque vs $18th$ torque component in % of the nominal torque for the solutions: PM-inset with array of magnet(blue line), radial magnetization (red line), parallel magnetization (green line) and for the classical SMPM (pink one).

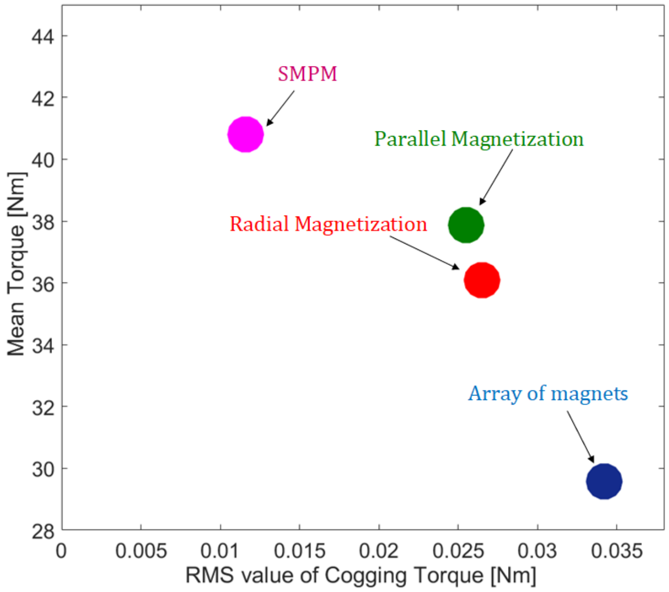

Fig. 3.41 Mean Torque vs cogging torque component in % of the mean torque for the solutions: PM-inset with array of magnet(blue line), radial magnetization (red line), parallel magnetization (green line) and for the classical SMPM (pink one).

3.5 Testing

The aim of the tests is to evaluate the torque and the torque ripple for the multiphase machine designed at different current amplitudes. Fig. 3.42 and Fig.3.43 show the experimental set-up.

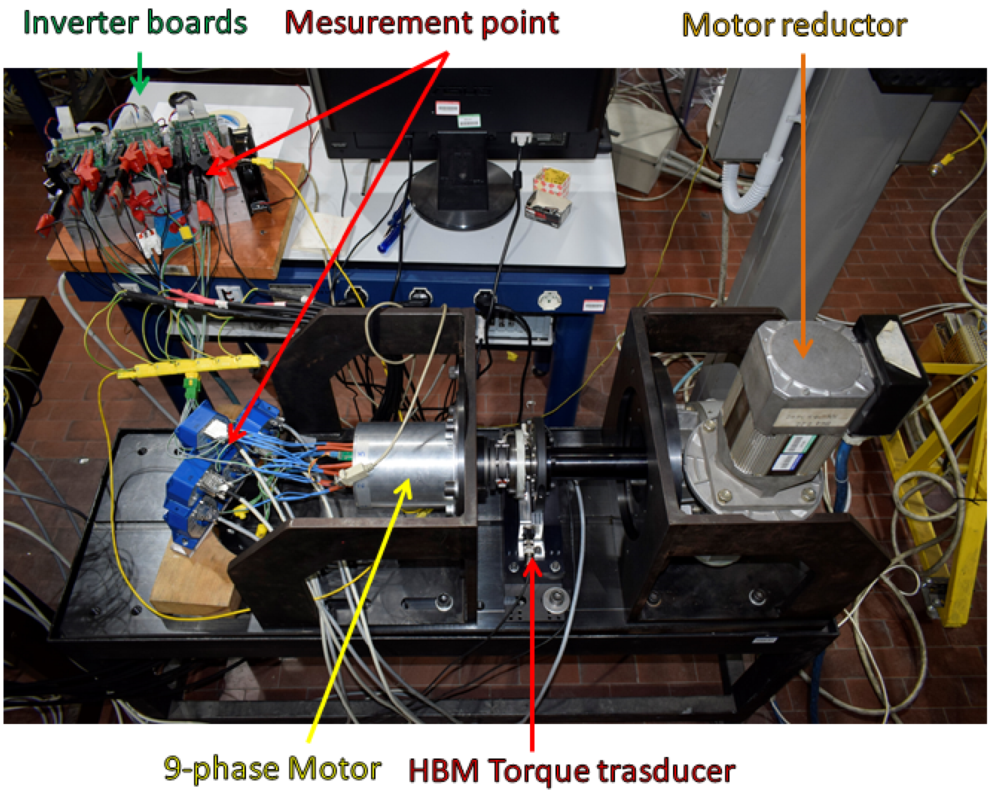

Fig. 3.42 Laboratory set-up: shaft connection.

The test bench is composed by: the nine phase motor under test, a AC motor reductor and the acquisition system. The acquisition system includes an HBM T40B torque transducer and an HBM Gen3i data recorder[47]. The torque, the currents and the voltages have been acquired with a sampling rate of 2MS/s. In order to guarantee a good resolution of the torque, the speed has been settled to $10 rpm$. The motor under test is controlled by a triple 3-phase power converter IGBT based. The converter is managed by a control unit, that communicate with an host computer. An user interface has been realized on the host computer in order to manage the tests.

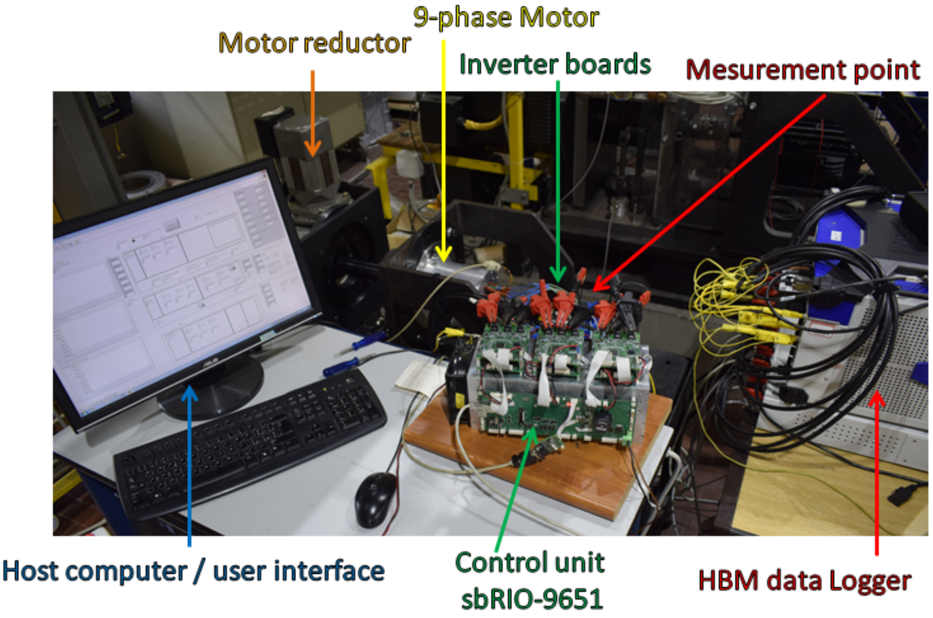

Fig. 3.43 Laboratory set-up: control system.

3.5.1 Power electronics and control

The converter structure is a dual-triple-3-phase converter. The power electronic was designed in order to control two triple-3- phase motors. The whole structure has been designed as combination of modular parts. Each module is a 3-phase converter constituted by a low level control board and a power board based on an intelligent power module, both are visible in Fig. 3.44. The modules have been realized in order to meet the following maximum specifications: 20A peak phase current, 400V

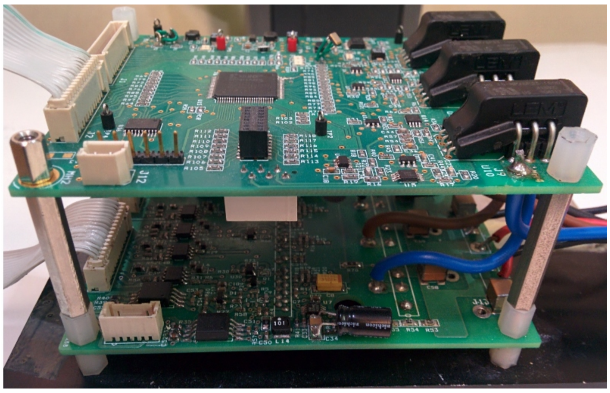

Fig. 3.44 Converter module: Low level control board and power board.

max DC-link voltage, 20kHz max PWM frequency. The modules have a reduced dimension (PCB 102.24 mm x 78.61 mm). The intelligent power module adopted is the ST microelectronics STGIPL30C60, 30 A 600 V IGBT based [13]. In Fig. 3.44 is possible to see TDK CKG57N 450 V 2.2uF capacitors and LEM HO 15NP ±37.5A 250 kHz. The maximum current tested is equal to 18 A and not 25A.

The whole application requires the presence of an high-level controller to manage the power conversion. A single control board unit manages the three low level control boards. The single control board unit is a board that host the master of the system that is a sbRIO 9651. The sbRIO include a real time and a FPGA modules (Xilinx Zynq All Programmable System on Chip (SoC)).

The architecture of the control realized from scratch for embedded control, is reported in Fig. 3.45. The master communicate by Serial Peripheral Interface (SPI) in a synchronous way with the low level control boards. Each power module is controlled by an Spartan3A FPGA (Field Programmable Gate Array) Xilinx XC3200AVQ100 that performs all measurement tasks.

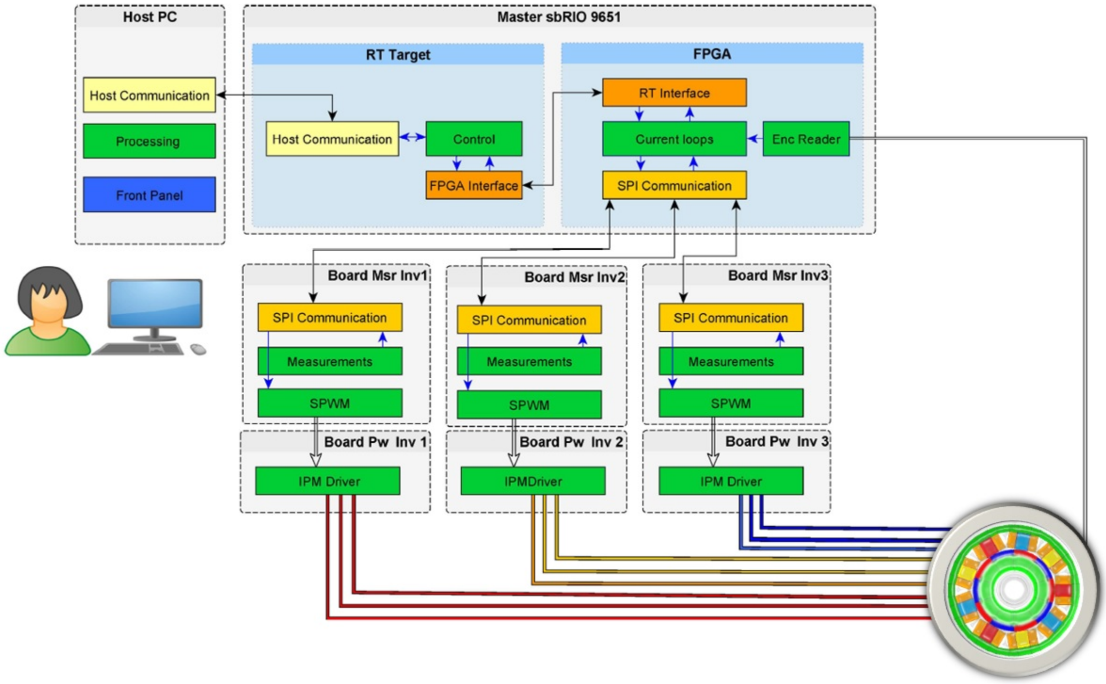

Fig. 3.45 Control architecture.

Three independents currents controls are realized on the master control unit. The master control unit receives the measurements from the low level control board and the signal from the encoder. The measurement are used in order to realize three field oriented controls. The measurement and the modulation signals must to be communicated through a strong communication protocol. The speed of the communication is set to 20MHz 12 bit based. In detail the control unit and the low level control unit communicates each others:

- MOSI: Status command
- MOSI: Modulation indexes
- MOSI: Angular phase shifting between PWM
- MISO: Status
- MISO: Current measurements
- MISO: Voltages

all of this information are exchanged nine times in the PWM period. The structure proposed is very flexible and has been used in other research activities. The same structure was used in order to realize an interleaved boost converter for charging a vehicle during dynamic inductive power transfer [48]. The firmware of the single control board unit (the master) was developed from scratch in LabVIEW environment. The main task of each modules are evidenced in Fig. 3.45. An user interface has been realized on the host computer in order to manage the tests. Trough the control panel of the user interface is possible to control and check the status of the power converter, to imposed the d-q reference currents (one for each board) and define the phase shifting between PWM carriers (more details are reported in Chapter 4). In addition all the measurement acquired by the measurement board, and used for in control, are visible on the screen.

3.5.2 Experimental Results

The tests are executed in order to measure the torque, mean value and torque ripple, for different current amplitudes. Three current controls, one for each stars, are driven. In this way is possible to control the three different stars of the machine independently. In figure Fig. 3.46 is shown the torque behaviours when the three stars are sequentially powered. The sequence is: the first star of the motor is powered on, then the second one is powered on and then the third one. The same dq-reference is imposed for each control. The peack current in each phase current $15.9A$. In the

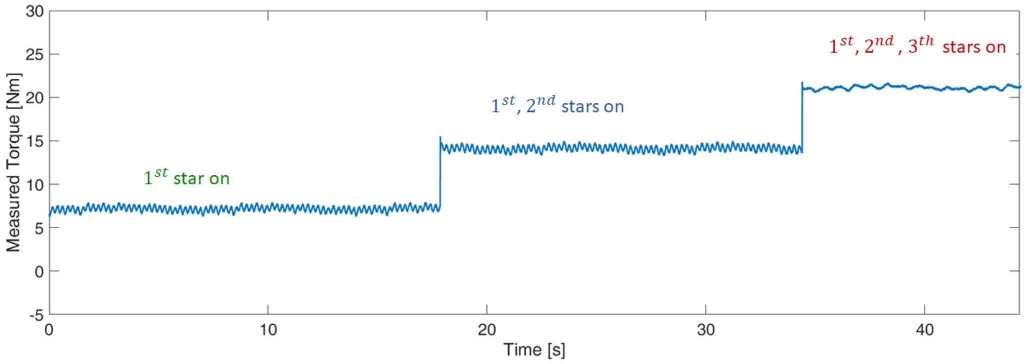

Fig. 3.46 Torque evolution powering each stars in sequence: the first star of the motor is powered on then the second stars is powered on and then the third one.

same way it is possible to remove the power supply from each star independently. The shut-down sequences is : the first star is power off then the second one and then the third one Fig. 3.47. All the stars contribute in the same way to produce the torque.

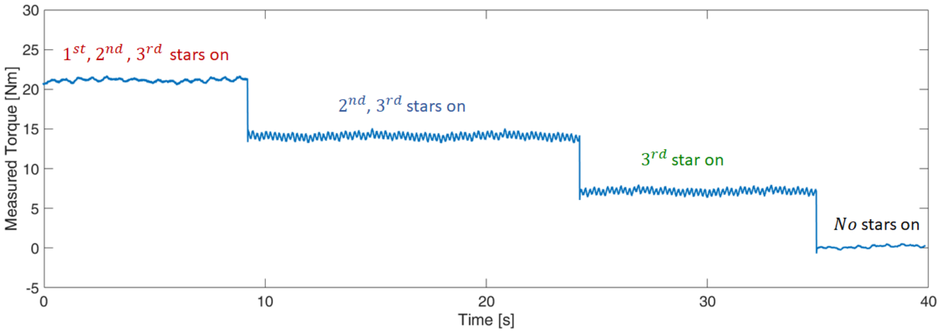

Fig. 3.47 Torque evolution powering off each stars in sequence: the first star of the motor is powered off then the second stars is powered on and then the third one is powered off.

The torque measurements during an electric period, for the 4-operating conditions, are reported in Fig. 3.48. The torque ripple, when only one or two stars are powered on, is mainly related to the $6th$ harmonic on the electric period ($30th$ harmonic on the mechanical period). This torque ripple component is not present any more when

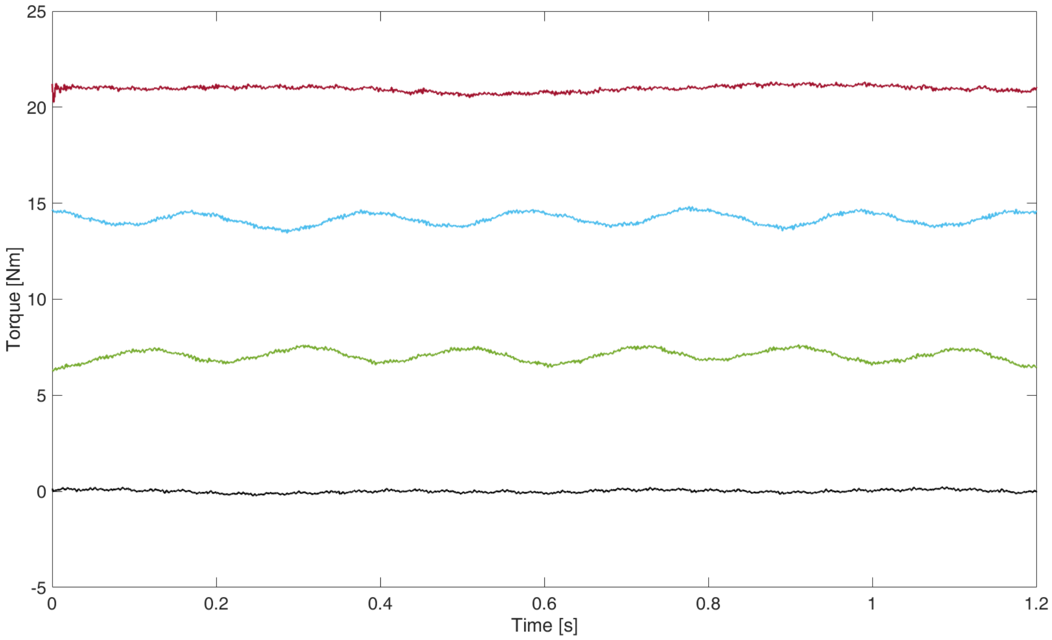

Fig. 3.48 Torque evolution in the electric period for four operating condition: one star on (green line), two stars on (blue line), three phase on (red line). The black line report the torque ripple measured when all the stars are power off.

the three stars are powered, as expected from the simulations and from the torque ripple modelling. The harmonic spectrum of the torque ripple measured during the four operating conditions is reported in Fig. 3.49. We can try to categorize the torque ripple harmonics in:

- harmonics not multiple of p
- harmonic multiple of p

The harmonics not multiple of p result from a not perfect centring of the rotor. The harmonic multiple of p are more interested. Some of that, like the $30th$, $60th$ and the $90th$ were predicted by FEA and by the torque modelling. The others like the $5th$ and the $10th$ are proportional to the amplitude of the currents and can probably result form the radial forces due to the asymmetry of the stator. Otherwise the amplitude of these harmonics is very low. Only a qualitative analyses can be done, being the amplitude of the torque ripple very close to the resolution of the torque-meter. In Fig. 3.51 the torque ripple harmonic spectrum is reported for different values of the phase currents. Fig. 3.51 reports the Root Mean Square (RMS) value of the

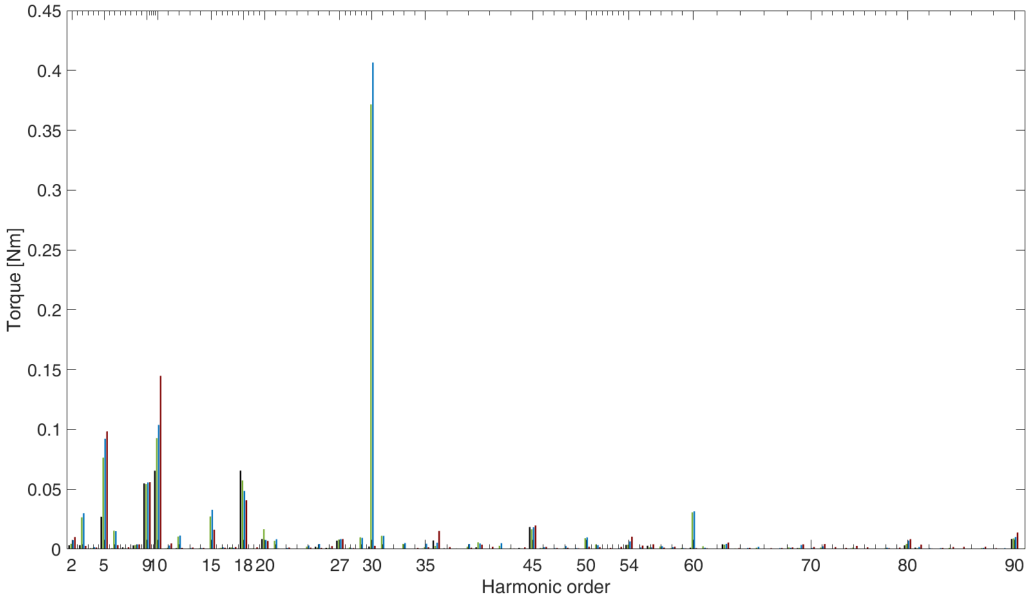

Fig. 3.49 FFT Torque ripple in the mechanical period for the four operating condition: one star on (green bars), two stars on (blue bars), three phase on (red bars). The black bars report the torque ripple measured when all the stars are power off.

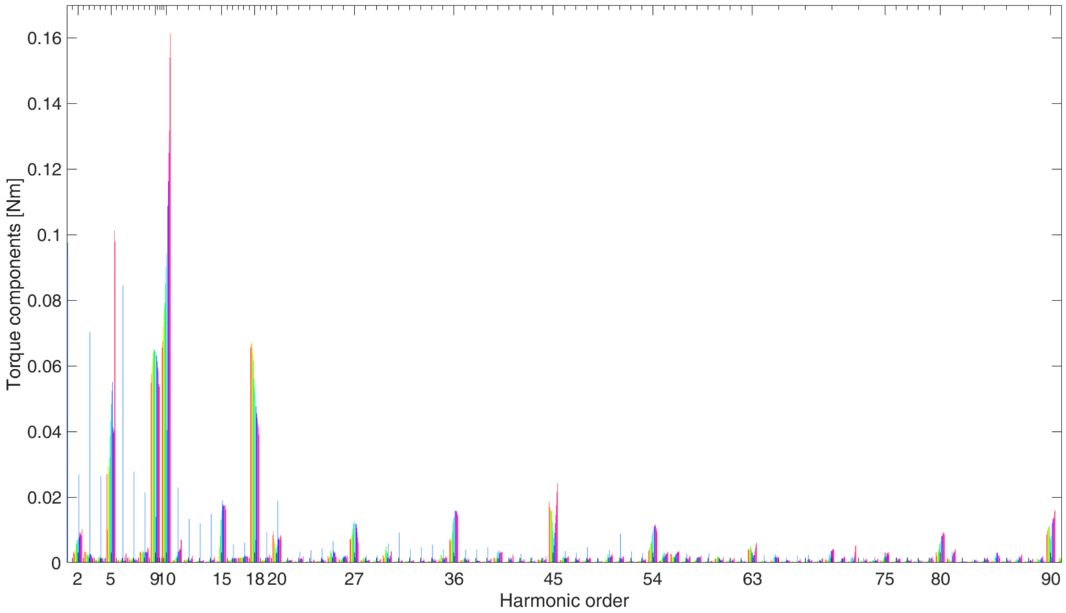

Fig. 3.50 FFT Torque ripple in the mechanical period for different currents. The amplitude of the current span from 0 to 18A from the left to the right bars

measured torque normalized respect to the mean torque. This allows to have an idea about the impact of all the ripple harmonics. The red circles represent the measured point. It is possible to see that the torque ripple RMS value exponentially decreases with the amplitude of the currents. The fitting curves (blue line) is obtained excluding from the fitting function the outliers measured points. The mean value of the torque for different phase current is reported in the top picture of Fig. 3.52. The bottom picture of Fig. 3.52 shown the pk-to-pk torque ripple value in p.u of the mean torque for different amplitudes of current. In these pictures the measurement data are represented by red circles and the fitting curves are reported by blue lines. With the aim of comparison the simulation results are reported by green lines. Comparing the 2D FEA with experimental data it is evident a discrepancy in the mean value of the torque. Typically the 3D FEA allows to reduce the difference between the numerical solutions and experiments. This can be related to the border effects. On the other hand , considering the torque ripple measurement, an error between experimental and simulations is evident at low current when the cogging torque and the presences

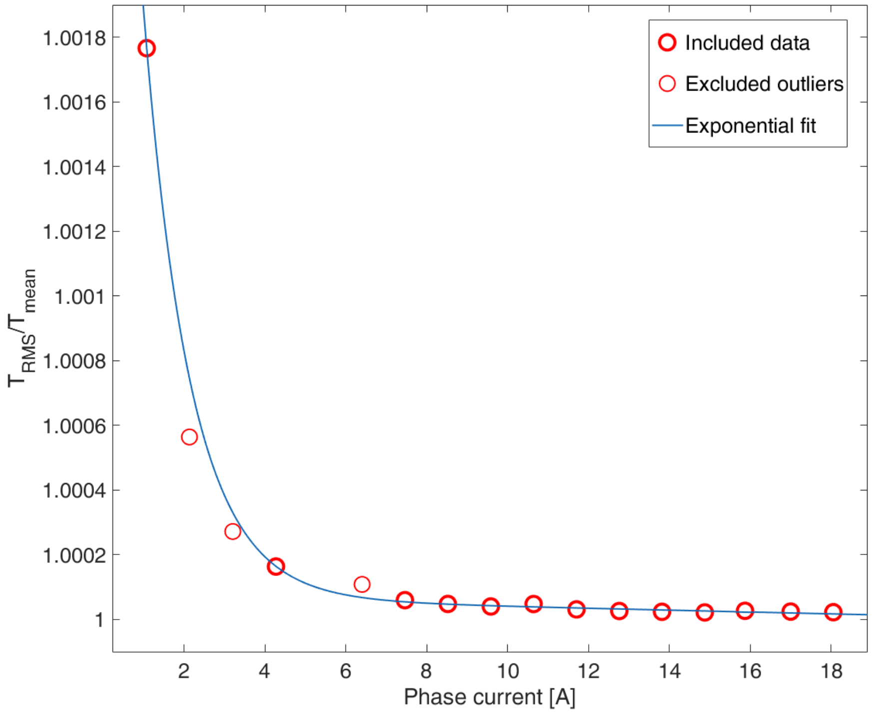

Fig. 3.51 RMS value of the torque pu respect to the mean torque vs the current applied.

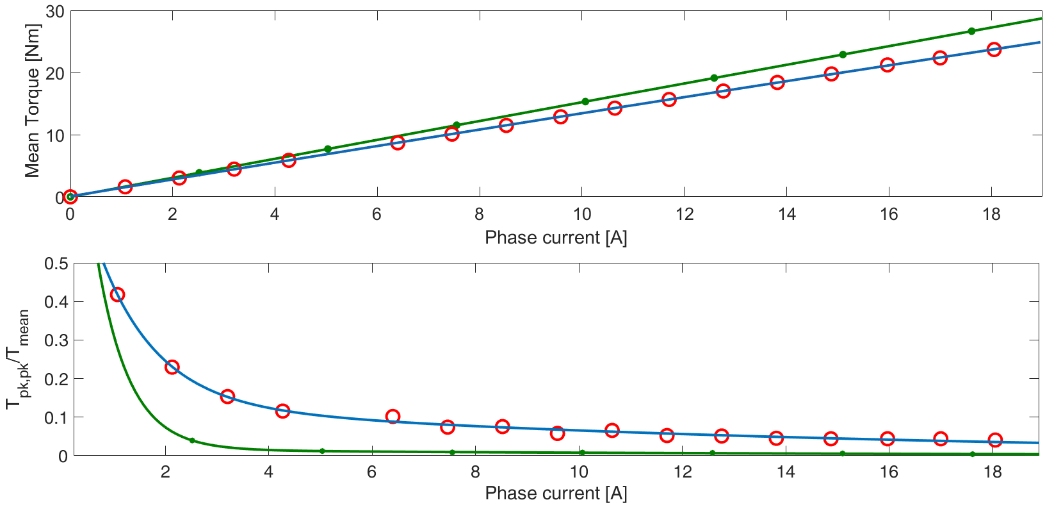

Fig. 3.52 Experimental VS FEA results: Up picture represents the mean torque vs phase current amplitude, while the bottom picture reports the pk to pk torque ripple value normalized to the mean torque vs phase current amplitude.

of the radial forces are predominant. The errors become lower for greater current levels.

3.6 Conclusions

In this chapter the main issues tackled in the design of a nine phase machine are reported. Between the possible solutions a 9 slot-10 poles machine has been chosen. The design results in a open slot stator, tooth-coil wound. A particular tooth shaping (that realize a not constant air gap) has been chosen in order to reduce the torque ripple. An PM-inset rotor topology has been chosen, and different magnet configuration tested. The PM-inset sheet has been studied from the mechanical point of view by FEA. The results shown how the solution is feasible in terms of stress with a very high factor of safety. FEA were conducted in order to valuate the performance of the machine. The FEA highlighted how for this solution the flux linkage is almost sinusoidal and the torque ripple is very low. The external ring affect the torque performances in therms of mean torque and in terms of torque ripple that results greater compared to the classical SMPM version. Between all the possible solutions the more promising solution in terms of performances is the PM-inset version with customized magnet with parallel magnetization. Otherwise the solution characterized by an array of magnet in the rotor slots can allows to reduce the cost. In the end the machine designed was tested in a reduced operating area. Some differences between experimental and simulation results occurs and are mainly related to constructive defect in the mechanical machine realization, and limits in the simulations conducted. In particular 3D simulations can allows to obtain results more similar to the experimental data, and multiphysics simulations can allow to investigate more the effect of the radial forces on the torque ripple. Otherwise, despite its simplicity, the machine tested results in a very low torque ripple solution with value of pk-pk torque ripple under 1 Nm for each operating condition tested. A more accurate mechanical design and realization can be done in order guarantee a better centring of the rotor eliminating some harmonics from the ripple. Passing from the $3-3-10-1$ solution to the $3-3-10-2$ solutions allows to eliminate any problem related to the radial forces.

Chapter 4

Control strategy to reduce the DC-link stress

Part of the work described in this chapter has been previously published in [35] and in [27]

4.1 Introduction

The DC-link capacitor it is an important element in an electric drive for voltage source converter, both in terms of cost and space [49]. The energy density of the applications typically required electrolytic capacitor that are typically bulky and heavy. Currently the DC bus capacitor contributes up to 20% of the cost and weight of an inverter and up to 30% of an inverter's volume [50]. Moreover the life time of electrolytic capacitor usually decides that life time of the overall system [51].

The reliability requirements in the field of electric vehicle (EV) and hybrid electric vehicle (HEV) has lead to the strong use of film capacitors. For this technology the large ripple currents become even more problematic in high temperature environments. The impact of the capacitor design is so important that, according with the Oack Ridge from national laboratories, "can presents a significant barrier to meeting the U.S. DRIVE targets for cost, volume, and weight established by the U.S. Department of Energy and its industrial partner" [50].

The DC-link capacitor can performs several functions. The main role of the capacitor it is to allow for compatible hard switching commutations firstly , to allow for the impulsive converter currents supply without involves the main supply, to absorbs the energy of the drive in case of fault, to assure energy for power peaks and to protect the converter from the transient voltages peaks if connected to a power grid.

The capacitor size depends on: the capacitor current, its main frequency components, and the DC-link operating voltage. As well explained by Kolar and Round in [52], the most critical parameter that affect the Dc-link capacitor life is the working temperature. The thermal analysis strongly influences the capacitor design. In fact for an aluminium electrolitytic Capacitors a reduction of the 10% of the rated voltage leads to a reduction of 60% of the failure rate but the working life of the capacitor became double each times that the working temperature decrease of 10°C . A method for predicting the expected life of bus capacitors is reported in [53] together with the capacitor model. The core temperaturate, that affect the DC-link capacitor life it is strictly related to the capacitor RMS (ICrms) other than the ambient temperature [52]. Therefore a reduction of the RMS capacitor current reflecting a reduction of the dimension of the capacitor or a increment in the capacitor lifetime.

The chance to reduce the design of the capacitor is an important issue because allow to reduce the cost, space and weight and , often, the physical shape of the capacitor itself can lead to difficult practical solutions resulting in large commutation path. In addition the presence of bulky and heavy capacitor can reduce the feasibility of converter motor integration [54]. The techniques that allow the reduction of the dimension of the capacitor are very appreciated in electric vehicle market where the requirements are weight, dimension and low cost.

The goal of the research is related to the investigation of the benefit introduced by the multiphase drives from the converter point of view introducing a simple modulation strategy that allows to reduce the DC-link stress. In this context the research it is interesting because introduces some aspects able to give a further boost to the use of multi-n-phase drives on the electric vehicles.

After a description of the background technique the modulation strategy is presented with simulation and experimental results for the specific drive solution (nine phase one). Than a short analyses is reported for the sectored multiphase solution.

4.2 Background

As previoous said the ICrms current affect the dimension of the capacitor. In order to offer a guideline for the dimension of the capacitor a lot of paper has been produced in the past for analytical calculation of the rms current for n phase system. In [52] the author offer a simple analytical expression for the DC-Link current in a 3 phase converter. In the paper the output current ripple has been neglected, this lead to an average error of 8% of the evaluation of the current ripple respect to experimental results. A similar analysis has been conducted for multi phase drives [55].

Technique to reduce the DC-link stress

A lot of paper in the last decades focused on reducing DC-link stress . In [56] has been proposed a method to reduce the DC-link stress by variation of the DC-link link voltage through a PWM current source rectified and holding the modulation index constant in adjustable speed application. The authors start from the model proposed [53] in order to calculate the losses. A very appreciated, althought dated work is the paper of Kim and Sul [51] in which they propose a control algorithm for AC/DC/AC converter without electrolytic capacitor but distributed ceramic capacitors.

In [50] the authors proposed a traction drive solution that use a sectored three phase machine supplied by two converter (a six phase motor supplied by two inverter like a three phase one) in which the PWM has been interleaved in order to reduce the DC-link stress obtaining a reduction of the 60% of the volume capacitors, the results for three different angle between carrier has been theoretically proposed. A complete analysys has been also offered for sectored three phase machine supplied by three inverter in [38] offering a design point for this particular sectored three phase solution and is reported in the following.

Also a proposal that use multilevel multiphase induction motor drives it is proposed in [57].

In the field of multiphase drives in 2015 different works introduced the phase shifting between carriers in order to reduce the DC-link stress for a six-hase machine [58] and for a nine-phase machine [38], in order to reduce the harmonic distortion and power losses [59][60] or to improved the quality of the line-to-line output voltages [61].

4.3 Proposed Modulation Technique

The basic idea it is to exploit an additional degree of freedom, the phase shifting between PWM carriers for the different n-phase inverters in order to allow the reduction of the DC-link rms current. The novelty of the research it is mainly related to the investigation of the best angle of shifting between carriers in order to reduce the DC-link rms current in multi-3-phase drives. In addition, the analysis carried out shown that no variation in the control strategies and in the optimal angle are needed under fault conditions. This means that the phase shifting between carriers appear like a real additional degree of freedom offered by multi-n-phase drives. In this way the authors offer conscious guideline for the correct choice of the DC-link capacitor suggesting a reasonable design point. The control strategy can be extended to other multiphase drive solutions but, different results about the best phase shifting between angle occur.

4.3.1 Modulation technique

What here is defined as PWM control strategy is an extension of the Sine triangle PWM (SPWM) with the common mode injection calculated from the balanced envelopment [62] where more than one carrier have been used for different section of the multiphase converter.

A 10 poles permanent magnet surface mounted (PMSM) machine, 9 coils double layer concentrated windings can been considered. According to the algorithm proposed in 1 this machine is called $3-3-10-1$, meaning 3 stars of 3 phases, 10 pole, repeated 1 times, in the multi-n-phase version. As base machine, rotor and stator structures are reported in Fig. 4.2a. It is possible to observe that the structure is the same of the well known $q_{3/10}$ as a resulting 3-phase double layer machine, defined by the parameter q (number of slot-per-pole-per-phase) and by the number of permanent magnets (poles). Since in the next this will be identified as the three phase counterpart the winding configuration is reported here Fig. 4.1a.

The control strategy proposed consider to supply the triple-3-phase machine by a triple-3-phase converter with coils connections as in Fig. 4.2 and the center taps insulated from each other.

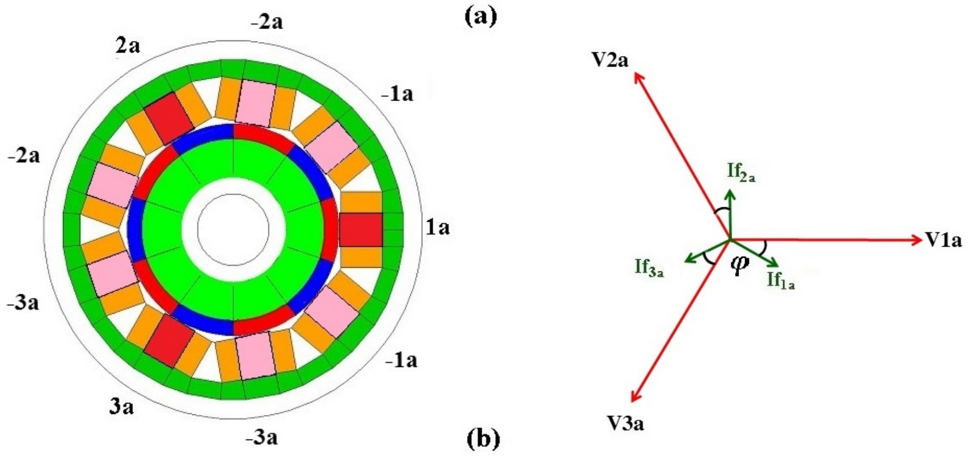

Fig. 4.1 Case **I**: base machine (**a**) and phasor diagrams (**b**). Red stator teeth are the axes of the coil supplied by the converter **a**.

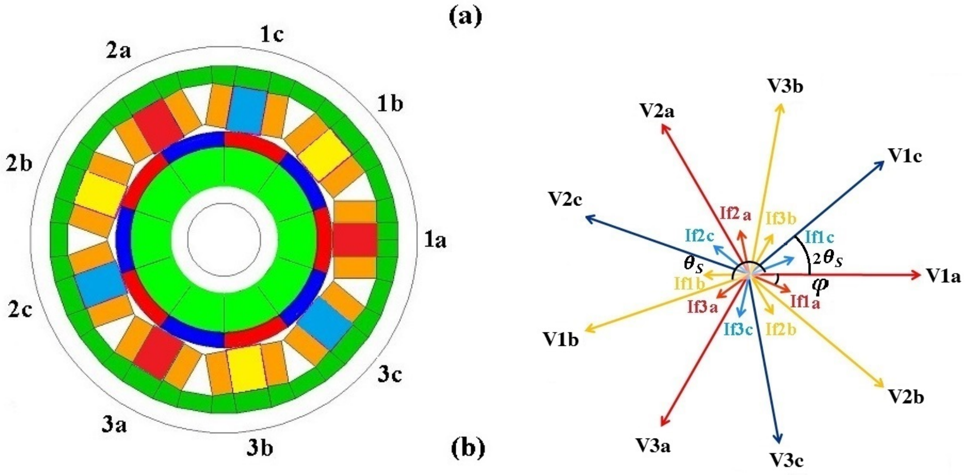

Fig. 4.2 Case **III**: base machine (**a**) and phasor diagrams (**a**). Red teeth and red star supplied by the converter **a**, yellow teeth and yellow star supplied by the converter **b**; blue teeth and yellow star supplied by the converter **c**.

A 9-phase converter (one leg for each coil of the base machine) like the one in Fig. 4.3 has been adopted. The whole structure, in this latter case, has been designed as combination of modular parts. Each module is a 3-phase converter constituted by a control board and a power board based on an a standard control and modulation technique. The modular structure of the converter offers different choices in how to supply the different machine portions. Then for the triple-3-phase solution the 3 coils of the first star are supplied by the first inverter, the second star by another and

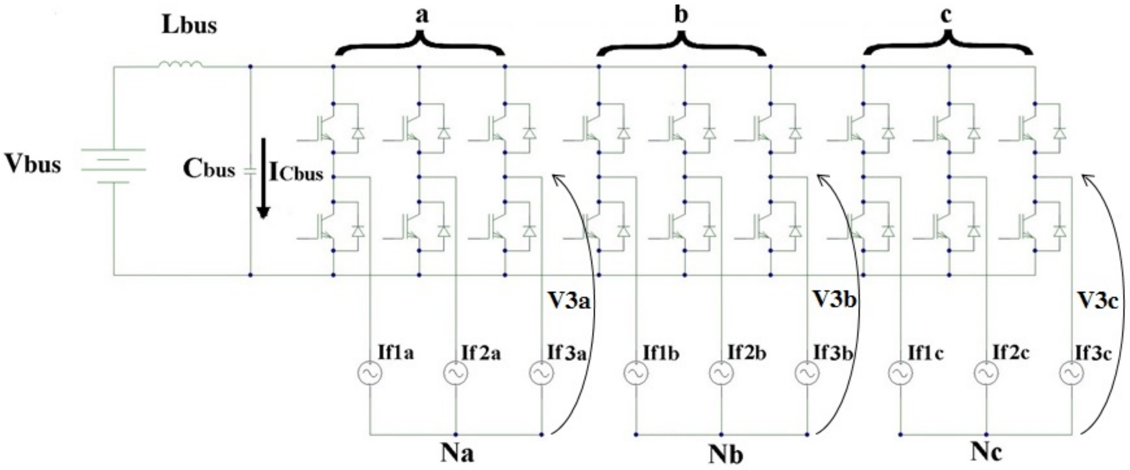

Fig. 4.3 Triple-3-phase converter IGBT based. The converter is obtained from the composition of three 3-phase converter modules. Each 3-phase converter (**a**,**b**,**c**) supplies a 3-phase star of the machine.

so on (Fig. 4.3).
The 3 converters have to obtain 3 voltage stars as in Fig. 4.2b. The electrical displacement between two sequential stars is defined by θ_S electrical degrees [25] (citare la formula quando ci sarà),

$$\theta_S = \frac{N_P \cdot \pi}{N_C \cdot N_S} \tag{4.1}$$

where:

N_C: Number of Coils that constitute star (considering always one coil per phase, here $N_C = 3$),

N_S: Number of Stars (here $N_S = 3$),

N_P: Number of Poles (i.e. PM) (here $N_P = 10$)

For a 3-3-10-1 machine the $\theta_S = 200$ electrical degree.

The drive control block scheme is reported in Fig. 4.4. Three equal *dq* current current loop with three equal references are generated from a lookup table (LUT), one for each star.
In the proposed control scheme, three different synchronous carriers signals have to be used in the PWM control of the three sections. Triangle carried with rising and falling symmetrical edge have been used in this work.

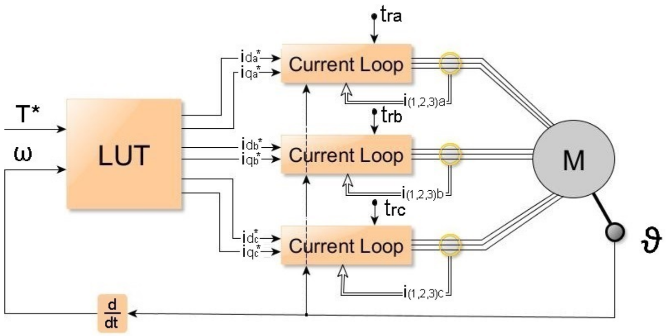

Fig. 4.4 Control block scheme for the triple-3-phase drive: each current loop have **the same** reference current.

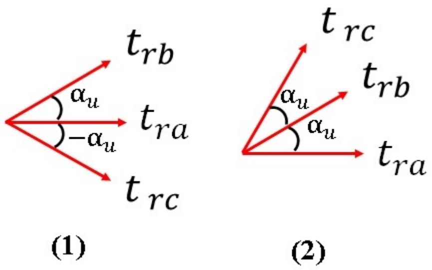

Fig. 4.5 Phase shifting between carriers signals: the results of the analysis are the same regardless of the reference (1) and (2) if the three PWM carriers signals have equal mutual phase shift.

Different relationships between the carriers signals can be chosen. In this work is discussed the effects of a specific simple relationship between PWM carriers: the three carriers have the same mutual phase shift, as show in Fig. 4.5. In Fig. 4.6 an example of the relationship between carrier has been reported for an angle $\alpha_u = 45$ degree).

It is worth noticing that the introduction of a displacement between PWM carrier could also positively affect output torque ripple [63]. In this analysis the authors focused on the effect of the control technique on the converter side also testing the effectiveness on a test bench.

In the following section a detailed analysis based on simulations of the effect on the DC-link capacitor bench of the just described PWM strategy is proposed.
The results will be compared with the one of the classical 3-phase drives. Reference case is then the case **I**, i.e. the 3-phase machine supplied by a single inverter with a simple current control in SPWM. In general $I_{C_{rms}}$ decreases as the number of

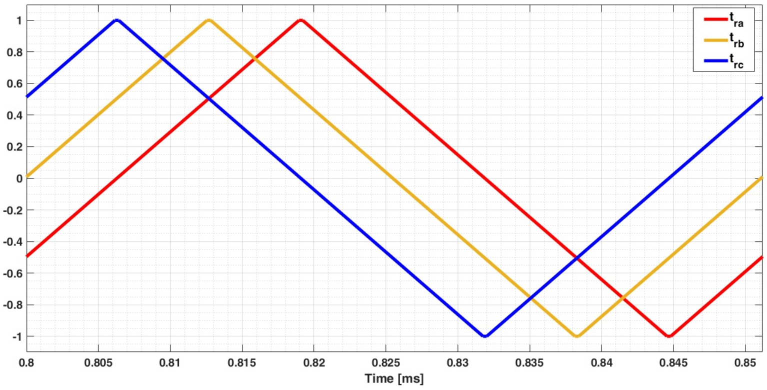

Fig. 4.6 Carriers t_{ra},t_{rb},t_{rc} related to an angle of $\alpha_u = 45 degree$.

phases increases [55],[64], and the value of the $I_{C_{rms}}$ changes for different operating conditions.

As an example, for a three-phase machine supplied by a single inverter, the simulated $I_{C_{rms}}$ values for different operating condition are reported in Fig. 4.7 [52].

4.3.2 Simulation Results

In order to have a complete description, simulations have been carried out for the 3-phase drive and for the triple-3-phase one.

The software used in simulation is Pspice. The switching frequency is fixed to 20kHz and dead time are not considered.

In the 3-phase solution, a single inverter supplies a motor simply modelled by current generators. No ripple current effect is considered at the simulation level.

In order to reduce the mutual coupling between phases belonging to difference stars a double layer tooth-coil open slot stator solution has been chosen. For the specific motor design chosen finite element analyses have been conducted. The value of the mutual inductance is equal to $1.37mH$ that is about the 12.5% of the self inductance, equal to $10.9mH$. Instead in a closed slot solution the value of the mutual inductance is equal to 97% of the self inductance. In Chapter 2 and in Chapter 3 has been demonstrate that also a so simple stator structure allows to obtain a very low torque ripple solution. In the triple-3-phase solution each module of the triple-3-phase converter (Fig. 4.3) supplies one 3-phase star as in Fig. 4.24 and Fig. 4.2. Discarding the output current ripple in a current loop control the motor can be modelled by current generators. This approximation can in general be done as shown in [52] and in [65]

The variations of the following parameters have been considered:

- Modulation index ($M = 2VPhase/Vbus$)
- Displacement between PWM carriers (α_u)
- Phase between voltage and current (VI-phase).

Steady state simulations have been performed in all of the possible combinations of the above parameters. Considers different values of VI-phase mean evaluate the effect of the proposed technique through different operating condition like that one related to the constant power speed range in which the rotation of the current vector lead to a variation of the power factor of the machine. The $I_{C_{rms}}$ values and their harmonic spectrum for all the operating points have been stored and here proposed. All results have been normalized to ease the comparison. DC-link rms currents have been normalized to the rms phase current value of the 3-phase case. The modulation index M can vary from 0 to $2/\sqrt{3}$ according to the linear inverter range extended through the injection of the proper common mode [62]. Data processing has been performed to search for the worst case in all conditions so to guide for the DC-link capacitor choice. In the following the more representative results are proposed.

3-phase counterpart

3-phase machine $q_{3/10}$ powered by a single-3-phase converter as in Fig. 4.1 For the case **I** the values of the $I_{C_{rms}}$ for different operative conditions are collected in the Fig. 4.7 like in [52]. The capacitor design value is $I_{C_{rms}} = 0.64$ p.u

Triple 3-phase

In the triple-3-phase case $I_{C_{rms}}$ also depends on M and VI-phase. In Fig. 4.9 it is possible to see the benefits of the introduction of the displacement α_u. The results for different value of M are reported in the pictures Fig. 4.8

The graph in Fig. 4.9 refers to the M value for which the greatest variation with α_u in the $I_{C_{rms}}$ values occurs. It can be noticed that, for the chosen M value, the $I_{C_{rms}}$

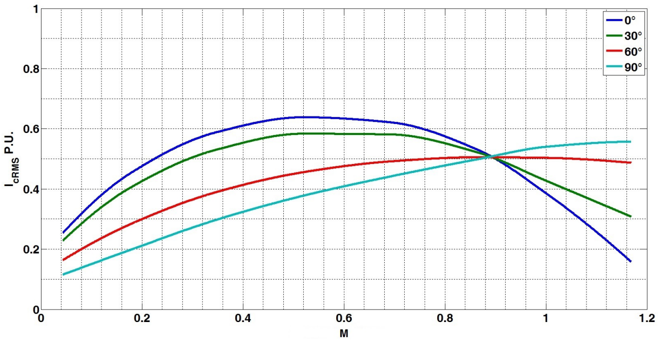

Fig. 4.7 Case **I** 3-phase machine $q_{3/10}$ 3-phase powered: $I_{C_{rms}}$ variation depends on EMF for different value of electric angle between voltage and current (VI-phase).

is barely constant independently of the VI-phase for 4 values of α_u: 50, 70, 110, 130 carrier degrees approximately.

For different operating conditions the minimum of $I_{C_{rms}}$ moves and the trend become barely flat as the M increases as it will be shown in detail in the experimental part.

In Fig. 4.10 a 3D picture collects all results for all simulated M, α_u and VI-phase values.

Once known the drive operating condition it is possible to define the DC-link design point. To make the analysis independent on any particular application, it is possible to assume that the drive could explore all the operating conditions (all VI-phase/M couples). It is possible to see how for the triple-3-phase machine it is sufficient to calculate the value of $I_{C_{rms}}$ for VI-phase 0 and 90 in order to calculate the worst case design. In Fig. 4.11 and Fig. 4.12 iso-level curves report the value of the $I_{C_{rms}}$ in p.u respect to the rms value of the phase current. It is possible to see how the design point it is influenced by the operating conditions. If the VI-phase variation it is limited from 0 to 30 electrical degrees two equivalent α_u angle are 60 and 120 degree but if the operating range of the drive it is not well defined or the VI-phase moves from 0 to 90 electrical degrees the design point moves and a optimal angle can be chosen around 45 degree. Data in Fig. 4.10 are then analysed in order to identify the locus of greatest values of $I_{C_{rms}}$ versus α_u in all operating conditions. Fig. 4.13, in detail, represents this locus for each α_u carrier displacement. The mutual phase shifting between PWM carriers α_u for which the minimum of the greatest $I_{C_{rms}}$ occurs can be chosen as the optimal PWM displacement angle. In [35] the analysis on the simulated results includes the evaluation of the DC-link current harmonic

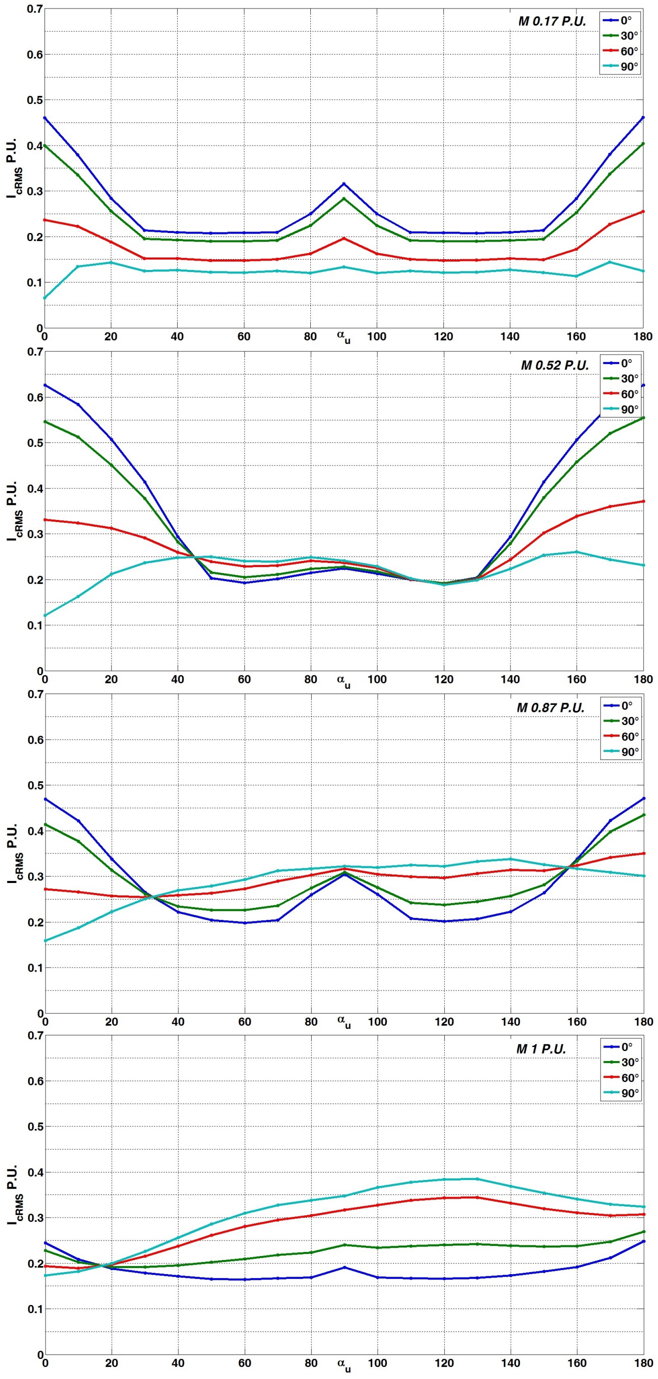

Fig. 4.8 Case **III** triple 3-phase machine triple 3-phase powered: $I_{C_{rms}}$ variation depends on M for different value of electric angle between voltage and current (VI-phase).

contributions for different α_u. The design point chosen ($\alpha_u = 45$ degrees) is the point where the first and the second harmonic contributions meet each other.

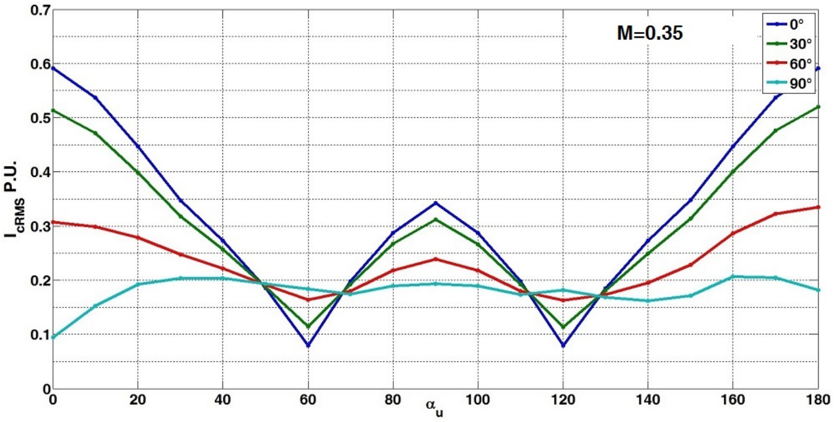

Fig. 4.9 Simulated results triple-3-phase machine: $I_{C_{rms}}$ for different displacement between PWM carriers signals (α_u) and different V-I phases. At $M = 0.35$ there is the larger variation of $I_{C_{rms}}$ as function of α_u.

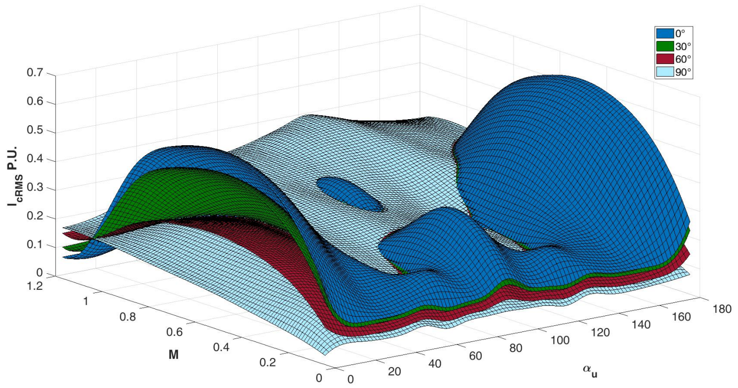

Fig. 4.10 Simulated results: triple-3-phase phase machine: values of $I_{C_{rms}}$ with the variation of M and α_u. Each surface represents a different value of VI-phase.

The same analysis, described above, has been extended for α_u larger than 180 degree and the collected results suggest a mirror behaviour. More, for V-I phases greater than 90 degree electrical degrees graphs regress overlapping previous curves. As an example, the $I_{C_{rms}}$ resulting for 100 electrical degrees is equal to the one for 80 el. deg. and for 180 el. deg. the curve overlaps the 0 one.

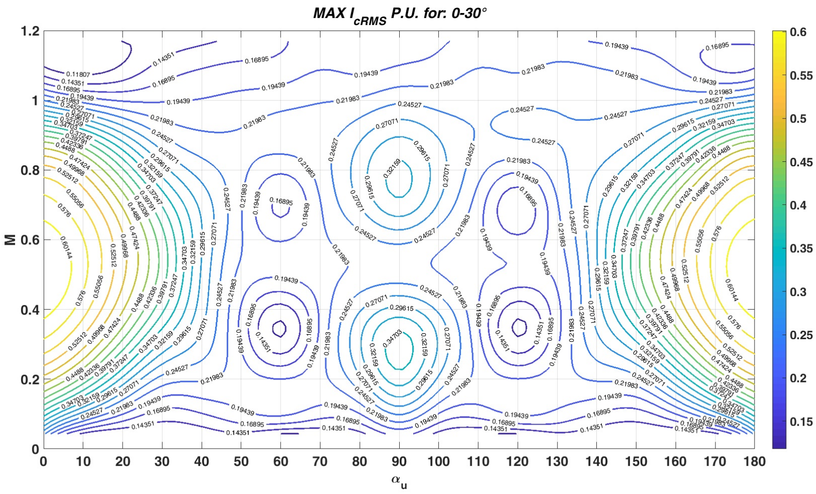

Fig. 4.11 Simulated results: Isolevel of greatest $I_{C_{rms}}$ in p.u respect to the rms value of the phase current worst case vs α_u for all M value. The different figure represent the locus of the greatest $I_{C_{rms}}$ values for a specific operating range.

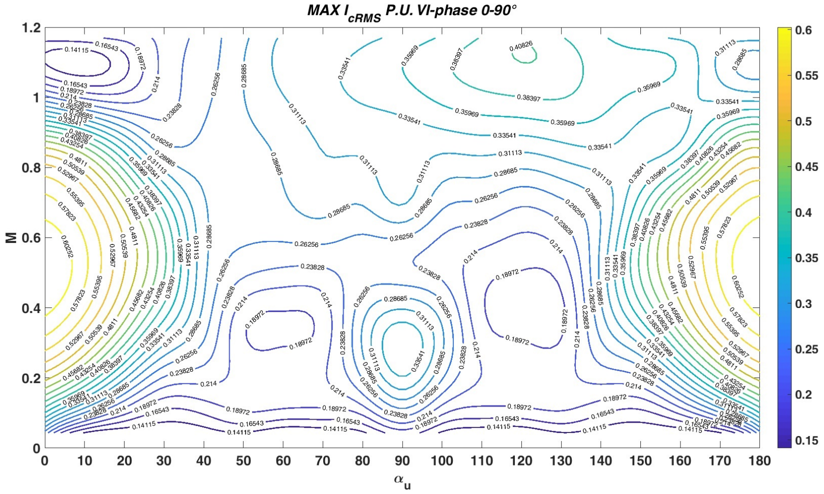

Fig. 4.12 Simulated results: Isolevel of greatest $I_{C_{rms}}$ in p.u respect to the rms value of the phase current worst case vs α_u for all M value. The different figure represent the locus of the greatest $I_{C_{rms}}$ values for a specific operating range.

Modulation in fault condition

As said in Chapter 1 multiphase drives offer additional degree of freedom that can be used for different purposes, such as torque enhancement and design of fault tolerant strategies. The aim of this chapter is to highlight that, in the proposed PWM strategy, adjustments are not needed under fault operation. The displacement between carriers

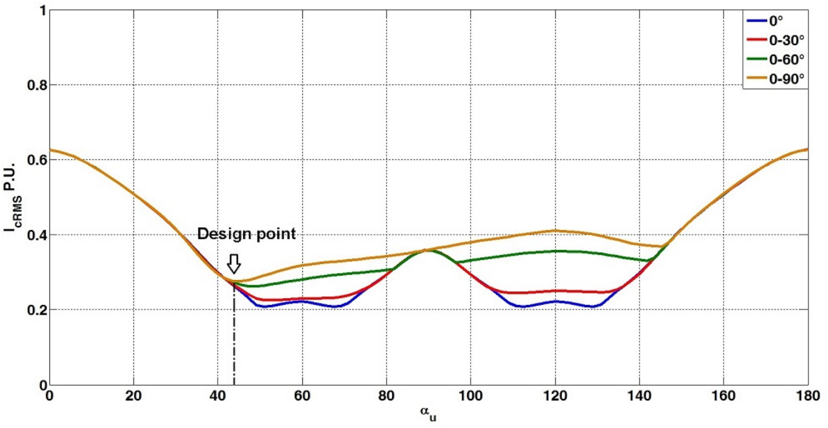

Fig. 4.13 Simulated results: triple-3-phase phase machine: $I_{C_{rms}}$ worst case vs α_u for all M value. The different curves represent the maximum $I_{C_{rms}}$ values for different V-I phases.

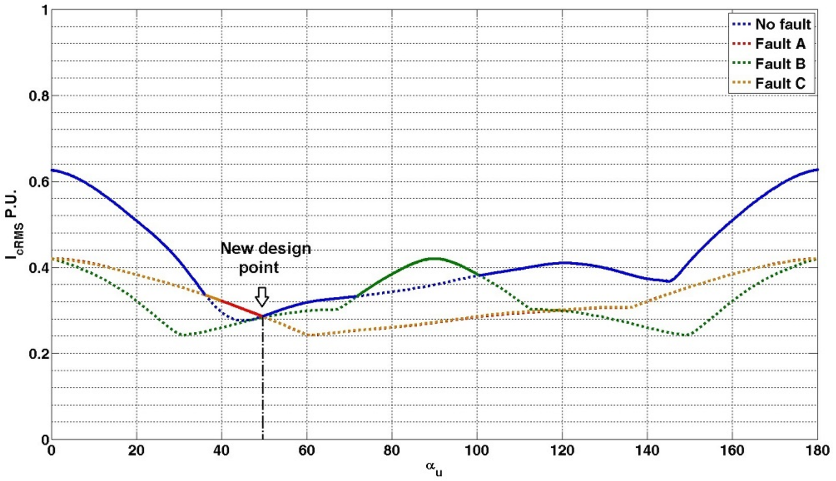

Fig. 4.14 Simulated results: triple-3-phase machine: $I_{C_{rms}}$ worst case vs α_u for all M/VI-phase combinations including in fault conditions.

signals are also applicable under single or double inverter faults appearing as a real additional DoF. The analysis is conduced considering only inverter faults. If one phase of one converter fails the whole converter is removed. Considering the adopted fault scheme, then, the maximum number of admitted inverter faults is 2 (removing 6 inverter legs).

The analysis in previous section is here repeated considering one modular converter fault at a time. The proposed configuration, in fact, is not symmetric and two different faults could occur. For a single inverter fault, then, the value of $I_{C_{rms}}$ depends on which converted has been shut down.

The $I_{C_{rms}}$ values for a double inverter fault are equal to the values for 3-phase case (Fig. 4.7) reduced by a factor of 3, i.e. a constant maximum value of 0.21 p.u. independently of α_u.

Fig. 4.14 shows the locus of the greatest $I_{C_{rms}}$ as a function of α_u for any value of V-I phase and M including fault conditions. The fault of the inverter **a** and **c** leads to the same points and to the same harmonic spectrum, highlighting that the harmonic compensation depend by the mutual phase shift α_u independently by the sign of the shifting. The fault in the **b** inverter leads to the doubling of the adopted phase shifting.
Overlapping the locus of the greatest $I_{C_{rms}}$ for each fault condition it is possible to define a new design point that represents the global best worst case design point for the proposed drive, considering all operating conditions (continuous line in Fig. 4.14). The value of optimal displacement angle α_u on witch the minimum $I_{C_{rms}}$ occurs, also including the fault conditions, is close to the design point that could be defined if no faults would have been introduced.

Harmonics in DC-link

The analysis concludes with the valuation of the capacitor current harmonic contribution for different α_u values. The value of current harmonic contribution depends on M and V-I phase . For each current harmonic contribution the worst cases for all operatives condition are considered. The results for the first 8 harmonics are collected in Fig. 4.15 for the triple-3-phase drive.

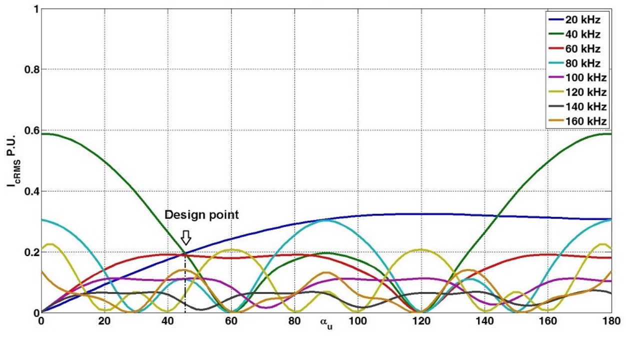

Fig. 4.15 triple-3-phase machine triple 3-phase converter powered: harmonic contribution to the $I_{C_{rms}}$ with α_u

The α_u value that reduces the first harmonic and the second harmonic is near to 45°. This is the angle that reduce the $I_{C_{rms}}$ and that can be considered an optimal solutions also for the implementation view point.

The α_u angles that reduce the single contribution for the triple-3-phase solution are collected in the Table 3.4.

Table 4.1 α_u that minimize the maximum value for each harmonic order for 3-phase machine triple three phase powered

h order	**1**	**2**	**3**	**4**	**5**	**6**	**7**	**8**
α_u	0	60	120	58	71	40	49	60

4.4 Experimental part

Measurements from two different laboratory setups verify the simulated values of the $I_{C_{rms}}$ shown in previous sections. These verifications allow the simulated approach the capability to predict results and to define the appropriate design point. The reduction of the rms current in the capacitor has been tested for three asynchronous motors over a wide variety of operating conditions and then for a triple 3-phase motor. The tests are both essential in order to validate the effectiveness of the simulation methodology.

4.4.1 Three 3-Phase Motors Experimental Setup

The experimental setup adopted in this set of measurements is shown in Figure 4.16. In the following a detailed explanation of the various elements that composed the test bed is given.

Power Electronics

The power electronics used for the test are composed of three inverter boards and a single control unit (Figure 4.16). Each inverter board has a capacitor (260 nF, 600 V) on each leg in order to reduce the commutation path as shown in Figure 4.17 and then to reduce the overvoltage related to the current commutation of each half bridge. The

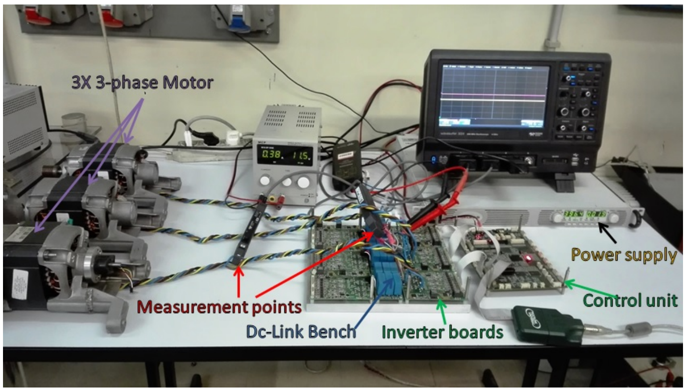

Fig. 4.16 Experimental setup: three 3-phase motors, the control board and the power section with two triple-3-phase converter.

dimension of the ceramic capacitors are one order of magnitude lower with respect to the DC-link one (27 uF); as a consequence, it is possible to consider that the biggest amount of the current ripple flows through the DC-link capacitor. The three boards are connected in a parallel way to a common DC-bus. If the internal DC-bus is not directly accessible, then the values of the $I_{C_{rms}}$ are estimated through the measurement of the AC current downstream the bus (inverters input). The measurement procedure itself affects the results. In fact, the wires introduced to allow for a high bandwidth current probe placing modify the characteristic impedance of the commutation path. The wires and the current probe introduce a parasitic inductance that reduces the amount of current that flows through the DC-link capacitor. In order to complete the analysis, the simulations have been extended including also parasitic parameters, commutation path capacitors and the parameters of the wires introduced for the measurement in Figure 4.18. Taking into account the parasitic parameters in the model is important since they affect the current flowing in the DC-link capacitor showing how the power electronics layout can affect the results. The values reported in Figure 4.18 have been estimated and are considered equal to $Lpar = 1$ nH, $Rm = 5$ mΩ and inductance $Lm = 10$ nH.

Electrical Machines

In order to validate the control technique, three equal induction machines have been adopted (Figure 4.16). This choice has been done in order to verify the validity of the control technique neglecting high frequency phenomena. The results in this case are then compatible with a triple-3-phase machine in which the phases belonging

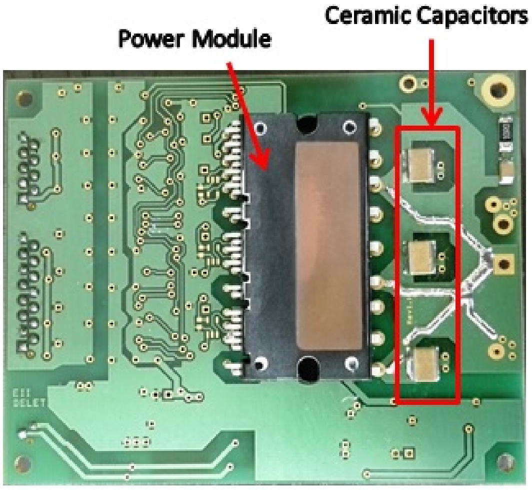

Fig. 4.17 3-phase module: in the picture, the Intelligent Power Module (IPM) and the ceramic capacitors introduced in order to reduce the commutation path are highlighted.

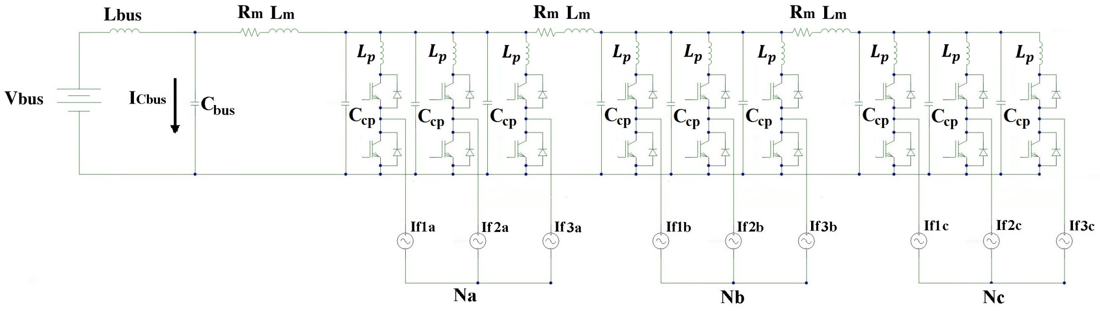

Fig. 4.18 Triple-3-phase converter IGBT based including parassitic inductance $Lpar$, commutation path capacitors Ccp, DC-link connecting cable resistance Rm and inductance Lm.

to different stars are magnetically insulated. The chosen motor design allows for minimizing the mutual coupling between adjacent stars. As a consequence, the interaction between phases belonging to different stars can be neglected in a first approach. The three motors used are motors for home appliance application with the following characteristics (Table 4.2).

The three motors are driven by simple V/Hz control with the three voltage stars displaced one with the other according to Figure 4.2b. No-load and locked rotor tests have also been realized to investigate different value of VI-phase.

Table 4.2 Induction machine data

Characteristics	**Value**
Poles	2
Nominal Current rms	3.2 A
Nominal Voltage rms	190 V
Speed Max	17.900 rpm

Experimental and Simulated Results Comparison

The $I_{C_{rms}}$ in different operating conditions for different values of α_u are depicted in Figure 4.19.

The graphs show different curves:

- the simulated values of $I_{C_{rms}}$ for triple-3-phase converter in (Figure 4.3) (blue line).
- the simulated values of $I_{C_{rms}}$ considering a model of the triple-3-phase converter used in the laboratory setup with estimated concentrated resonance parameters (green line).
- the measured values of $I_{C_{rms}}$ with the laboratory setup (red line).

Similarly to what has been done in Section 4.3.2, it is possible to represent the locus of the greatest $I_{C_{rms}}$ (Figure 4.13) so as to compare for the worst case for the capacitor bench in the simulations and in the experimental results.

Even if the experimental tests $I_{C_{rms}}$ are limited in number and do not cover the whole operating area, the loci of the greatest $I_{C_{rms}}$ for the three different evaluations are compared in Figure 4.20.

Figures 4.19 and 4.20 show that the simulation model well represents the evolution of the phenomena with small differences for high M values. The comparison between the blue curve and the green one highlight that the $I_{C_{rms}}$ values depend by the converter layout. The proposed PWM control technique become more effective if a proper commutation path is adopted, as always happens.

The experimental results provide $I_{C_{rms}}$ trends for α_u close to what was expected. The difference between the green curve and red ones could be due to two factors:

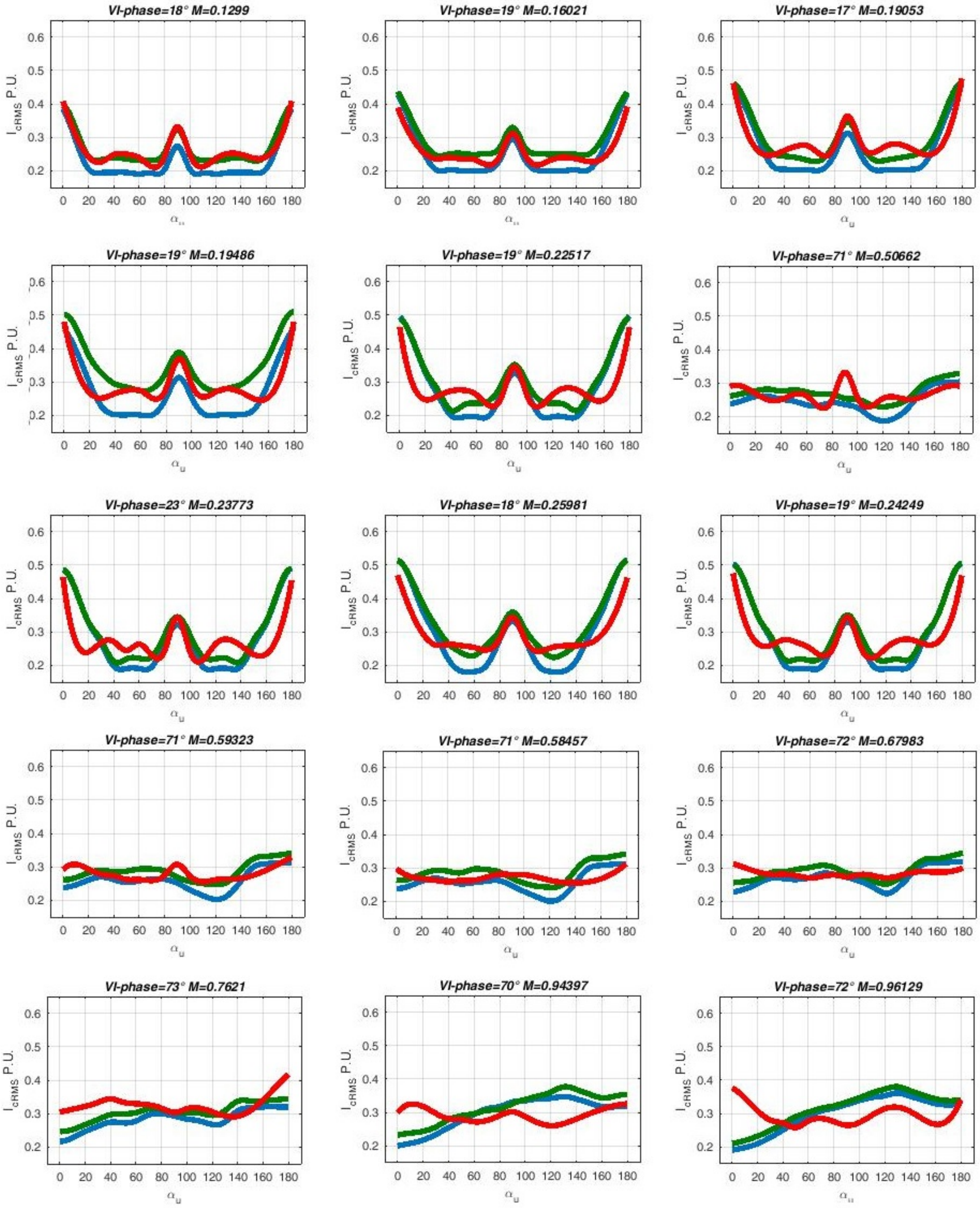

Fig. 4.19 Each picture shows $I_{C_{rms}}$ values for different α_u and different couples of M and VI-phase. The blue line is the simulated $I_{C_{rms}}$ for triple-3-phase converter in Figure 4.3, the green line is the simulated $I_{C_{rms}}$ considering a model of the triple-3-phase converter used in the laboratory setup with estimated concentrated resonance parameters, and the red line is the measured evolution of $I_{C_{rms}}$ with the laboratory setup.

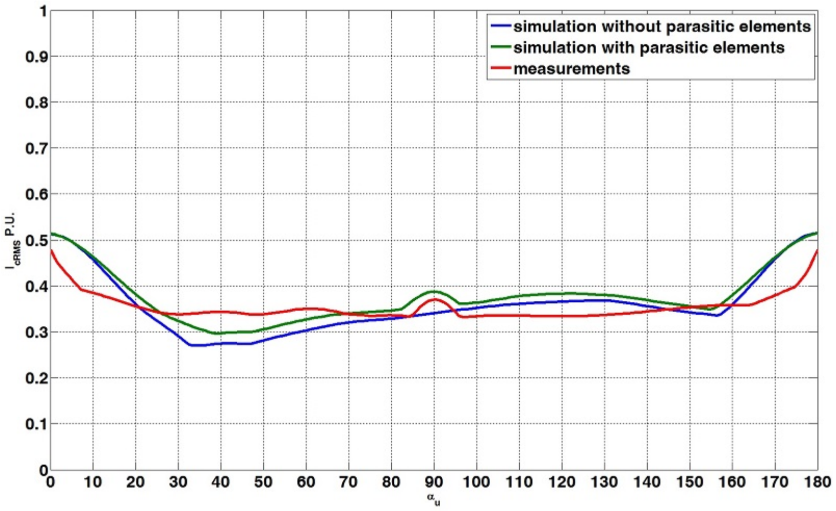

Fig. 4.20 $I_{C_{rms}}$ worst case for α_u variation for considered couples of M and V-I phases values. The blue line is the simulated $I_{C_{rms}}$ for triple-3-phase converter in Figure 4.3, the green line is the simulated $I_{C_{rms}}$ considering a model of the triple-3-phase converter used in the laboratory setup with estimated concentrated resonance parameters, and the red line is the measured evolution of $I_{C_{rms}}$ with the laboratory setup.

- It is difficult to identify the resonant parameters of the commutation path. These parameters are estimated and inserts it in the simulation model as concentrated parameters.

- The DC bus is not directly accessible: as a consequence, the measurements are conditioned by the measurement procedure itself.

Simulation and experimental results, anyway, indicate that the α_u minimizing the $I_{C_{rms}}$ for the proposed PWM strategy is not a constant, and it is not necessarily equal to 120 carrier degrees as could be at first thought. The optimal α_u depends on the converter layout and by operating conditions. Downstream from the simulations and the experimental results, the present work suggests defining the DC-link capacitor bench dimension considering a phase shifting between PWM carriers equal to 45 carrier degrees. In this case, it is possible to contain the value of $I_{C_{rms}}$ in all operating conditions, also considering faults operation. The adoption of this α_u value is advantageous also in terms of implementation being $1/8$ of the PWM period time, typically an integer number in the digital implementations.

4.4.2 Triple 3-Phase Motor Experimental Setup

In Figure 4.21, the test bench is reported. A triple 3-phase machine is driven by a I/Hz control with three equal dq reference current.

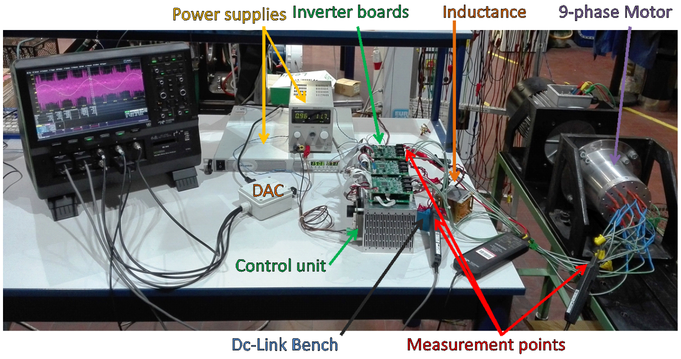

Fig. 4.21 Experimental setup: triple 3-phase motors, the control board and the power section with one triple-3-phase converter.

Power Electronics

The power electronics used for the test is composed by three inverter boards and a single control unit (Figure 4.16). Each inverter board has a capacitor (1.1 uF, 600 V) on each leg in order to reduce the commutation path. An external DC-link film capacitor has been used (60 uF) and the DC-link capacitor is directly accessible. With respect to the previous case, a bigger DC-link inductance is presented (measured $L_m = 220$ nH). Like has been done for the experimental setup previously presented, the estimated parameters shown in Figure 4.18 have been inserted in the simulation. Thanks to the chance to measure directly the DC-link capacitor current, the simulation and the experimental results become much more congruent and the effect of the parasitic element is more evident compared to the previous case.

Electrical Machines

In order to validate the control technique, the has been adopted. The motor used is a different prototype of the triple-3-phase machine presented in Chapter3 in which the array of magnets solution were adopted. This motor has some manufacturing defects and does not present sinusoidal EMF. As a consequence, if a I/Hz control is driven at low speed, the shape of the modulation indexes is not perfectly sinusoidal. In Figure 4.22, the value of a phase current and corresponding modulation index acquired by a Digital to Analog Converter (DAC) have been reported.

Two different operatives' conditions have been tested.

In Figure 4.21, the test bench and the measurement layout have been reported.

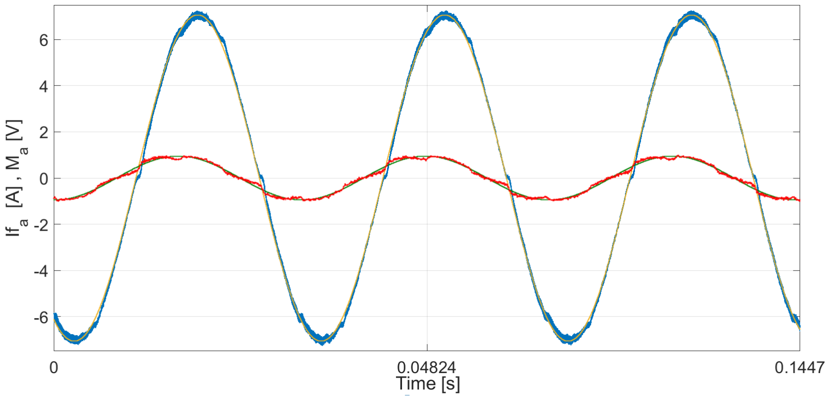

Fig. 4.22 Measurement of the current (blue) and the corresponding modulation index (red) for a single phase. In yellow and green, the corresponding first harmonic of the waves is reported.

Experimental and Simulated Results Comparison

In Figure 4.23, results have been reported in detail for no load and on load conditions. For the same operatives' conditions, the simulations have been conducted without considering the parasitic parameters in order to compare the results with the ideal case. Measurements and simulations highlight how the parasitic parameters can affect the final results.

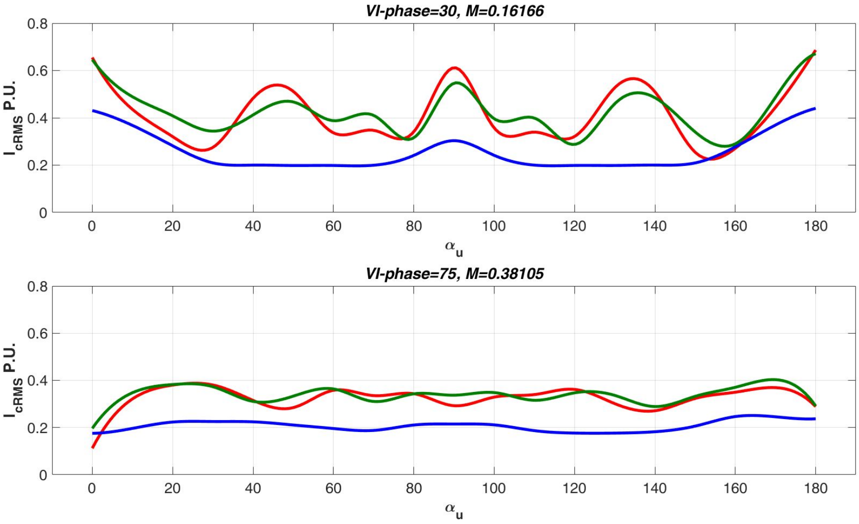

Fig. 4.23 Each picture shows $I_{C_{rms}}$ values for different α_u and different couples of M and VI-phase. The blue line is the simulated $I_{C_{rms}}$ for triple-3-phase converter in Figure 4.3, the green line is the simulated $I_{C_{rms}}$ considering a model of the triple-3-phase converter used in the laboratory setup with estimated concentrated resonance parameters, and the red line is the measured evolution of $I_{C_{rms}}$ with the laboratory setup.

The main differences between the simulation and experimental results are related to:

- the error in the estimation of the resonance parameters of the commutation path,
- the realized modulation index is not purely sinusoidal due to the not perfect sine EMF at load operation

4.5 Sectored 3-phase

With the same stator rotor structure by choosing the correct winding arrangement it is possible to obtain the classical $q_{3/10}$ motor solution. This machine can be powered by a single inverter in a classical way or by a triple-3-phase converter in order to obtain what is here called sectored multiphase drive.

If the 3-phase machine is supplied by a triple three phase converter the per unit phase ripple current is reduced by a factor near to 3. As a first approximation, in fact, same phase voltage means to have 3 times the wires in each coil with an inductance that grows by a factor 9. Phase current is reduced by a factor 3, their ratio presents an advantage of a factor 3 in the per unit phase current ripple (at the same modulation frequency and the same motor voltage).

In this section the analysis previous done has been extended in order to see the possible benefits introduced by the technique of the displacement of the carriers also in these drives.

The 3-phase machine $q_{3/10}$ is supposed powered by a triple-3-phase converter with coils connections as in Fig. 4.24a. It is worth to notice that the currents in the three windings must be the same, and must considers a phase shifting between 3 EMF. This phase shifting is equal to slot electrical displacement. Consequently the voltages applied at the three windings in parallel is such that the currents in the three windings are the same. The center taps N_a, N_b, N_c (Fig. 4.3) are connect together.

In Fig. 4.26b the phasor diagram is reported. In this case the modular structure of the converter is exploited in order to supply each sector of the same phase by a single converter module (each converter module supplies a star of 3-phase). Red stator teeth are supplied by the converter **a**, yellow teeth by the converter **b**; blue teeth by the converter **c**.

The machine control is based on three current controls, with the same reference of current, SPWM based with three different carrier signal.

The simulation setup previously presented has been repeated for this case and the results are collected in Fig. 4.25, Fig. 4.26.

In order to have a global description of the phenomena the results of the DC-link rms current are reported in 4.27 in the form of locus of the greatest.

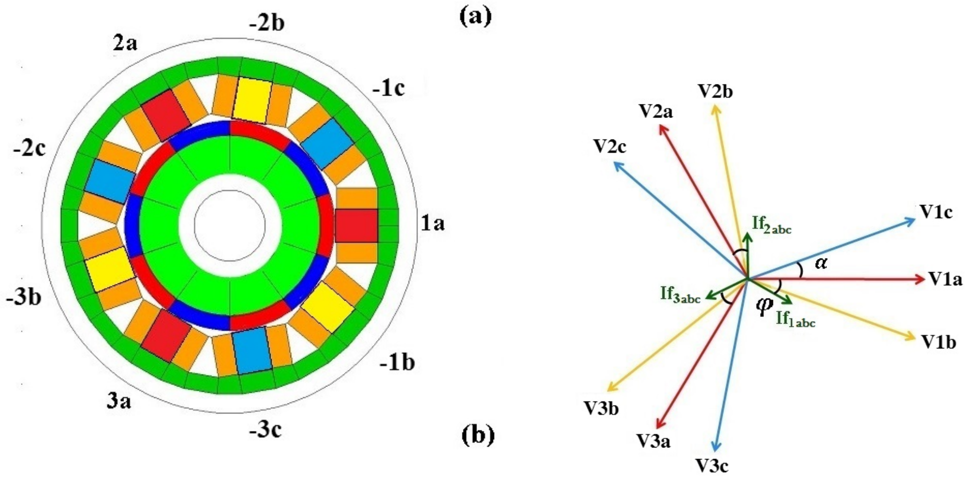

Fig. 4.24 Base machine (**a**) phasor diagrams (**a**) . Red stator teeth are supplied by the converter **a**, yellow teeth by the converter **b**; blue teeth by the converter **c**.

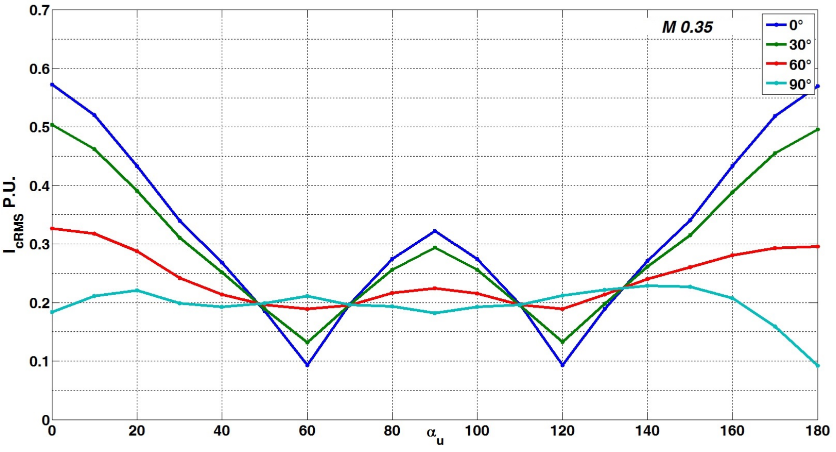

Fig. 4.25 3-phase machine $q_{3/10}$ triple 3-phase powered: $I_{C_{rms}}$ for different displacement between PWM carrier signal(α_u) and different V-I phases. For M=0.35 p.u there is the larger variation of $I_{C_{rms}}$ as function of α_u.

The loci of the greatest can be also been evaluated under single and double inverter faults

It has to be noticed that the $I_{C_{rms}}$ behaviour looks mirrored in the case of the sectored 3-phase drive and triple-3-phase solutions with a small difference in the absolute values. The analyses of the frequency reported in 4.29 gives an explanation at the mirrored behaviour on the $I_{C_{rms}}$ for the triple-3-phase case and sectored 3-phase one that is related in principle to the evolution of the first harmonic (20kHz).

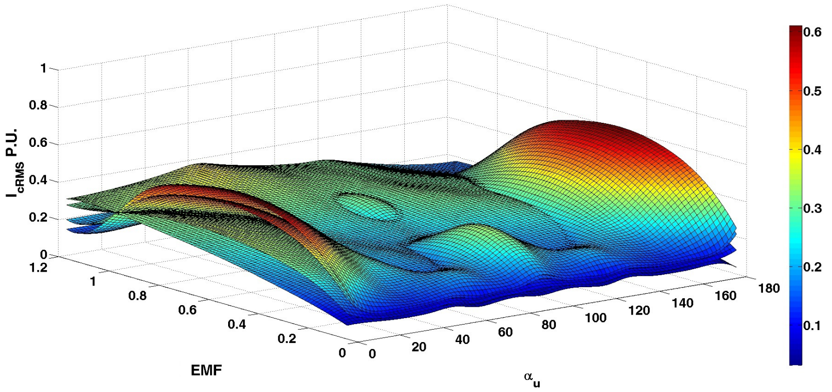

Fig. 4.26 3-phase machine $q_{3/10}$ triple 3-phase powered: values of $I_{C_{rms}}$ with the variation of M and α_u. Any surface represent a different value different values of VI-phases.

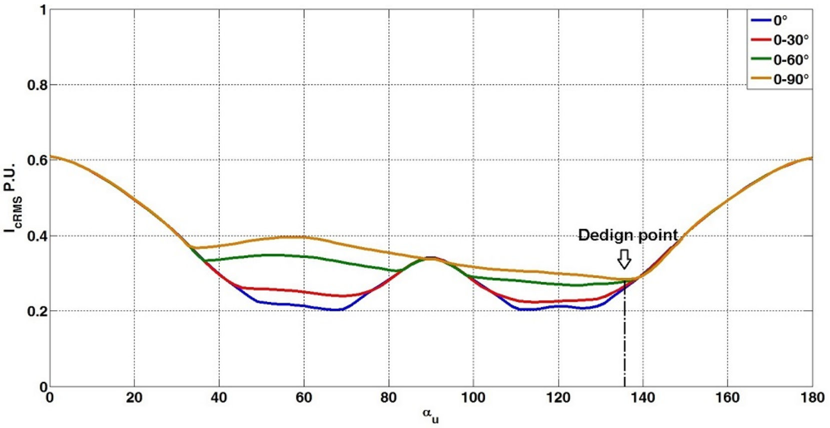

Fig. 4.27 3-phase machine $q_{3/10}$ triple 3-phase powered: worst case for α_u for all M value. The different curves represent the maximum value of $I_{C_{rms}}$ for different V-I phases.

The α_u angles that reduce the single contribution for the 3-phase counterpart are collected in the Tab.4.3

The analyses conducted shown that also using a three phase machine triple three phase powered (sectored multiphase machine) it is possible to obtain interesting benefits from the converter point of view if the PWM carrier displacement is implemented. The results shown that the angle α_u for each the minimum of the greatest occurs is different in this last case. This is not an additional advantage for sectored multi-phase machine as in multiphase one.

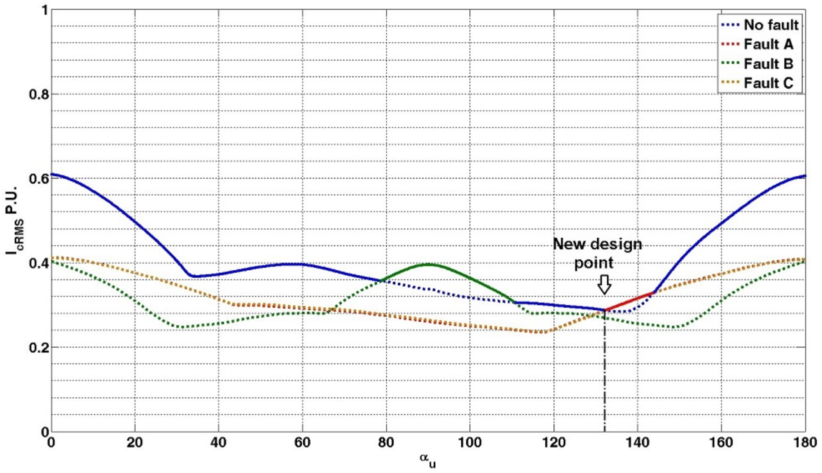

Fig. 4.28 3-phase machine $q_{3/10}$ triple 3-phase converter powered: worst case for α_u variation for all EMF value in fault condition.

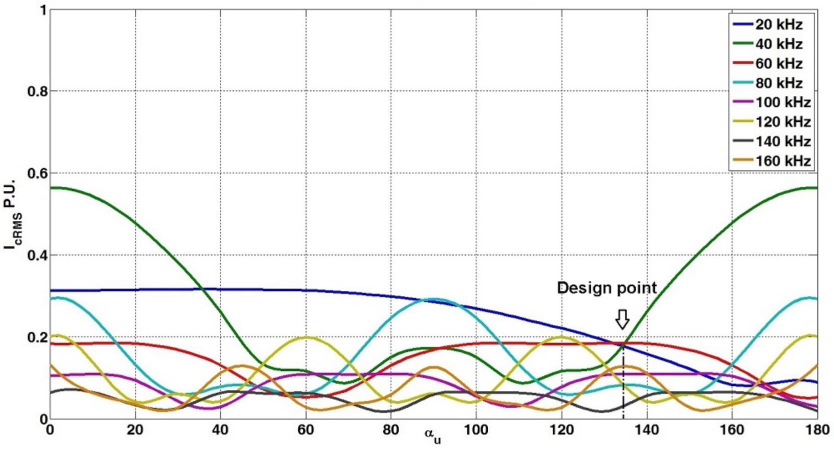

Fig. 4.29 3-phase machine $q_{3/10}$ triple-3-phase converter powered: harmonic contribution to the $I_{C_{rms}}$ with α_u

Table 4.3 α_u that minimize the maximum value for each harmonic order for 3-phase machine triple three phase powered

h order	**1**	**2**	**3**	**4**	**5**	**6**	**7**	**8**
α_u	162	111	60	122	109	142	129	60

4.6 Conclusions

The present section highlights some of the benefits of the multi-n-phase structures and presents a simple modulation strategy that reduces the DC-link stress in terms of rms capacitor current for a triple-3-phase drive. The approach to exploit an additional degree of freedom, the phase shifting between PWM carriers for the different 3-phase inverters, leads to a positive result and allows for the reduction of the DC-link rms current in triple-3-phase drives. The analysis of the benefits introduced by PWM phase shifting are extended to all possible operating conditions including the fault one. The analysis includes the evaluation of harmonic contribution of the capacitor current for different displacement between carrier signal for different operative condition. In order to find the optimal solution to minimize the value of $I_{C_{rms}}$ other condition of PWM phase shifting must be tested especially in the fault conditions. Simulated and experimental results show that the optimal PWM phase shifting is not a constant and the $I_{C_{rms}}$ design point is affected by converters' layout as well as operating conditions.

The same analysis has been extended to sectored multiphase machine and allows to obtain the same benefits. Otherwise sectored multiphase machine not allows to obtain the same benefits in therms of winding factor and reduction of torque ripple. The analysis and the procedure to identify can be extended to other multiphase structure but different results in therms of optimal phase shifting angle occur.

Chapter 5

Torque ripple modelling in fractional slot tooth coil wound Synchronous Reluctance machine

5.1 Introduction

In Chapter 1, the harmonic compensation in the MMF of tooth-coil/multiphase machines has been presented. The advantages that were obtained by the combination of tooth-coil/multiphase solutions can arise interest in reluctance rotor solution, in which the high harmonic content in the MMF has a heavier impact on performances [66, 67]. In this Chapter a mathematical model is proposed in order to evaluate the torque and the torque ripple in fractional slot tooth-coil wound (TCW) Synchronous Reluctance (SyR) machines. Considering a generic harmonic field and an ideal SyR rotor, the rotor magnetic potential and the torque equations are calculated.

The ideal rotor considered is a rotor able to separately react to any harmonic field generated by the stator. In this way the analysis is independent by the specific rotor layout. The ideal synchronous reluctance rotor pole is constituted by an unlimited number of segments separated by an ideal insulator with a constant permeance in each flux barrier. A description about how to design this rotor is reported in Appendix A. The procedure chosen for the calculation of the torque starts from the evaluation of the single pole reaction (in scalar magnetic potential) to a generic stator MMF. This approach allows to analytically justify the pole-per-pole contributions to the torque component in a SyR motor considering a generic stator MMF. As shown by Bianchi et all in [67] by FEA for Fractional Slot Concentrated Windings (FSCW) Permanent Magnet Assisted synchronous Relactance machine (PMAREL) the poles of the machine can contribute to the torque in a non uniform way. The pole-per-pole modelling approach allows to study positive and negative TCW SyR motors. Transversally laminated SyR machines can be divided in two categories [66]:

- positive machines: if the iron is present across the d-axis of the rotor
- negative machines: if air is present across the d-axis of the rotor

Negative rotors are traditionally disregarded due to the poor shaft embedding suitability. Fig.5.1 shown the example of negative rotor reported by Vagati in [68]. Otherwise if the number of poles is greater than 2 some solutions are feasible Fig.5.2. If the number of segments tents toward infinity there is no more difference between positive and negative solutions.

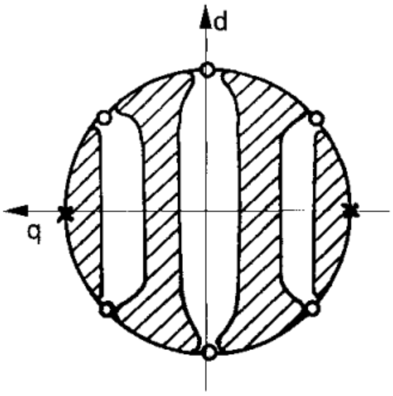

Fig. 5.1 Negative rotor solution: the image is reproduced from A. Vagati, Synchronous reluctance electrical motor having a low torque-ripple design, US5818140A, year 1995 .

The analysis identifies the harmonics that for a generic multiphase TCW machine are potentially involved in the production of torque, by identifying the mechanisms through which they produce torque components.

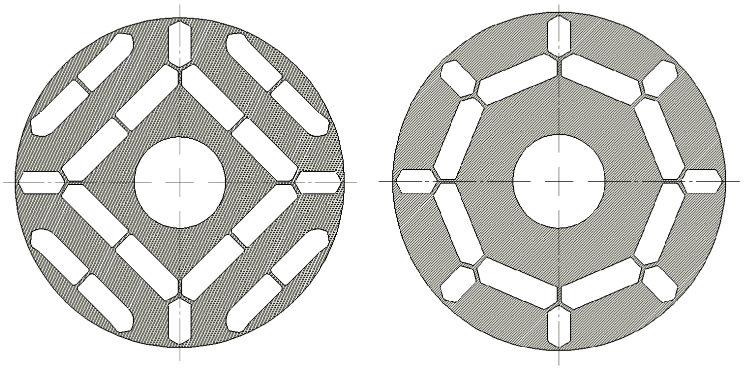

Fig. 5.2 Examples of feasible negatives rotor solutions. On the left p=2 $n_r = 8$ on the right p=8 $n_r = 4$. n_r is defined as the equivalent rotor slot per pole pairs.

5.2 Stator MMF

Based on Chapter 2, the generic harmonic field of a multiphase machine can be expressed by (5.1):

$$f_{s_h} = \hat{f_{s_h}} \cos\left(h\alpha \mp \omega t + \gamma_d\right) \tag{5.1}$$

where $\hat{f_{s_h}}$ is the peak value of the generic harmonic h of the stator MMF, α is the stator coordinate, ω is the electrical pulsation of the current, and γ_d is electrical angle of the current vector with respect the d axis.

The sign $\mp$ in (5.1) depends on the direction of the generic rotating field produced by the stator windings. The sign $(-)$ is related to the direct fields and the sign $(+)$ is related to the reverse fields. The angle γ_i in Fig.5.3 is the angle of the current with axis $\alpha = 0$ and is equal to γ_d for $t = 0$.

In Fig. 5.3 the q axis is considered to be at the center of the generic pole, and a rotor mechanical coordinate ξ, starting from this axis, is assumed to be positive in the counter clockwise direction. The stator coordinate can be written as in (5.2). The generic harmonic field can then be written in the rotor reference frame as in (5.3).

$$\alpha = \omega_r t + \frac{\pi}{2p} + \xi \tag{5.2}$$

$$f_{s_h} = \hat{f_{s_h}} \cos\left(h\xi + h\omega_r t + h\frac{\pi}{2p} \mp \omega t \mp \gamma_d\right) \tag{5.3}$$

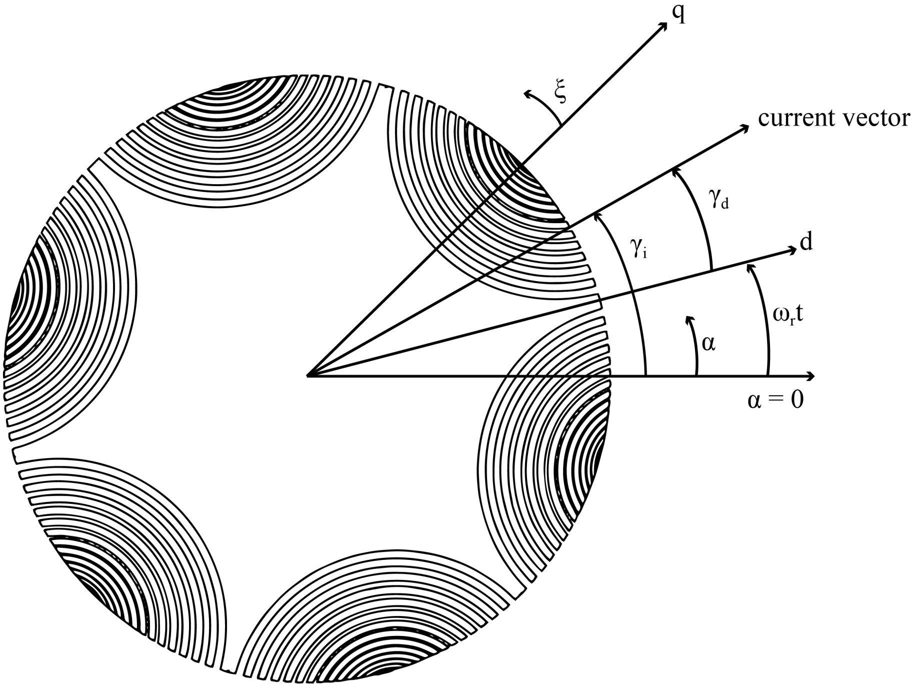

Fig. 5.3 Definition of the reference frame for the a generic ideal rotor $p = 3$.

Where ω_r is the mechanical pulsation and p is the pole pair. Equation (5.3) can be written as a function of the mechanical pulsation being (5.4).

$$\omega = \omega_r sgn\left(\omega_r\right) p \tag{5.4}$$

For compactness, the function $\varphi(t)$ is introduced.

$$\varphi\left(t\right) = -\omega_r t\left(h \mp psgn\left(\omega_r\right)\right) \pm \gamma_d - h\frac{\pi}{2p} \tag{5.5}$$

In conclusion, the generic harmonic of the stator MMF can be expressed in the rotor reference frame as in (5.6) in which φ is the phase angle that contains the time's dependence.

$$f_{s_h} = \hat{f_{s_h}} cos(h\xi - \varphi) \tag{5.6}$$

5.3 Rotor magnetic potential

In this section the magnetic potential of an ideal rotor is calculated. The ideal rotor is a rotor with distributed isotropy in which each flux barrier has a constant permeance. Under this hypothesis the rotor is able to react to each harmonic component of the stator MMF. For an ideal rotor the rotor magnetic potential is only related to the q component of the stator MMF. The *d* and *q* components of (5.6) can be calculated as in (5.7) and (5.8).

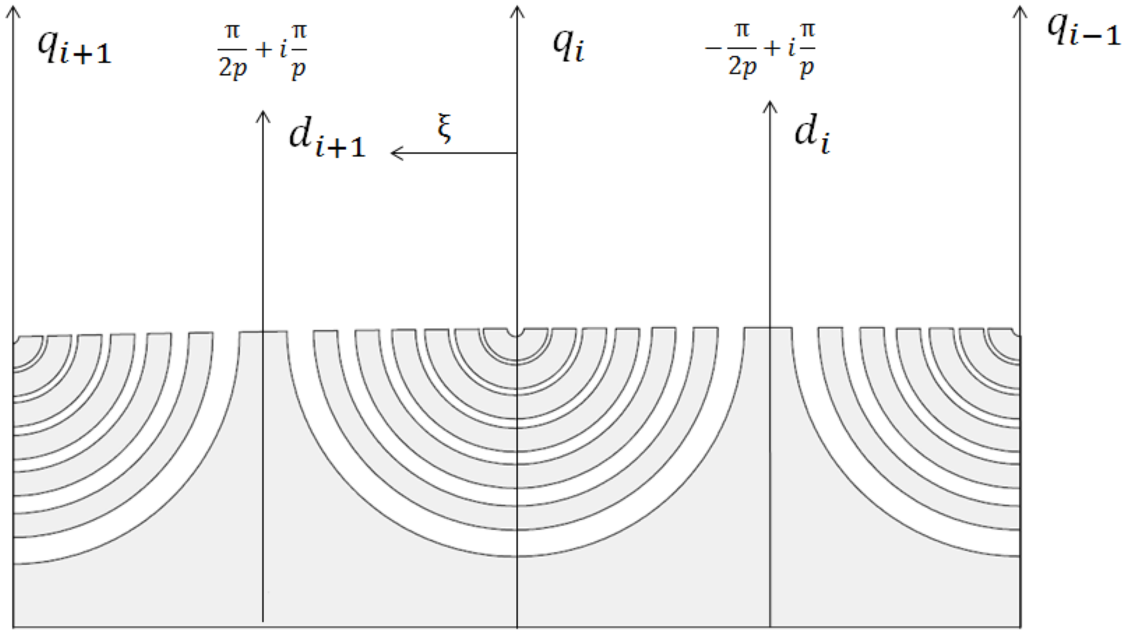

Fig. 5.4 Rotor reference frame. The flux barrier has been designed with constant permeance.

$$2f_{s_{dh}} = f_{s_h}(-\xi) - f_{s_h}(\xi) \tag{5.7}$$

$$2f_{s_{qh}} = f_{s_h}(-\xi) + f_{s_h}(\xi) \tag{5.8}$$

$f_{s_h}(-\xi)$ and $f_{s_h}(\xi)$ are the odd and the even function of the stator MMF respect to the q-axis.

In order to calculate the rotor reaction to a specific harmonic the rotor reference frame is proposed in Fig.5.4. Considering the generic pole *i*, the ideal magnetic potential of the *i* pole is equal to the symmetric component with respect to the generic

q_i reduced by a factor k_h as in (5.9). The pole magnetic potential results in (5.10) that after some manipulation become (5.11). The rotor mechanical coordinate ξ is then defined, starting from the q_0 axis corresponding to the $i = 0$ pole.

$$f_{r_{h,i}} = k_h f_{s_{qh}} \tag{5.9}$$

$$f_{r_{h,i}} = k_h \frac{\hat{f}_{s_h}}{2} \left\{ cos\,(h\xi - \varphi) + cos \left[h \left(-\xi + 2i\frac{\pi}{p} \right) - \varphi \right] \right\} \tag{5.10}$$

$$f_{r_{h,i}} = k_h \hat{f}_{s_h} cos \left(i\frac{h\pi}{p} - \varphi \right) cos \left(h\xi - i\frac{h\pi}{p} \right) \tag{5.11}$$

The coefficient k_h reported in (5.10) is a reduction coefficient that takes into account how the capability of reaction to the harmonics becomes lower as the harmonic order h increases. It depends on the air gap g, the radius at the air gap R, the harmonic order h of the MMF, and the permeance parameter ρ.

$$k_h = \frac{1}{1 + \frac{g}{R}\rho h^2} \tag{5.12}$$

A description about how this parameter has been obtained is reported in Appendix A together with a description of how to obtain a constant permeance rotor.

In 5.11 it is possible to see that the rotor magnetic potential of the single pole depends on the time through φ except for the synchronous harmonic $h = p$. Observing the equation (5.11), it is possible to note that at the generic time t the rotor magnetic potential of two adjacent poles can be different. The rotor reaction calculated for each pole at the border between two adjacent poles can leads to have

- the same scalar magnetic potential
  - equal to zero if h is a multiple odd of p
  - not equal to zero if h is a multiple even of p
- different scalar magnetic potentials if h is not a multiple of p

on the left and on the right of the cross section between two adjacent poles.

This behaviour is shown in Fig.5.5, Fig.5.6, Fig.5.7, Fig.5.8 for a generic 2 pole pair machine in which the harmonics 1,2,4,5 are applied. This harmonics are the ones generated by a classical $q = 1/4$ machine TCW, where q is the number of slot per pole per phase. In these figures are reported the generic MMF harmonic applied (black line), their symmetric component respect to the generic q_i (grey one,) and the corresponding magnetic potential (red line) obtained from equation (5.11) on the mechanical period for $t = 0$ and the generic supply angle $\gamma_d = 55°$. Vertical lines identify the section between poles (d-axes).

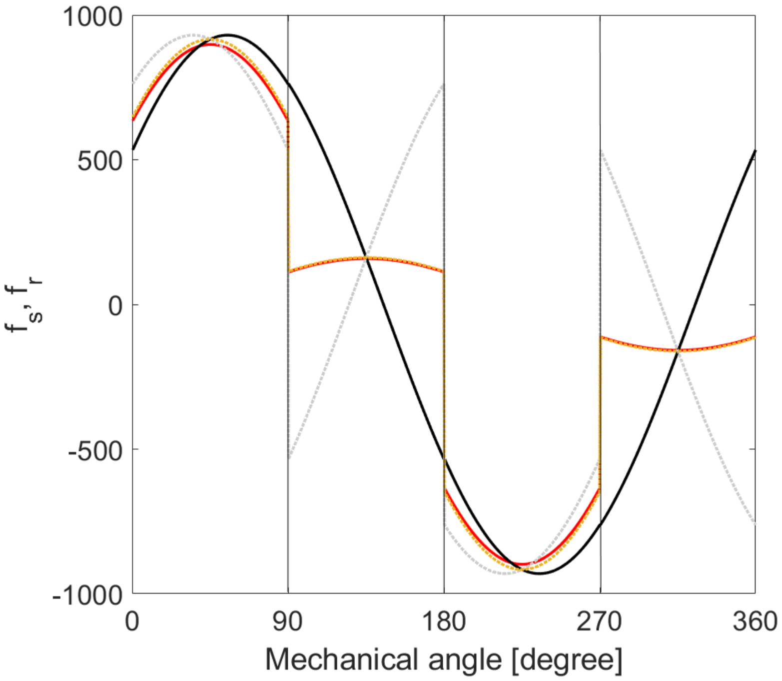

Fig. 5.5 Rotor reaction to the generic harmonic $h = 1$ for $q = 1/4$ and $\gamma_d = 55°$ at $t = 0$ number of turns per coil $Ns = 45$ supply current $25A$.

How these harmonics can affect the torque will be shown in the next section.

5.4 Torque calculation

In the previous section it has been shown how a single pole of an ideal rotor reacts to a specific harmonic of MMF. In this section is calculated the torque produced by the interaction of the stator harmonic of h_w order $f_{s_{h_w}}$ with the rotor reaction $f_{r_{h_v}}$ to

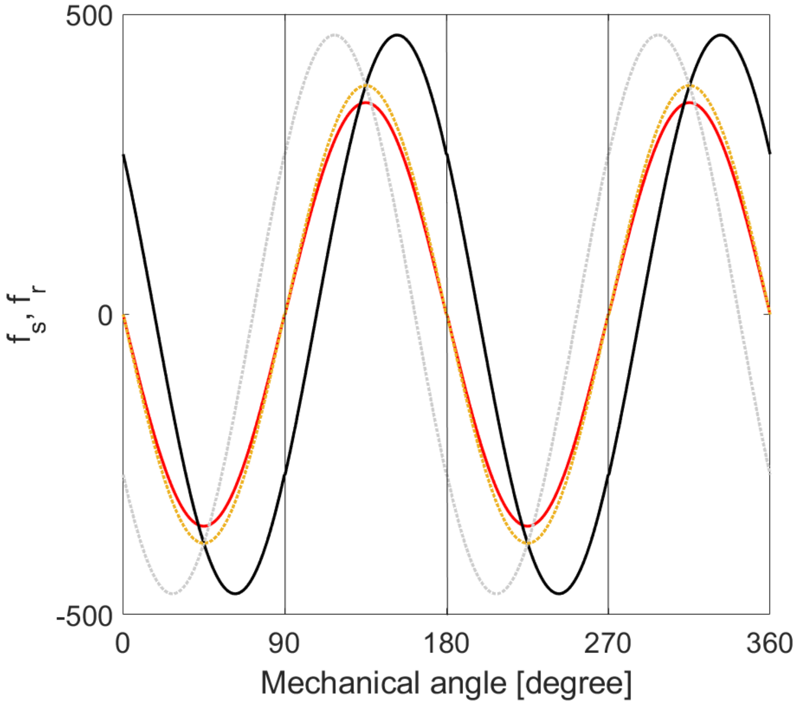

Fig. 5.6 Rotor reaction to the generic harmonic $h = 2$ for $q = 1/4$ and $\gamma_d = 55°$ at $t = 0$.

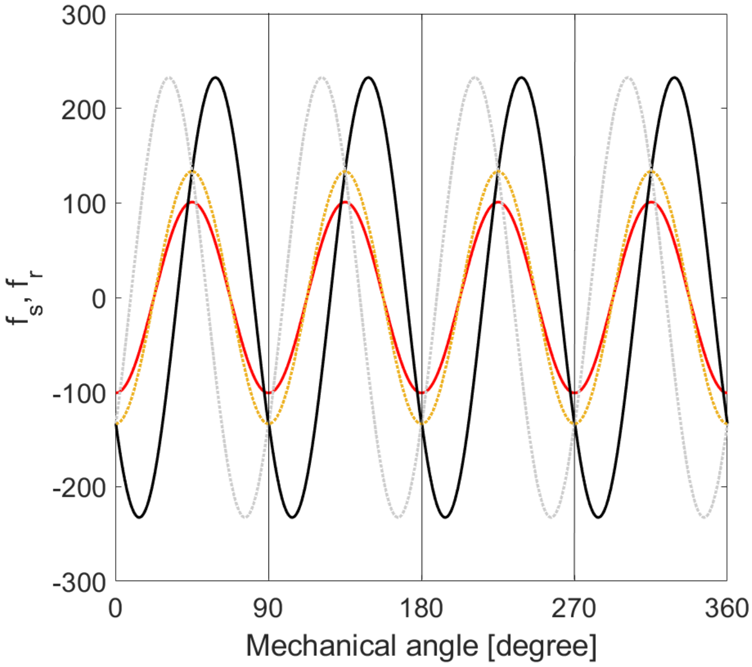

Fig. 5.7 Rotor reaction to the generic harmonic $h = 4$ for $q = 1/4$ and $\gamma_d = 55°$ at $t = 0$, number of turns per coil $Ns = 45$ supply current $25A$.

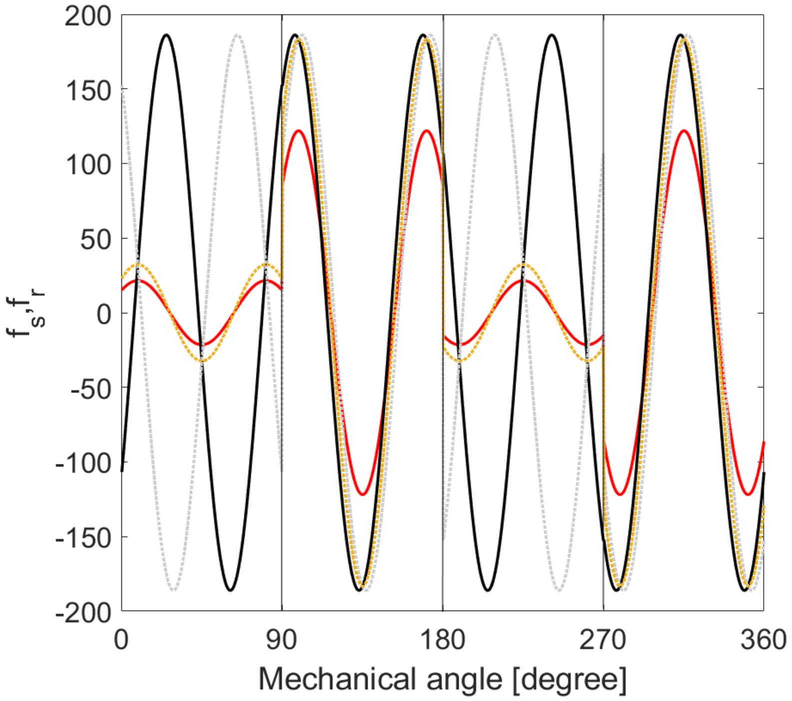

Fig. 5.8 Rotor reaction to the generic harmonic $h = 5$ for $q = 1/4$ and $\gamma_d = 55°$ at $t = 0$, number of turns per coil $Ns = 45$ supply current $25A$.

another stator harmonic $f_{s_{h_v}}$ of h_v order. In order to evaluate the torque, the Lorentz torque law can be written along the rotor periphery as in (5.13).

$$T = r_g l \int_0^{2\pi} B_g df_s = r_g l \frac{\mu_0}{g} \int_0^{2\pi} (f_r - f_s) df_s \tag{5.13}$$

where r_g is the radius at the airgap, B_g is the flux density at the air gap, l is the stack length, μ_0 is the magnetic permeability of the void, f_s is the stator magneto motive force and f_r is the rotor magnetic potential.

$$\int_0^{2\pi} f_s df_s = 0 \tag{5.14}$$

Being (5.14) the torque equation results in (5.15).

$$T = r_g l \frac{\mu_0}{g} \int_0^{2\pi} f_r \frac{df_s}{d\xi} d\xi \tag{5.15}$$

It is worth noting that in the torque calculation the superposition principle has not been applied. Both f_s and f_r can be written as *Fourier* series. However, since the torque calculation process is non-linear, the superposition principle cannot be applied and each stator harmonic could interact with any other rotor harmonic, in general. Instead, the rotor magnetic potential is evaluated harmonic by harmonic and then summed up to get the rotor reaction. This can be done under the hypothesis of linearity of the magnetic circuit. The torque contribution of one stator harmonic can then be calculated as the interaction between the rotor reaction and the single stator harmonic. In addition since in general different poles of the machine can react to specific harmonics in a different way the calculation of the torque is conducted pole-per-pole.

The generic pole i lying between $-\frac{\pi}{2p}+\frac{i\pi}{p}$ and $\frac{\pi}{2p}+\frac{i\pi}{p}$.
For the pole i the torque produced by the interaction between the magnetic potential $f_{r_{i,h_v}}$, due to the application of the stator harmonic h_v, and the generic stator harmonic h_w of the MM $f_{s_{h_w}}$ can be calculated like in (5.16).
It is worth noticing that hv and h_w are considered integers and $h_w > h_v$.

$$T = r_g l \frac{\mu_0}{g} \int_{-\frac{\pi}{2p}+\frac{i\pi}{p}}^{+\frac{\pi}{2p}+\frac{i\pi}{p}} f_{r_{i,h_v}} \frac{df_{s_{h_w}}}{d\xi} d\xi \tag{5.16}$$

The magnetic potential $f_{r_{i,h_v}}$ due to the application of the stator harmonic h_v is reported in (5.17), while the derivative of the stator harmonic MMF is reported in (5.18).

$$f_{r_{h_v,i}} = k_{h_v} \hat{f_{s_{h_v}}} cos\left(i\frac{h_v\pi}{p} - \varphi_v\right) cos\left(h_v\xi - i\frac{h_v\pi}{p}\right) \tag{5.17}$$

$$\frac{df_{s_{h_w}}}{d\xi} = -h_w \hat{f_{s_{h_w}}} sin(h_w\xi - \varphi_w) \tag{5.18}$$

By substitution of 5.17 and 5.18 in 5.16 and after some manipulation the torque per pole results (5.19).

$$\begin{aligned}T_{i,hv,hw} = & -h_w K_{h_v} r_g l \frac{\mu_0}{g} \hat{f}_{s_{h_v}} \hat{f}_{s_{h_w}} \frac{1}{2} \cdot \\ & \left[sin\left((h_w + h_v)\, i\frac{\pi}{p} - \varphi_v - \varphi_w \right) + sin\left((h_w - h_v)\, i\frac{\pi}{p} + \varphi_v - \varphi_w \right) \right] \cdot \\ & \left[\frac{sin\left((h_w + h_v)\, \frac{\pi}{2p} \right)}{h_w + h_v} + \frac{sin\left((h_w - h_v)\, \frac{\pi}{2p} \right)}{h_w - h_v} \right]\end{aligned} \tag{5.19}$$

In order to understand how (5.19) can be simplified, the analysis from here is divided into two sub-cases: one that analyses the case $h_w = h_v$ and one that analyses the case of $h_w \neq h_v$. In the first case we talk about Mirror Torque while in the second case we talk about Mixed Torque.

Mirror Torque

The mirror torque is the torque component related to the interaction between the rotor reaction and the MMF stator harmonic that has generated it.
In the 5.19 $h_w = h_v = h$ has been substituted. Considering (5.20) for ($sinc(0) = 1$), the expression of the torque per pole produced by the generic harmonic h is reported in 5.21 and then in a more compact way in 5.22.

$$\frac{sin\left((h_w - h_v)\, \frac{\pi}{2p} \right)}{h_w - h_v} = \frac{\pi}{2p} sinc\left((h_w - h_v)\, \frac{\pi}{2p} \right) \tag{5.20}$$

$$T_{i,h} = -hK_h r_g l \frac{\mu_0}{g} (\hat{f}_{s_h})^2 \frac{1}{2} \cdot \left[sin\left(2hi\frac{\pi}{p} - 2\varphi \right) \right] \cdot \left[\frac{sin\left(h\frac{\pi}{p} \right)}{2h} + \frac{\pi}{2p} \right] \tag{5.21}$$

$$T_{i,hv,hv} = -K_h r_g l \frac{\mu_0}{g} (\hat{f}_{s_h})^2 \frac{1}{4} \cdot \left[sin\left(2hi\frac{\pi}{p} - 2\varphi \right) \right] \cdot \left[sin\left(h\frac{\pi}{p} \right) + h\frac{\pi}{p} \right] \tag{5.22}$$

Summing up the torque contribution for each pole for variation of $i = 0$ to $2p-1$, the torque produced by the generic harmonic h results. In some cases a zero sum results.
In details, only for the harmonic h multiple (odd or even) of pole pairs p the torque contributions of each pole are in phase and sum each other. Otherwise the torque contributions constituted a regular star at zero sum. This in particular results by the observation of the first square bracket in (5.22).
If the harmonic applied ($h_v = h_w = h$) is an integer multiple of p the torque component on the whole rotor results in (5.23).

$$\begin{aligned} T_h = \sum_{i=0}^{2p-1} T_{i,h} &= 2pK_h h r_g l \frac{\mu_0}{g} (\hat{f_{s_h}})^2 \frac{1}{2} sin\left(2\varphi\right) \frac{\pi}{2p} \\ &= K_h h r_g l \pi \frac{\mu_0}{2g} (\hat{f_{s_h}})^2 \cdot sin 2\varphi \end{aligned} \tag{5.23}$$

Equation (5.23) for $h = p$ results in the synchronous torque (5.24) that present maximum value for $\gamma_d = 45^\circ$. All the other harmonics multiple of pole pairs give torque ripple. The harmonic order of this torque ripple is defined by φ.

$$T_{h=p} = -K_h p r_g l \pi \frac{\mu_0}{2g} (\hat{f_{s_h}})^2 \cdot sin 2\gamma_d \tag{5.24}$$

The total torque of this kind is then obtained from (5.23), by summing up from 1 to infinity the index (h/p) as in (5.25).

$$T_{mirror} = \sum_{\frac{h}{p}=1}^{\infty} K_h h r_g l \pi \frac{\mu_0}{2g} (\hat{f_{s_h}})^2 \cdot sin 2\varphi \tag{5.25}$$

The analysis conducted up to here highlights the fact that, even if an harmonic is present in the stator MMF and if it is able to generate a rotor magnetic potential, it doesn't means that it is able to generate a torque component on the whole rotor. This is for example the case of the harmonic $h = 1$ in a $p = 2$ rotor. This sub harmonics can polarize the rotor poles but each pole contributes to the torque in a different way, and results in a zero sum. It is worth noticing that the harmonics not multiple of pole pairs can not be discarded from the analysis of the torque, as it is done for example for the SMPM solution. This concept will be clarified in the next section.

Mixed Torque

In FSCW, the harmonic content of the MMF is very rich. We have seen that the harmonics multiple of p polarize the rotor poles in a symmetrical way and can generate torque components. Instead, the harmonics that are not multiples of p can polarize each pole of the rotor in a different way, but they are not able to produce mirror torque components. In this section, it will be shown that also the harmonics which are not multiple of p have the potential to produce torque ripple.
In particular, it will be demonstrated that some pairs of harmonics of different order (h_v and h_w), if they are present simultaneously, can interact to generate torque components. We call these torque components Mixed Torque.
The simultaneous presence of two harmonics h_v and h_w is then considered in the torque calculation. The torque produced by the interaction between the rotor magnetic potential, due to the harmonic h_v, and the stator harmonic h_w is reported in (5.26).

$$
\begin{aligned}
T_{i,hv,hw} = & -h_w K_{h_v} r_g l \frac{\mu_0}{g} \hat{f_{s_{h_v}}} \hat{f_{s_{h_w}}} \frac{1}{2} \cdot \\
& \left[sin\left((h_w + h_v)\, i\frac{\pi}{p} - \varphi_v - \varphi_w \right) + sin\left((h_w - h_v)\, i\frac{\pi}{p} + \varphi_v - \varphi_w \right) \right] \cdot \\
& \left[\frac{sin\left((h_w + h_v)\, \frac{\pi}{2p} \right)}{h_w + h_v} + \frac{sin\left((h_w - h_v)\, \frac{\pi}{2p} \right)}{h_w - h_v} \right]
\end{aligned}
\tag{5.26}
$$

In the same way, the torque produced by the interaction between the rotor magnetic potential due to the harmonic h_w, and the stator harmonic h_v is reported in (5.27)

$$\begin{aligned} T_{i,hw,hv} = & -h_v K_{h_w} r_g l \frac{\mu_0}{g} \hat{f}_{s_{h_w}} \hat{f}_{s_{h_v}} \frac{1}{2} \cdot \\ & \left[sin\left(\left(h_w + h_v \right) i \frac{\pi}{p} - \varphi_w - \varphi_v \right) - sin\left(\left(h_w - h_v \right) i \frac{\pi}{p} + \varphi_v - \varphi_w \right) \right] \cdot \\ & \left[\frac{sin\left(\left(h_w + h_v \right) \frac{\pi}{2p} \right)}{h_w + h_v} + \frac{sin\left(\left(h_w - h_v \right) \frac{\pi}{2p} \right)}{h_w - h_v} \right] \end{aligned} \tag{5.27}$$

Being h_v and h_w of the stator MMF present simultaneously the torque contribution of each pole is equal to 5.28.

$$\begin{aligned} & T_{i,hw,hv} = -r_g l \frac{\mu_0}{g} \hat{f}_{s_{h_w}} \hat{f}_{s_{h_v}} \frac{1}{2} \cdot \\ & \left[\left(h_w K_{h_v} + h_v K_{h_w} \right) sin\left(\left(h_w + h_v \right) i \frac{\pi}{p} - \varphi_w - \varphi_v \right) + \left(h_w K_{h_v} - h_v K_{h_w} \right) sin\left(\left(h_w - h_v \right) i \frac{\pi}{p} + \varphi_v - \varphi_w \right) \right] \cdot \\ & \left[\frac{sin\left(\left(h_w + h_v \right) \frac{\pi}{2p} \right)}{h_w + h_v} + \frac{sin\left(\left(h_w - h_v \right) \frac{\pi}{2p} \right)}{h_w - h_v} \right] \end{aligned} \tag{5.28}$$

Summing up the contributions of the poles, some of them result in a zero sum. In fact, by the observation of the first bracket of the formula (5.28):

- when $h_w + h_v$ is an even multiple of p, the $sin\left(\left(h_w + h_v \right) i \frac{\pi}{p} - \varphi_w - \varphi_v \right)$ results in a non zero sum
- when $h_w - h_v$ is an even multiple of p, the $sin\left(\left(h_w - h_v \right) i \frac{\pi}{p} + \varphi_v - \varphi_w \right)$ results in a non zero sum

Instead to the observation of the second bracket of the formula:

- when $h_w + h_v$ is an even multiple of p the term $sin\left(\left(h_w + h_v \right) \frac{\pi}{2p} \right)$ is zero
- when $h_w - h_v$ is an even multiple of p the term $sin\left(\left(h_w - h_v \right) \frac{\pi}{2p} \right)$ is zero

As a consequence the harmonics h_v and h_w must respect the conditions in 5.29 in order to contribute to the torque:

$$\begin{cases} h_w + h_v = mp \\ h_w - h_v = np \end{cases} \tag{5.29}$$

with m integer even and n integer odd or alternative m integer odd and n integer even. Equation (5.29) say that only the pair of harmonics for which their sum is an even multiple of p and their difference is an odd number of p (or vice versa) can interact to give a torque component. As a consequence, the harmonics that are object of interest according to the 5.28, are those ones for which 5.30 is valid.

$$\begin{cases} h_w = \frac{m+n}{2} p \\ h_v = \frac{m-n}{2} p \end{cases} \tag{5.30}$$

Being m even and n odd or vice versa, also the sum and the difference of m and n results in a odd number. In order to have h as an integer the number of p must be even. This means that only for the machines characterized by an even number of p must be taken into account the contribution of the mixed torque.
Being the sum and the differences of m and n an odd number, only the harmonics that are odd multiple of $p/2$ can interact between each other in order to produce torque.
It is worth noticing that the case $h_w = hv$ occurs for $n = 0$. In order to obtain 5.22 from 5.28 it is needed to substitute $h_w = h_v$ and to divide the results by 2 since in (5.28) the two dual torque terms are present.

For a SyR machine with p being odd, only the harmonics multiple of pole pair can contribute to the torque and then only "mirror torque" formulation must be considered. In the case of p being even the cross effect of non-multiple harmonics of the pole pair must be taken into account through the mixed torque formulation.

Two expressions of the torque can be written. One that considers m even and the other one that considers m odd.

$$T_{meven} = +pr_g l \frac{\mu_0}{g} \hat{f}_{s_{h_w}} \hat{f}_{s_{h_v}} \cdot \left(h_w K_{h_v} + h_v K_{h_w} \right) sin \left(\varphi_w + \varphi_v \right) \cdot \left[\frac{sin\left(\left(h_w - h_v \right) \frac{\pi}{2p} \right)}{h_w - h_v} \right] \tag{5.31}$$

$$T_{modd} = +pr_g l \frac{\mu_0}{g} \hat{f}_{s_{h_w}} \hat{f}_{s_{h_v}} \cdot \left(h_w K_{h_v} - h_v K_{h_w} \right) sin \left(\varphi_w - \varphi_v \right) \cdot \left[\frac{sin\left(\left(h_w + h_v \right) \frac{\pi}{2p} \right)}{h_w + h_v} \right] \tag{5.32}$$

In (5.31) and (5.32) the parameters φ_v and φ_w contain the dependence of the phase angle (γ_d). It is worth noticing that the sum and the difference of φ_v and φ_w can leads to torque components that are dependent on the phase angle or to torque components that are independent by the phase angle.

According to(5.30) it is possible to realize a matrix like the one in Fig. 5.9, in which the allowed m,n pairs identifies uniquely the pairs of harmonics that if present can give a mixed torque component. The not allowed situations (the sum and the difference between n and m are both even or both odd) are evidenced by a small cross.

n m	1	2	3	4	5	6	7	8	9	10	11	12	13	14	15
1	■		X		X		X		X		X		X		X
2	--	■		X		X		X		X		X		X	
3	--	--	■		X		X		X		X		X		X
4	--	--	--	■		X		X		X		X		X	
5	--	--	--	--	■		X		X		X		X		X
6	--	--	--	--	--	■		X		X		X		X	
7	--	--	--	--	--	--	■		X		X		X		X
8	--	--	--	--	--	--	--	■		X		X		X	
9	--	--	--	--	--	--	--	--	■		X		X		X
10	--	--	--	--	--	--	--	--	--	■		X		X	
11	--	--	--	--	--	--	--	--	--	--	■		X		X
12	--	--	--	--	--	--	--	--	--	--	--	■		X	
13	--	--	--	--	--	--	--	--	--	--	--	--	■		X
14	--	--	--	--	--	--	--	--	--	--	--	--	--	■	
15	--	--	--	--	--	--	--	--	--	--	--	--	--	--	■

Fig. 5.9 m,n points allowed .

In a 3-phase motor for example the table can be built excluding also the case in which the the sum or the difference of m and n gives an harmonic multiple of 3. The void space in the table identifies the pairs of harmonics that, if present in the stator MMF, are able to produce torque components. It is worth noticing that the elements in the row characterized by $n = 2$ give independent of time contributes to the torque. In all other cases they constitute vertices of a square characterized by a specific ripple harmonic (Fig. 5.10). For example in a 3-phase 4 poles machine the pairs of harmonics $(7,5),(7,1),(11,5),(11,1)$ if present can contribute to the torque with a sixth harmonic, the harmonics $(13,11),(13,7),(17,11),(17,7)$, if present, can contribute to the torque with a 12 harmonics and so on. For the red dots (5.31) must to be used while for the purple dots (5.32) must be used. The line n=2 is related to the continuous components of mixed torque for which (5.32) must be used. All this harmonic are present in the $q = 1/4$ solution. The model is valid for any multiphase machine. For example, considering a 5-phase 4 poles machine (as the $5-1-4-1$ solution is) the pairs of harmonics $(13,3),(13,7)(17,3),(17,7)$ contribute to the torque with a tenth harmonic, while the harmonics $(23,7),(27,7),(23,13),(27,13)$ contribute to the torque with a fifteenth harmonic. Also in this case the line n=2 is related to the continuous components of mixed torque for which (5.32) must be used. Fig. 5.11 shows the squares related to the 5-phase 4 poles machine.

The total torque due to interaction of harmonics of different order is obtained from (5.31) and (5.32) , by summing up to infinity all the allowed m values, while n is summed up to $m-1$ only as in (5.33).

$$T_{mixed} = \sum_{m=1}^{\infty} \sum_{n=1}^{m-1} T_{m,n} \tag{5.33}$$

where $T_{m,n}$ is equal to (5.31) if m is even and is equal to (5.32) when m is odd.

5.5 Validation

In order to validate the model, FEA have been conducted. The motor chosen is a 4 poles rotor. For the motor characterized by p even, also the harmonics not multiple of pole pairs can contribute to the torque. In this section the main characteristic of

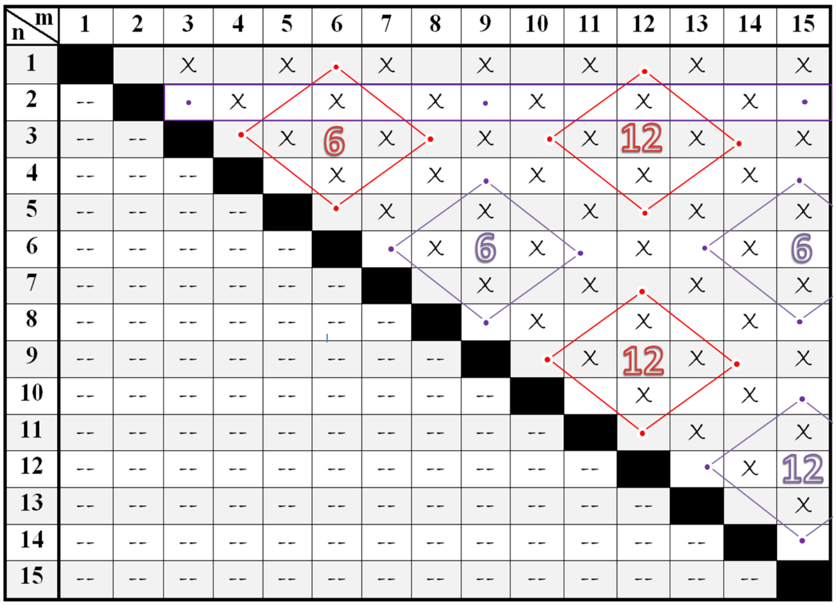

n \ m	1	2	3	4	5	6	7	8	9	10	11	12	13	14	15
1	■		X		X		X		X		X		X		X
2	--	■	•	X		X		X	•	X		X		X	•
3	--	--	■		X	6	X		X		X	12	X		X
4	--	--	--	■		X		X		X		X		X	
5	--	--	--	--	■		X		X		X		X		X
6	--	--	--	--	--	■		X	6	X		X		X	6
7	--	--	--	--	--	--	■		X		X		X		X
8	--	--	--	--	--	--	--	■		X		X		X	
9	--	--	--	--	--	--	--	--	■		X	12	X		X
10	--	--	--	--	--	--	--	--	--	■		X		X	
11	--	--	--	--	--	--	--	--	--	--	■		X		X
12	--	--	--	--	--	--	--	--	--	--	--	■		X	12
13	--	--	--	--	--	--	--	--	--	--	--	--	■		X
14	--	--	--	--	--	--	--	--	--	--	--	--	--	■	
15	--	--	--	--	--	--	--	--	--	--	--	--	--	--	■

Fig. 5.10 m,n point allowed and vertex of the squares that contribute to a specific harmonic order for a 3-phase 4 poles machine. In red the vertex related to m even, in purple related to m odd.

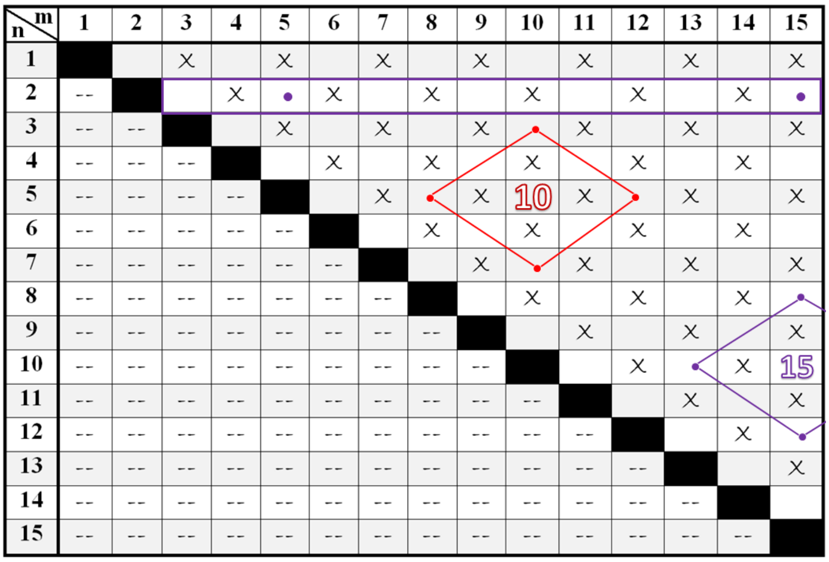

n \ m	1	2	3	4	5	6	7	8	9	10	11	12	13	14	15
1	■		X		X		X		X		X		X		X
2	--	■		X	•	X		X		X		X		X	•
3	--	--	■		X		X		X		X		X		X
4	--	--	--	■		X		X		X		X		X	
5	--	--	--	--	■		X		X	10	X		X		X
6	--	--	--	--	--	■		X		X		X		X	
7	--	--	--	--	--	--	■		X		X		X		X
8	--	--	--	--	--	--	--	■		X		X		X	
9	--	--	--	--	--	--	--	--	■		X		X		X
10	--	--	--	--	--	--	--	--	--	■		X		X	15
11	--	--	--	--	--	--	--	--	--	--	■		X		X
12	--	--	--	--	--	--	--	--	--	--	--	■		X	
13	--	--	--	--	--	--	--	--	--	--	--	--	■		X
14	--	--	--	--	--	--	--	--	--	--	--	--	--	■	
15	--	--	--	--	--	--	--	--	--	--	--	--	--	--	■

Fig. 5.11 m,n point allowed and vertex of the squares that contribute to a specific harmonic order for a 5-phase 4 poles machine. In red the vertex related to m even, in purple related to m odd.

the stator and the rotor used for validation are reported and the simulation results are collected.

The rotor

The rotor must be as close as possible to the ideal one. The main limitation is imposed by the impossibility to simulate a very large number of segments due to the limit imposed by the solver. The machine has been designed in an automatic way using the formulas reported in appendix A. In order to realize a constant permeance rotor the percentage of air in each segment must be reduced going from the d-axis to the q-axis. If the width of segments is constant this will lead to have a thickness that increases going from the d to the q-axis. In order to design a reasonable solution from the flux distribution point of view it is possible to follow an iterative procedure in which the thickness of the sections is reduced going from the d to the q-axis. In this way, it is possible obtain a reduction in the air ratio $a(\xi')$ as in the left picture of Fig. 5.12 with a reduction of the segment thickness as in the right picture of Fig. 5.12.

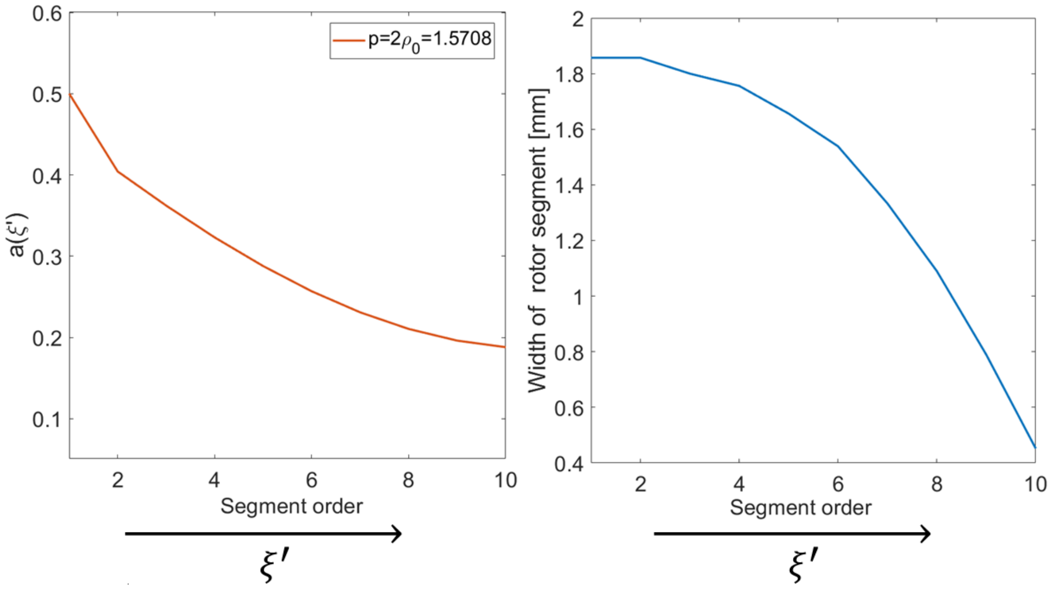

Fig. 5.12 $a(\xi')$ ratio and the thickness function implemented in order to obtain a reduction in the iron from d to q axis.

Fig.5.13 shown the resulting rotor pole designed according to Appendix A, in which it has been implemented the segment thickness function in the right picture of Fig. 5.12 and the air ratio $a(\xi')$ is reduced as in left picture of Fig.5.12.

In order to conduct a simulation closer to the ideal case, the iron used is linear and with the maximum permeability admitted by the solver. Between two adjacent

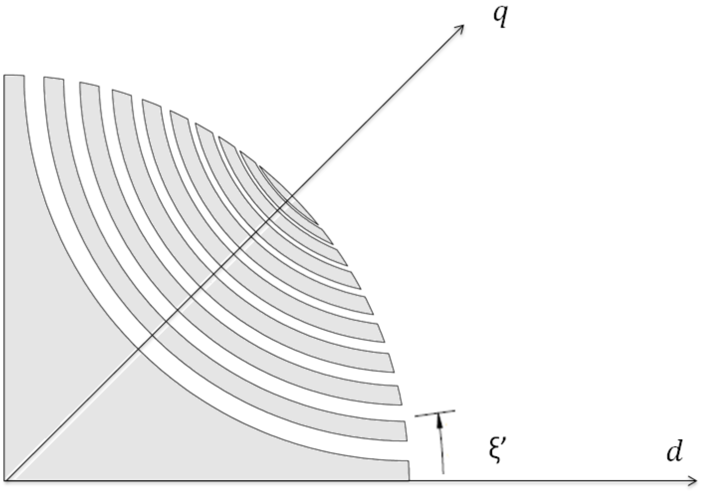

Fig. 5.13 Ideal rotor pole $p = 2$.

poles a small width of air has been positioned and a boundary condition between the poles has been put. The previous assumptions can also be removed in order to approach the real case.

The stator

In order to verify the analysis a special stator must be designed. Since in the model no stator slots have been taken into account, a real stator structure can not be used in the simulations. What we want to realize is a stator structure that allows to generate the same rotating magnetic field at the air gap of a real stator without introducing phenomena related to the slots. In addition, it is better to realize a system that allows to apply the stator harmonics once at time (or a pair of harmonics) in order to see how the rotor reacts to each of them. This can be done using a stator ring in which on the surface is applied a linear current density that reproduces the effect of stator MMF harmonics. This method was used by Tessarolo et al in [69–72] in order to evaluate the rotor eddy current losses in PM machines.

The software used for the FEA validation is the Finite Element Method Magnetics (FEMM 4.2). In this environment it is possible to realize a linear current density by the use of points in which the current can be applied. The stator can be modelled by an iron ring with n_d point (dot) equally distributed on air gap surface. According to [72] the current ΔI_d that must be applied to each point identified by d (can vary from 1 to n_d) is equal to 5.34.

$$\Delta I_d\left(t\right) = r_g \Delta\alpha_d J\left(d\Delta\alpha_d, t\right) \tag{5.34}$$

where $\Delta\alpha_d = \frac{2\pi}{n_d}$ identifies the distance between two points and the α_d is the mechanical angle of the generic point d. The current density is related to the stator MMF by the equation 5.35 (that discend by the Ampere's circuital law).

$$J\left(\alpha, t\right) = \frac{1}{r_g}\frac{\partial f_{s_h}\left(\alpha, t\right)}{\partial\alpha} \tag{5.35}$$

The generic harmonic h of the MMF in the stator reference frame is equal to 5.36 , where $\mp$ identify if the harmonic is associated to a direct or reverse rotating field. Then the density current that has to be considered in the simulation is 5.37.

$$f_{s_h} = \hat{f}_{s_h} cos\left(h\alpha \mp \omega t \mp \gamma_d\right) \tag{5.36}$$

$$J_h\left(\alpha, t\right) = -h\hat{f}_{s_h} sin\left(h\alpha \mp \omega t \mp \gamma_d\right) \tag{5.37}$$

The harmonics that must be applied are the harmonics of the stator MMF (the harmonic of the rotating magnetic field) of the real stator that we want to emulate.

The ideal stator, coupled with an isotropic rotor is reported in Fig.5.14. In the picture the harmonic applied by (5.37) is the $4th$ with a phase angle of $\gamma_d = 45°$.

Results

In a 4 poles machine the harmonics that if present on the stator MMF can contribute to the torque are:

- the harmonics multiple of p (2,4,6,8...)
- the harmonics that result from the table m,n in Fig.5.10

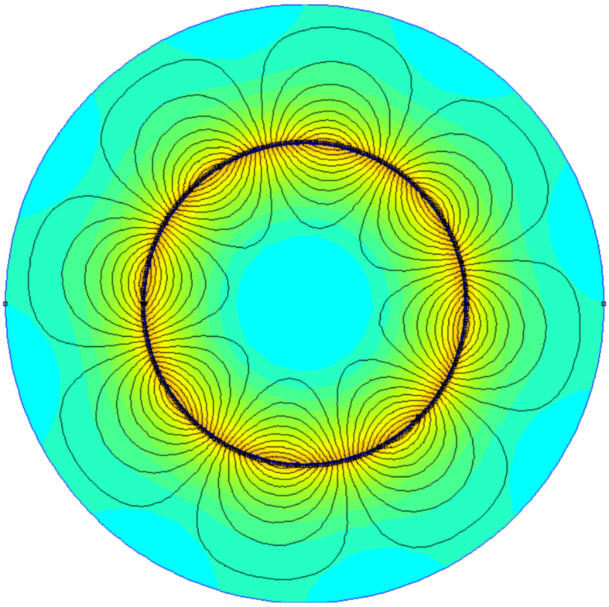

Fig. 5.14 Ideal stator coupled with an iron rotor : flux density plot considering the application of the harmonic$h = 4$.

In order to verify the results some of the harmonics of the machine $q = 1/4$ have been applied. The harmonic spectrum of the machine $q = 1/4$ is reported in Fig 5.15.

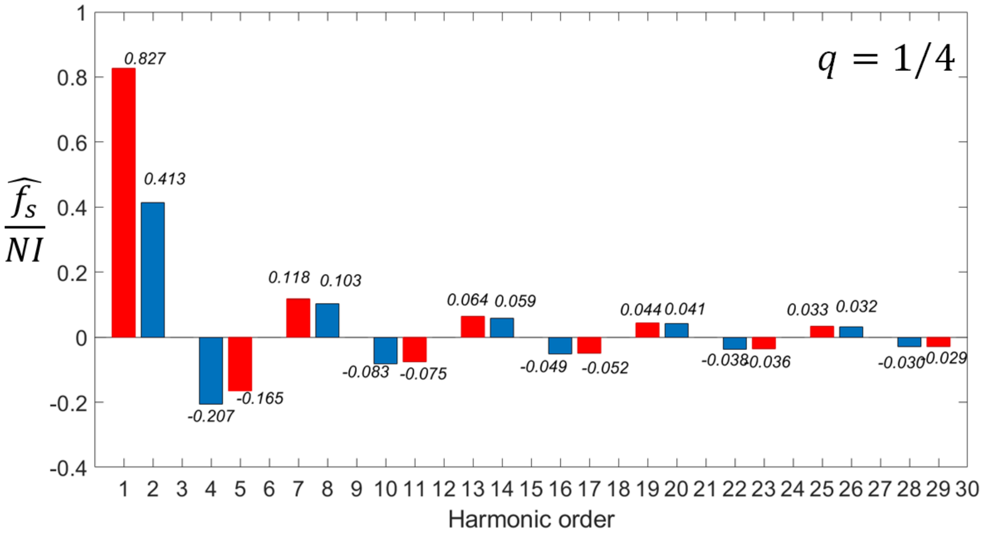

Fig. 5.15 Harmonic spectrum for the machine $q = 1/4$.

In Fig. 5.15 the harmonics that contribute mirror torque are reported in blue. In red are reported the harmonics that contribute to the mixed torque. Thanks to the specific stator designed for the validation it is possible to apply each harmonic once a time or all together in order to evaluate the results.

The flux density plot when the harmonic $h = 1$, $h = 2$ and $h = 4$ are applied are reported in Fig. 5.16.

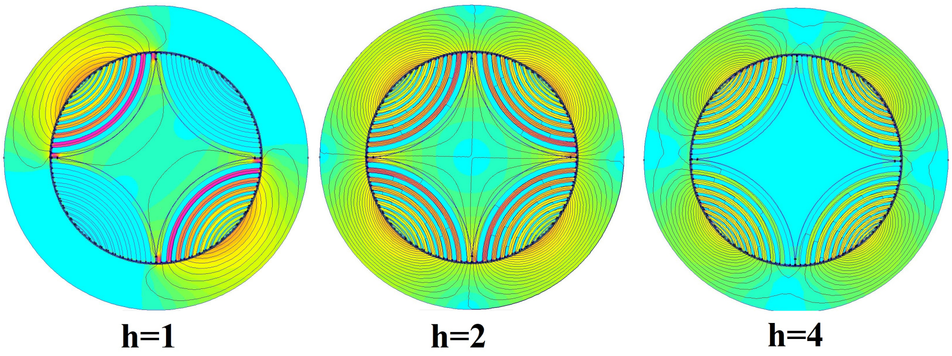

Fig. 5.16 Ideal stator coupled with an the ideal rotor: Flux density plot for different harmonic orders.

The rotor reaction to the sub harmonic, to the synchronous harmonic and to the multiple harmonics are reported in the Fig. 5.17, Fig. 5.18, Fig. 5.19 .

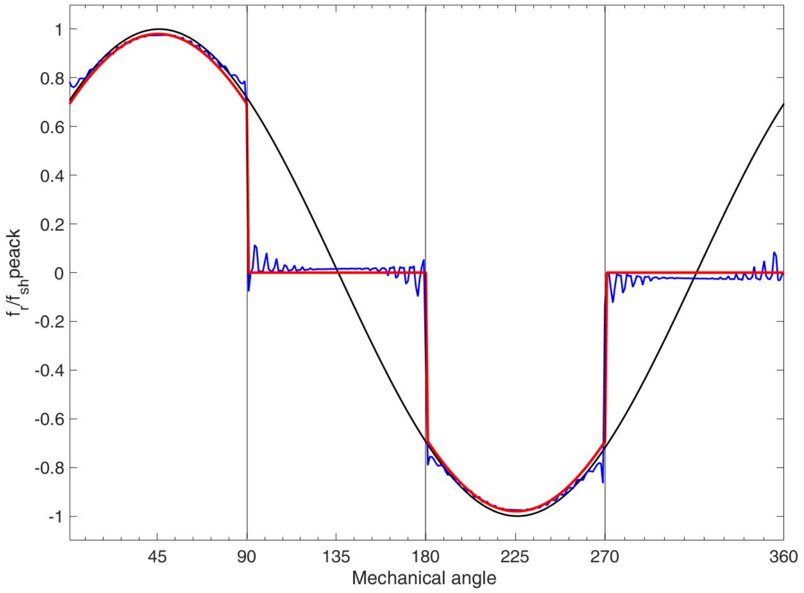

Fig. 5.17 Rotor reaction to the sub-harmonic h=1.

In order to evaluate the torque, time stepping simulations have been performed. In the simulations the rotor is moved for each step according to the synchronous

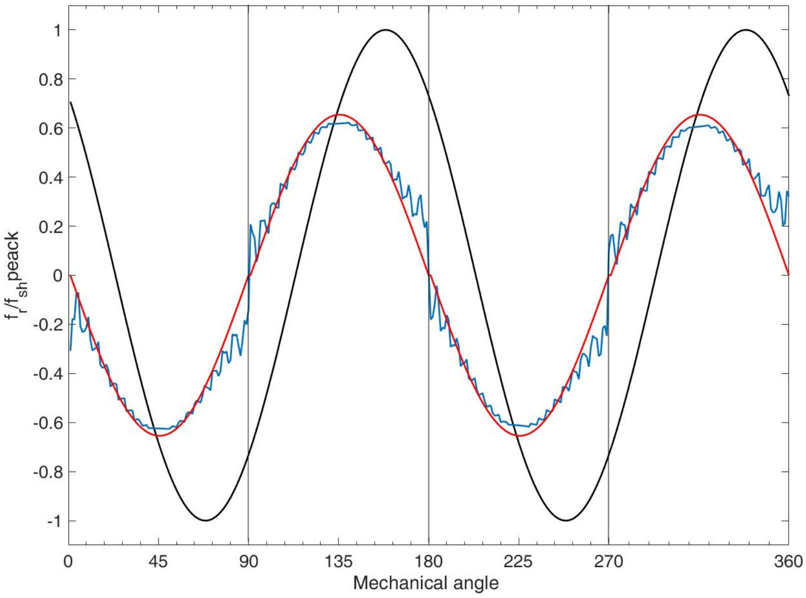

Fig. 5.18 Rotor reaction to the synchronous harmonic h=2.

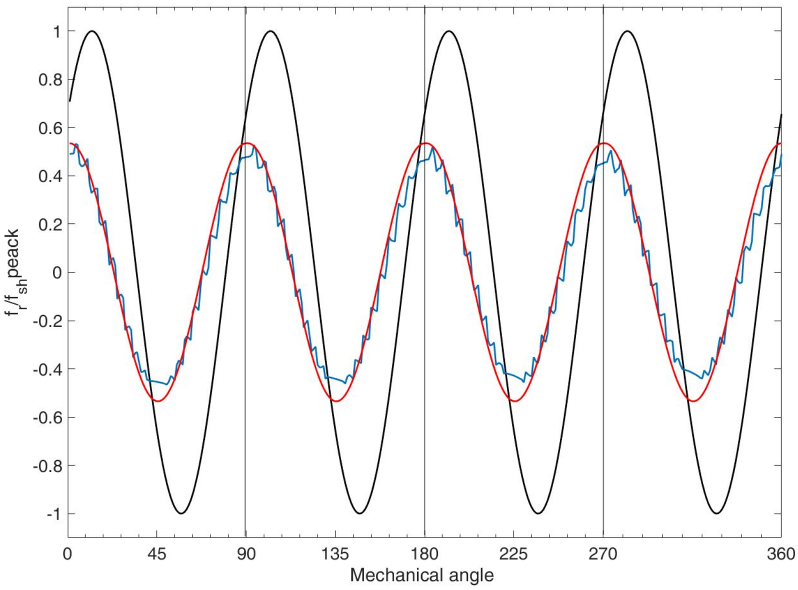

Fig. 5.19 Rotor reaction to the harmonic h=4.

harmonic. By the application of the stator harmonics that contribute to the mean torque and to the 6^{th} torque ripple harmonic the torque results in Fig. 5.20.

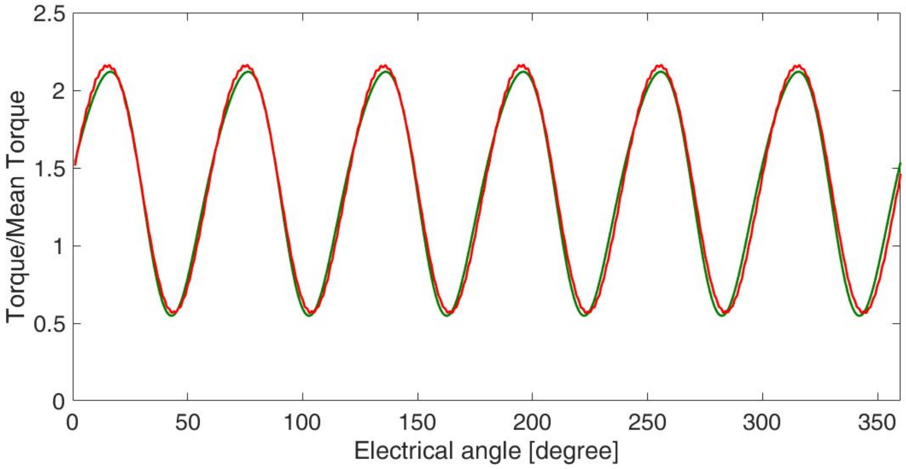

Fig. 5.20 Simulation results (in red) vs analytical calculation (green line) over an electric period for the machine $q = 1/4$ considering the application of the harmonics that contribute to the mean torque and to the 6^th torque ripple harmonic.

5.6 Conclusions

In this Chapter a mathematical model is proposed in order to evaluate the torque and the torque ripple in SyR solutions. A pole-per-pole approach has been followed and allows to highlight the non uniform rotor reaction, when harmonics not multiple of pole pairs are present, and to understand the mechanism of the torque ripple production in SyR FSCW solutions. The main results is that, in a SyR machine with a number of pole pair odd, only the harmonics multiple of pole pair can contribute to the torque and then only the mirror torque formulation must be considered. In the case of pole pair even, the cross effect of harmonics not multiple of pole pair must to be taken into account through the mixed torque formulation.

For the harmonics not multiple of pole pairs the rotor reaction has a jump across the d-axis. In the real case, at least in the positive one, this jump is not physically acceptable. Adjacent poles in fact react to the same harmonic in different way forcing the spider to assume locally different potential. Across the d-axis a rotor reaction imposed the continuity of the potential. As a consequence the rotor reaction will be modified. This has a direct impact on the torque components of the mixed torque for n=2 that result strongly reduced in their amplitudes. The model proposed offers a torque and torque ripple predicting formula in a generic m-phase machine in a $2p$ ideal rotor. Being the rotor able to react to each harmonic, the model proposed identifies also the worst case since, the filtering effect of the reduction of the segments or the specific rotor design are not considered. In addition looking forward to the real case, the analysis proposed here represents the starting point for the calculation of the rotor reaction in the case of a limited number of flux barriers. Starting from the ideal rotor reaction in equation (5.17) following a sampling and hold approach as in [73] it is possible to obtain the staircase rotor reaction. The torque expression can then be rewritten considering the typical staircase rotor function. All of this will allow to compare positive and negative rotor solutions. This development is part of a work in progress that is not reported in the thesis.

Chapter 6

Conclusions

The aim of the research was to investigate the advantages introduced by multiphase synchronous electric machines with a simple structure, mainly focusing on the advantages in terms of torque performance. The stator structure chosen was the tooth-coil wound because of its realization and maintenance simplicity. The combination of multiphase machine and tooth-coil woundings allows to obtain a very simple structure with a limited harmonic spectrum in the magnetic field if some specific rules are chosen. A generalized algorithm to identify the right stator-rotor coupling in order to obtain a tooth-coil wound machine with a very low torque ripple contribution is presented, and some examples of the proposed algorithm are reported. The harmonic field produced by the generic multiphase tooth-coil wound stator was studied analytically. An analytical model that allows to estimate the torque for Surface Mounted Permanent Magnet (SMPM) Multiphase machines is proposed. The model was validated by Finite element analysis (FEA) for different multi-3-phase motor solutions. Between all the possible solutions the triple-3-phase one was deeply analysed. Different rotor solutions have been considered. The design results in a 9-phase 10-poles SMPM machine. An inset rotor solution has been studied considering three different permanent magnets configurations and appear like a good compromise solution when bandaging wants to be avoided. The motor designed by following the specific rules, exhibits a very low torque ripple value. The torque ripple harmonics are the ones predicted by FEA and by the model. Although small, additional harmonics are present due to constructive defects in the mechanical machine realization, and due to the presences of radial forces not taken into account in the FEA or in the modelling. The experimental results suggest to execute multiphysics simulations in order to investigate the effect of the radial forces on the torque ripple. Otherwise, despite its simplicity, the machine tested results in a very low torque ripple solution. An improvement of the performance can be obtained by repeating the machine two times. The machine built is simple, maintainable and suitable for integration with the power electronic especially if the COOL-TIE concept presented is implemented. The cost of this simplicity in the motor realization is in the increased converter complexity. Otherwise additional advantages for the converter point of view exist. In this thesis an additional degree of freedom, the PWM shifting between carriers, has been studied. A control strategy was proposed, fully analysed by simulation and then tested. The control technique proposed allows to obtain a significant reduction of the dimensioning DC-link rms current. The research was extended to multiphase tooth-coil wound Synchronous Reluctance machine (SyR) and an analytical model for torque calculation was presented. A pole-per-pole approach has been followed and allows to highlight the non uniform rotor reaction, when harmonics not multiple of pole pairs are present, and to understand the mechanism of the torque ripple production in SyR FSCW solutions. The analysis is limited to an ideal rotor and represent the starting point for a generalized theory that allows to study and compare positive and negatives multiphase SyR solutions independently by the flux barrier design.

Appendix A

Constant Permeance 2p SyR rotor

Lets us consider an ideal rotor pole of a machine with 2p poles characterized by a very large number of rotor barriers, as in Fig.A.1. This can be seen as a sort of "distributed anisotropy" pole. The q axis of this pole is defined at the center of this pole and from this axis the mechanical coordinate ξ is defined and is positive in the clockwise direction. Is then considered the application of the sinusoidal stator MMF of harmonic h as in (A.1) where the dependence of time is contained in φ:

$$f_{s_h} = \hat{f_{s_h}} cos\left(h\xi - \varphi\right) \tag{A.1}$$

This can be always split into two components, being odd and even functions with respect the q axis (A.2),(A.3).

$$2f_{d_h} = f_{s_h}\left(-\xi\right) - f_{s_h}\left(\xi\right)) \tag{A.2}$$

$$2f_{q_h} = f_{s_h}\left(-\xi\right) + f_{s_h}\left(\xi\right) \tag{A.3}$$

The rotor pole reacts to the q axis component of the stator MMF by an even magnetic potential distribution $f_{r_h}(\xi)$. But the rotor magnetic potential $f_{r_h}(\xi)$ is not sinusoidal, in general, due to the rotor shape.

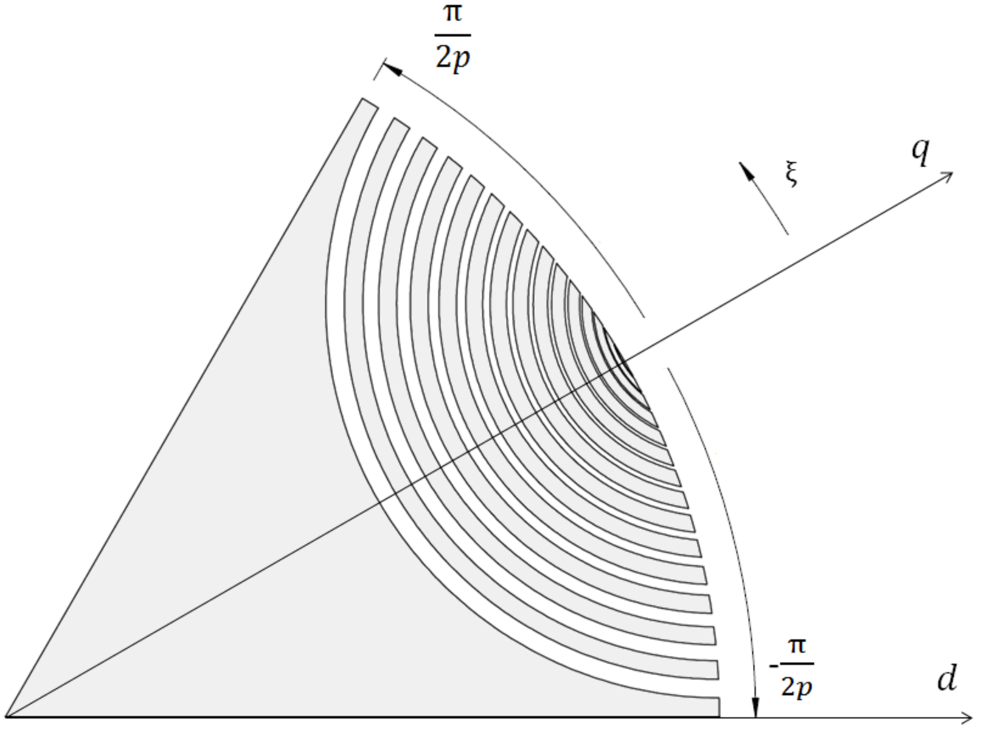

Fig. A.1 Definition of the refernce frame ξ for a generic pole of an ideal rotor with a very large number of rotor barriers

In this Appendix is demonstrated that the rotor reaction is still sinusoidal of the same h order of the stator MMF, if the permeance of each flux barrier is constant. Then the rules to obtain a constant permeance rotor are presented.

As done in [74] a differential analysis can be conducted considering a rotor segment very thin. According to [74] and considering the rotor geometry in Fig A.4 the permeance parameter can be expressed by (A.4).

$$\rho(\xi') = \frac{f(\xi')}{a(\xi')} \tag{A.4}$$

in which $f(\xi')$ is the lamination shape equal to A.5 and $a(\xi)$ is the ratio between non magnetic and magnetic materials in the segments, that can be a function of the rotor coordinate ξ' in general . The lamination shape function depends by half-length of a lamination $y(\xi')$ and by the angle ς.

$$f(\xi') = \frac{y(\xi')}{\frac{dx}{d\xi'}} \tag{A.5}$$

As a consequences the parameter permeance results in (A.6).

$$\rho(\xi') = \frac{y(\xi')}{Ra(\xi')sen\varsigma(\xi')} \tag{A.6}$$

Since each flux barrier is supposed to have constant thickness, the inside flux density B_{a_h} is uniform and can be written as in (A.7), where f_{r_h} is the rotor magnetic potential related to the h^{th} harmonic order of the stator MMF.

$$B_a = \mu_0 \frac{df_{r_h}}{a(\xi')dx} \tag{A.7}$$

Introducing the parameter ρ equation (A.8) results in which the term $B_a y$ represents one half the flux flowing through the flux barrier identified by ξ'. The flux flowing trough the flux barriers is also called adjacency flux.

$$B_a y = \mu_0 \rho(\xi') \frac{df_{r_h}}{d(\xi')} \tag{A.8}$$

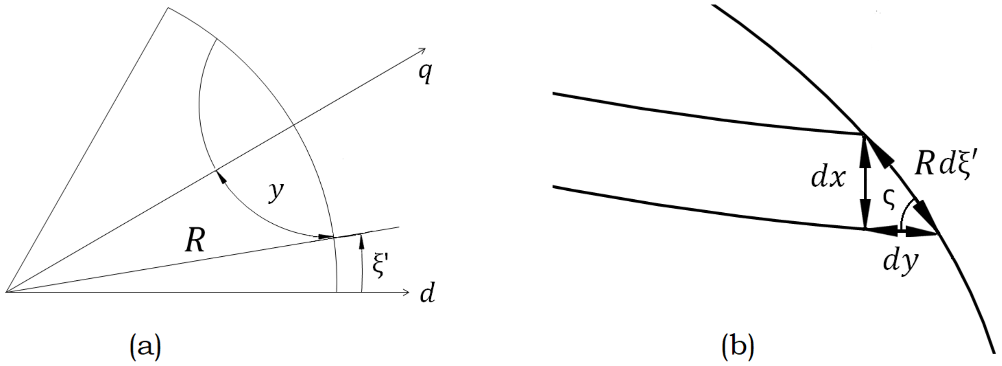

(a) (b)

Fig. A.2 Rotor geometry parameter.The picture is reproduced from I. Marongiu and A. Vagati, Improved modelling of a distributed anisotropy synchronous reluctance machine, presented in Conference Record of the 1991 IEEE Industry Applications Society Annual Meeting.

With reference to the schematic magnetic segment in Fig. A.3 the flux balance can be written in A.9

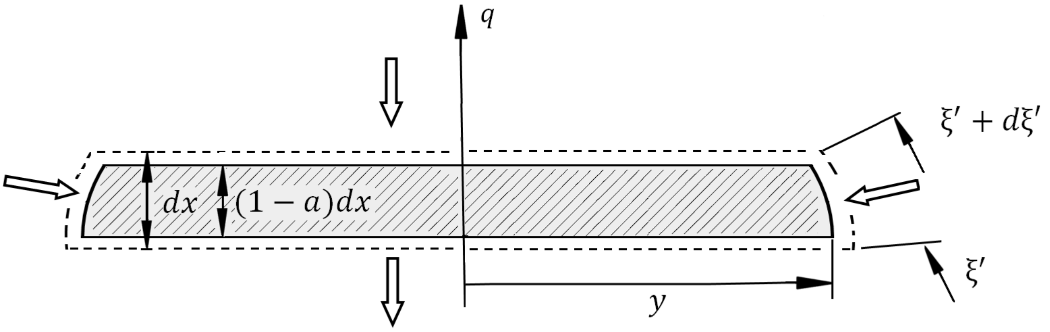

Fig. A.3 Balance of the flux across the lamination. The picture is reproduced from I. Marongiu and A. Vagati, Improved modelling of a distributed anisotropy synchronous reluctance machine, presented in Conference Record of the 1991 IEEE Industry Applications Society Annual Meeting.

$$-d\left(B_{a_h} y\right) = B_{q_h} \cdot R \cdot d\left(\xi'\right) \tag{A.9}$$

Being

$$B_{q_h} = \mu_0 \left(f_{q_h} - f_{r_h}\right) \tag{A.10}$$

Moving from d to q axis the decrement of the adjacency flux is compensated by the symmetrical q-axis at the rotor surface.

From (A.9) and (A.8) the equation (A.11) results

$$\rho \left(\frac{d^2 f_{r_h}}{d\xi'^2}\right) + \left(\frac{d\rho}{d\xi'}\right)\left(\frac{d f_{r_h}}{d\xi'}\right) + \frac{R}{g}\left(f_{q_h} - f_{r_h}\right) = 0 \tag{A.11}$$

where g is the constant airgap. If the applied MMF is sinusoidal the f_{r_h} is not, in general, due to the terms $(\frac{d\rho}{d\xi'})$. But if the permenance $\rho(\xi')$ is constant the equation (A.11) reduces in to the linear and costant coefficient equation in (A.12) and the f_{r_h} results sinusoidal too. Being $\xi' = xi + \pi/p$ then $d\xi' = d\xi$.

$$f_{q_h} - f_{r_h} = -\frac{g}{R}\rho \frac{d^2 f_{r_h}}{d\xi^2} \tag{A.12}$$

From (A.12), let us observe that the first term in the expression multiplied by μ_o/g represent the q component of the airgap flux density. The q component of the pole flux density is then obtained by integrating this component across the pole span. As a consequence the q component of the pole flux results proportional to the derivative $dfr_h/d\xi$ calculated at the pole border $\pi/2p$.

By substitution of the (A.1) and (A.3) in (A.12) equation (A.13) results.

$$f_{r_h} = \frac{\hat{f_{q_h}} \cos(h\xi)}{1 + \frac{g}{R}\rho h^2} \tag{A.13}$$

In practice, the rotor magnetic potential is a sinusoidal function in phase with f_{q_h} but of a reduced amplitude. The reduction coefficient is given in (A.14) that become heavier and heavier when the harmonic order increases. This means that the salient behaviour of the ideally rotor rapidly decrease as harmonic order multiple of p are increased.

$$k_h = \frac{1}{1 + \frac{g}{R}\rho h^2} \tag{A.14}$$

In order to obtain a parameter $\rho(\xi')$ constant the percentage of air $a(\xi')$ must to change according with $y(\xi')$ and $\varsigma(\xi')$ as in (A.15).

$$a(\xi') = \frac{y(\xi')}{R\rho sen\varsigma(\xi')} \tag{A.15}$$

By geometric consideration from Fig.A.4 equations (A.16),(A.17),(A.18),(A.19) and (A.20) results.

$$y(\xi') = r(\xi')\beta(\xi') \tag{A.16}$$

$$r(\xi') = \frac{2Rsin\left(\frac{\xi'}{2}\right)^2}{sin\beta} \tag{A.17}$$

$$\beta'(\xi') = \sin^{-1}\left(\frac{R}{r(\xi')}\sin\left(\frac{\pi}{2p} - \xi'\right)\right) \tag{A.18}$$

$$\beta(\xi') = \frac{\pi}{2} - \frac{\pi}{2p} - \beta'(\xi') \tag{A.19}$$

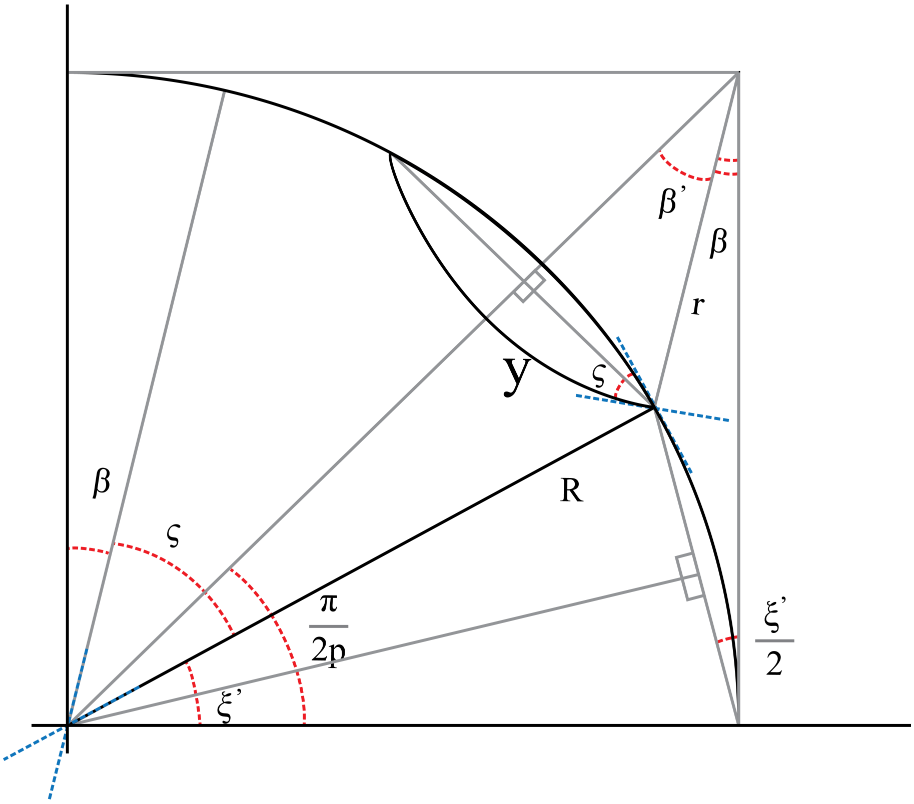

Fig. A.4 Design parameters that define the permeance in the rotor.

$$\varsigma\left(\xi'\right) = \frac{\pi}{2} - \xi' - \beta\left(\xi'\right) \tag{A.20}$$

Fig A.5 reports the function $a(\xi')$ for different poles fixing the initial amount of air $a(0) = 0.5$. The corresponding value of ρ are reported. The parameter ρ assumes value equal to 2 for pole pairs $p = 1$ (for which the parameter $a(\xi')$ is constant) and reduces going to p greater.

Following the formulas reported in this appendix it is possible to obtain a constant permeance rotor, an ideal rotor, able to react to the q component of the generic harmonic h of the stator MMF with a rotor magnetic potential that is still sinusoidal of the same order h.

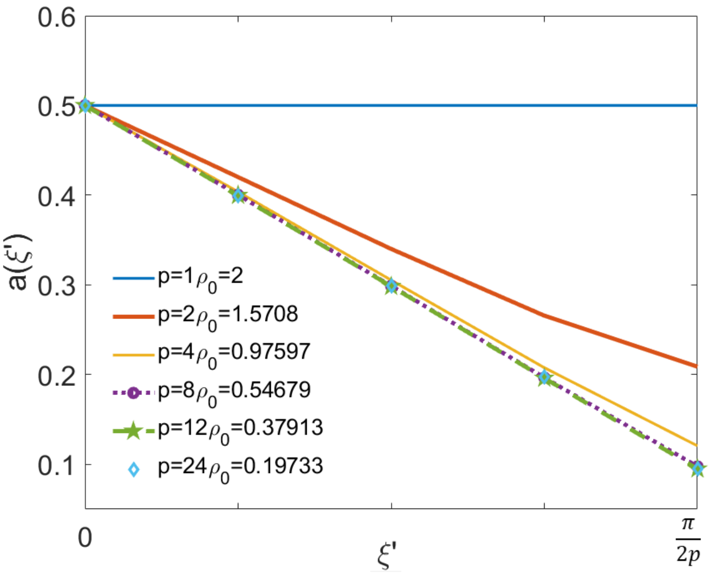

Fig. A.5 Air ratio $a(\xi')$ in order to have constant permeance in each flux barrier.

Appendix B

Manufacturing Process

The machine has been designed in all its parts (Fig. B.1) in order to have a motor that can be easily manufactured and easily maintained.

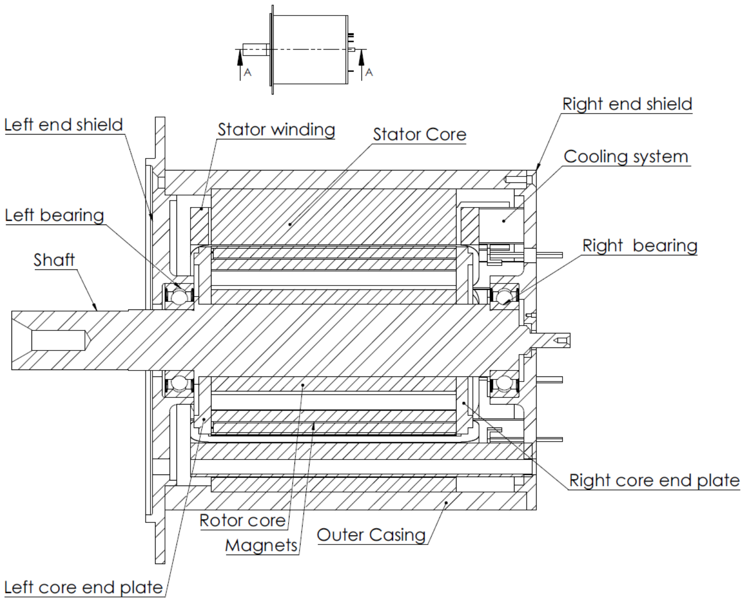

Fig. B.1 Electrical motor components

All the assembly steps are here reported.

The iron available is a pre-glued M250 35A. The stator and the rotor pack was obtained from the iron block in Fig. B.2 with the dimension $140 * 140 * 104mm$ using wire Electrical Discharge Machining (EDM).

Fig. B.2 Pre glued iron block M250-35A and the stator obtained by EDM

The stator was positioned in the outer casing with thermal interference fit. The stator position must be controlled in order to achieve an alignment between the two end shields of the motor frame. This allows an easier connection of the wire terminals and the installation of the cooling system designed, that is described in the next section. In order to execute the centring of the stator in the stator frame the scrap of the stator from the EDM process (the negative) in Fig. B.3 can be used like a guide. Three pins screwed on the frontal shield and connected to the negatives of the stator allow the correct positioning inside to the casing. These three elements were then placed in an oven until they reach 120 ° C, and after the extraction, the stator lowered into the heated pieces. The negative acts like a guide for the stator allowing the correct centring. The thermal contraction of the aluminium of the stator casing put the stator and the casing in contact by interferences. The maximum achievable precision is in the order of $+-0.2mm$. That is two times the tolerances of the EDM process.

As discussed previously the windings are tooth coil wound obtained from 9 preformed coils. The coil was made from copper enameled wire (magnet wire) in order to create a better fill factor . The coil realized is shown in Fig. B.10. A Nomex sheet was placed on the surface of the coil in contact with the iron.

Before mounting, the coil was compacted. A forming system was realized in order to compact the windings in terms of the width and hight. Then this forming system and the coil that needs to be formed was put in a press and the end connection was modelled to better fit into the available space. The coils were putted in contact

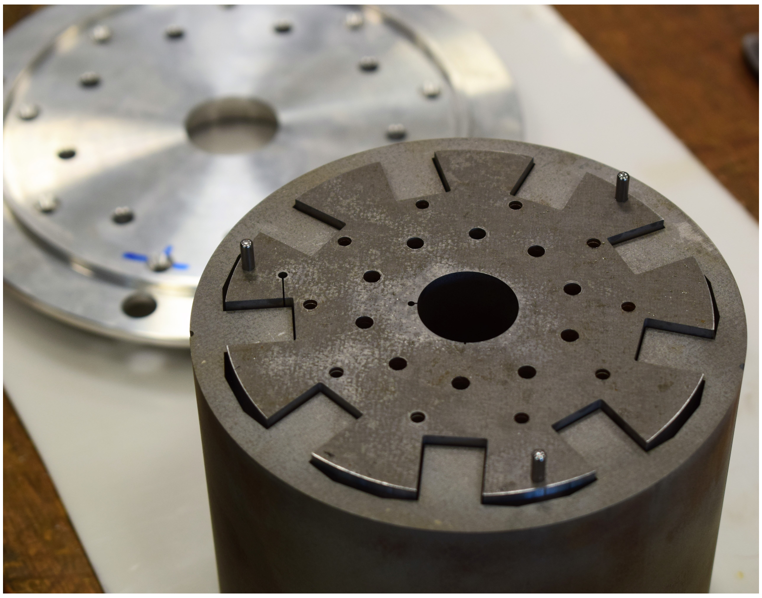

Fig. B.3 Negatives of the stator from the EDM process positioned inside the rotor. In the picture it is possible to see the pins

with the stator without any glue or resin. This was done to place the cooling system (not yet available) and to allow the reversibility of the operation in case damage to the insulation. A fixing by resin under pressure can be done in a second time.

The rotor pole was designed with an housing slot for the magnets. Some attention must be done in the position of the magnets in the housing slots. In order to avoid that the repulsion of the magnets push them out of the housing slots, the scrap of the rotor from the EDM process was used. The rotor was positioned inside the negatives of the rotor and the insertion of the magnets starts . Glue was used inside the hosting slots in order to facilitate the placement of the magnets and once cures to keep the magnets inside the rotor.

For the solution called array of magnets, commercial magnets of dimension $4mm * 4mm * 20mm$ were chosen. Each housing slot can contain five rows of five magnets side by side. The magnets have a precision of $\pm 0.1mm$. For the solution characterized by customized magnets with axial magnetization five rows of 1 magnets can be used.

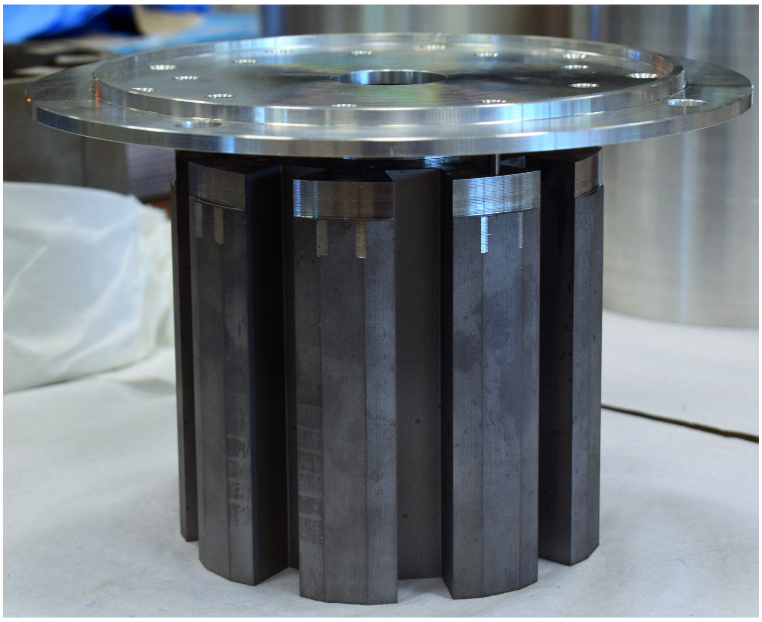

Fig. B.4 Negatives of the stator from the EDM process connected to the frontal shield.

B.0.1 Constrait and drownback

Electrical Discharge Machining make it possible to machine complex form with high precision thanks with the finishing processes. Otherwise some complication can occur during electro erosion. Surface problems are generated by residue of material between the electrode and the iron, that can be present if the filtering system of the dielectric liquid is not effective. In Fig. B.11 the lamination and the corrosion phenomena are well evidenced. In addition, electrolytic corrosion can occur,even if the material is corrosion resistant, due to the eddy currents that interact with the metal ions that can corrode the machined piece. This situation can worsen if the duration of the increases. In addition this corrosive phenomena has the potential to cause cracks that can affect the straight of the piece.

The observation of the cutting surface in Fig B.11 shown that the corrosion is present more in the internal surface of the stator than in the external surface. Corrosion is in our application very damaging since lead all the laminated pack in short circuit. In order to remove the oxide present on the surface of the packs a sandblasting procedure can be performed.

Another problem found in the first prototype is related to the use of the array of magnets. This solution, although cheaper, is very risky and the process of positioning

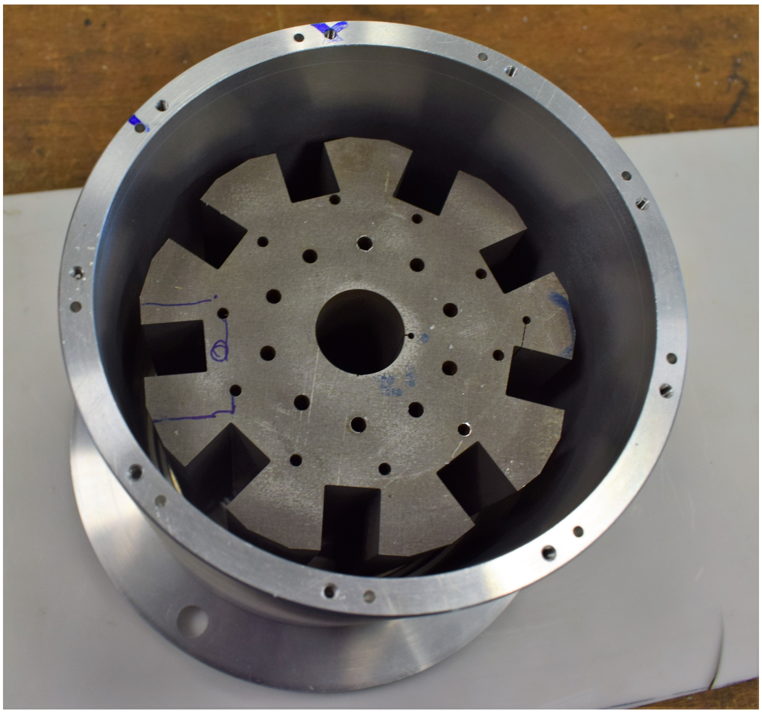

Fig. B.5 Negatives of the stator from the EDM process inside the external casing in order to allow the correct positioning of the stator.

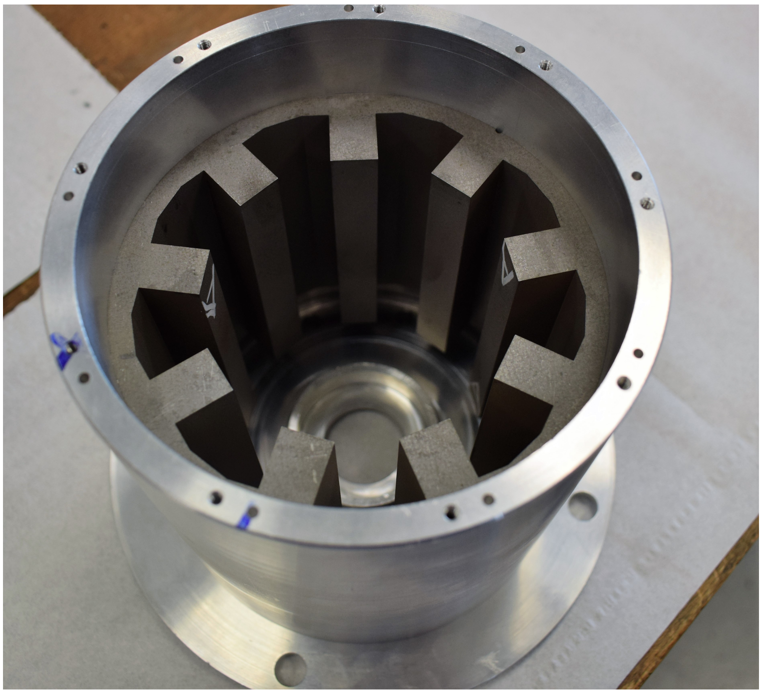

Fig. B.6 Final position of the stator inside the casing.

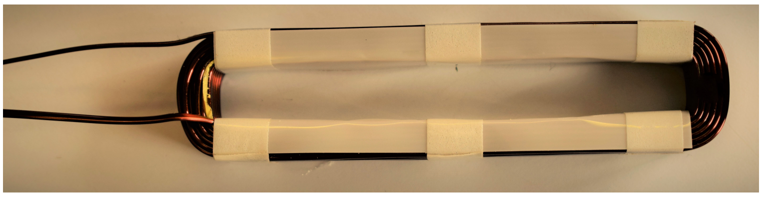

Fig. B.7 Tooth coil, number of turn per coil 42.

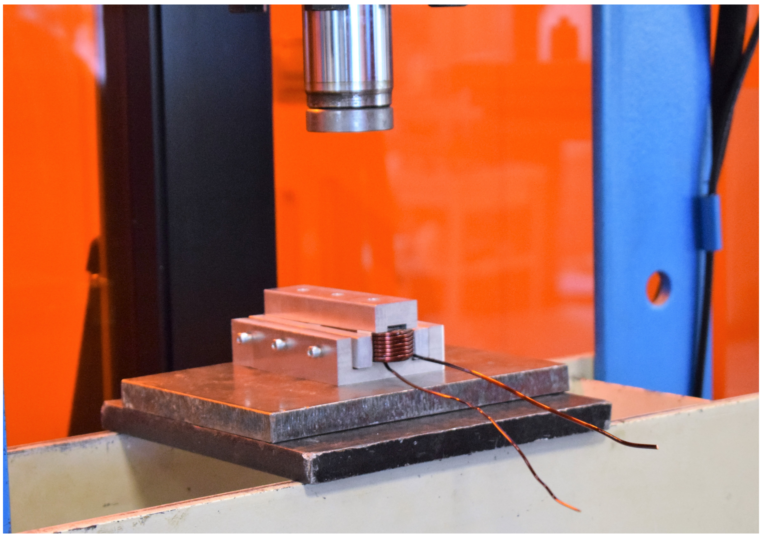

Fig. B.8 Tooth coil former in the press.

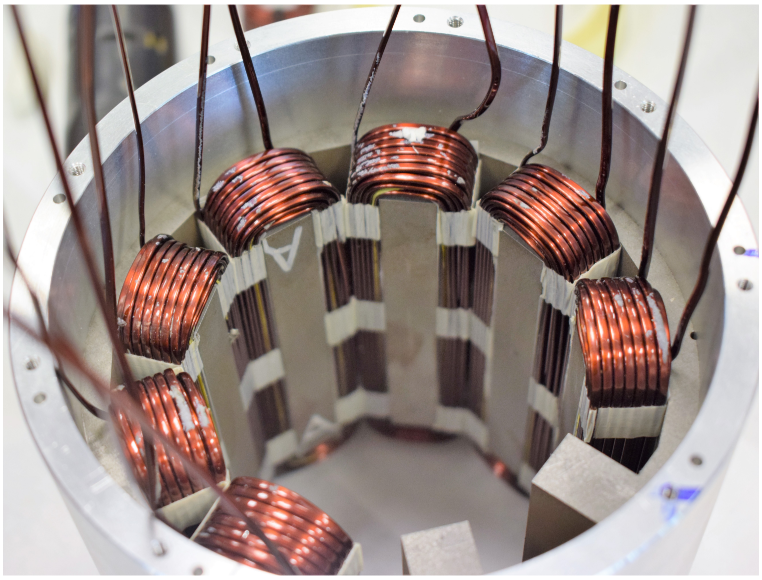

Fig. B.9 Tooth coil former in the press.

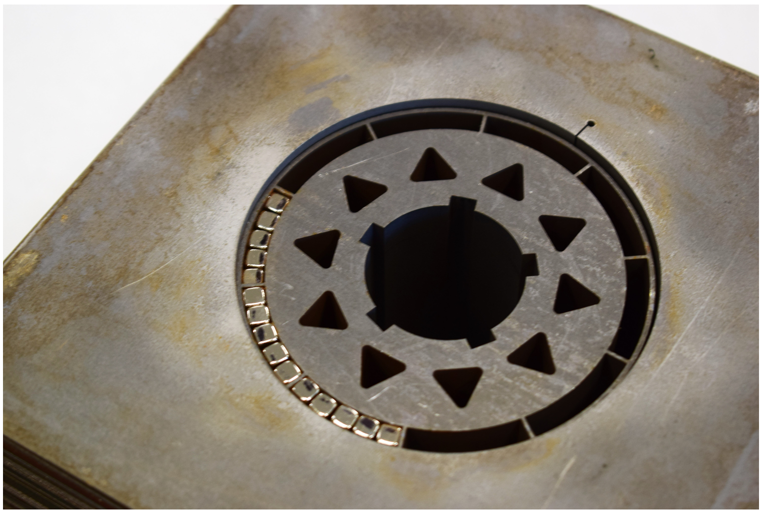

Fig. B.10 Inset rotor inside its negative from EDM.

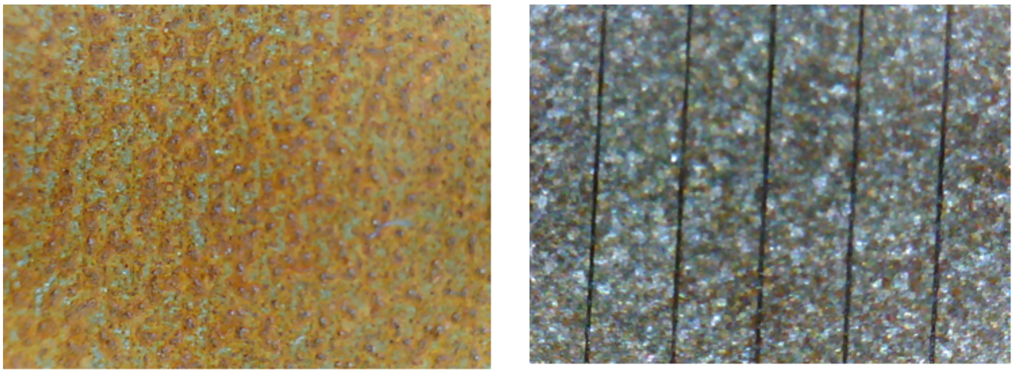

Fig. B.11 Oxidation phenomena after EDM process. On the left the internal stator surface with oxidation, and in the right the external rotor surface

of the magnets it is very time consuming. In the first prototype realized some magnet along the axis of the machine has assumed a unwanted position that lead to some asymmetry in the rotor. Another rotor has been realized with the use of customized magnet with parallel magnetization.

An additional problem is related to the not perfect shaping of the coils. The forming process in fact has damaged the insulation of the coils and during the electric discharges occurs. This operation must then to be avoided.

Appendix C

The COOL-TIE concept

The solution here briefly proposed is under patenting process and is part of a proof of concept under the acronym COOL-TIE (COOLing Topologies for Integrated Electric Drives) financed by Politecnico di Torino.

The machine has been thought to simplify the manufacturing process. The void space in the slot, between two adjacent space can be used in order to realize a thermal exchange channel. In this way it is possible to realize a simple direct cooling system. This allow to obtain an increment in the power density of the drive in small, medium applications $(under 100 kW)$. Typically the direct cooling system is used in fact in hight power application. For small application direct cooling solutions are not typically used since results in a complicated structure for a series production.

In particular is possible to design a cooling devices for an electric machine that can be put in thermal exchange with the stator winding. The shape of the device chosen is reported in picture Fig. C.1, in Fig. C.2, Fig. C.3 .

The shape is of the device is elongated and present a cross-section which is compatible with the cross-section of a cavity within the stator.

The material of the channel must have a greater thermal conductivity than the material of the stator (higher than $100W/(mK)$). In addition a good electric resistivity higher than $1.0\omega m$ and a good dielectric rigidity positioned between two phases. If a material characterized by an hight dielectric rigidity (greater than $1MV/m$) is chosen an improvement of the reliability can be obtained or in other terms a higher voltage level can be used. Of course the material chosen must he be not magnetic in order

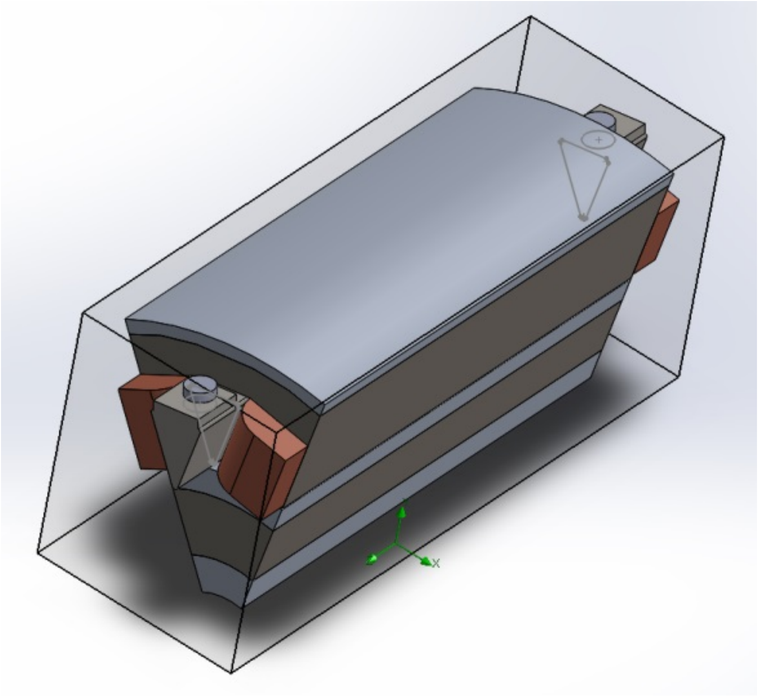

Fig. C.1 Cooling device

to not change the flux distribution in the machine. The device has been though to have a duct for the passage of a refrigerating fluid. The material chosen must to be resistant to corrosion.

Among the materials the more promising is the Silicon carbide (SiC or SiSiC). Another possible material is the Aluminum Nitride (AlN) but its mechanical fragility not allows to obtain feasible solutions due to the shape chosen.

The devices characteristic are compatible with a power electronic integration. The device can host part of the power electronic, at least the power modules, on its surface. Power electronic and motor can share the same cooling system with a direct reduction of the spaces. In an integrated solution the cable length between motor and inverter is reduced with advantages in terms of overvoltages on the motor side [75], and allows to obtain a better International Protection Rating (IP). It is worth noticing that the proximity between power electronic and motor allows to reduce the problem related to Electromagnetic interference (EMI) and Electromagnetic Compatibility (EMC).

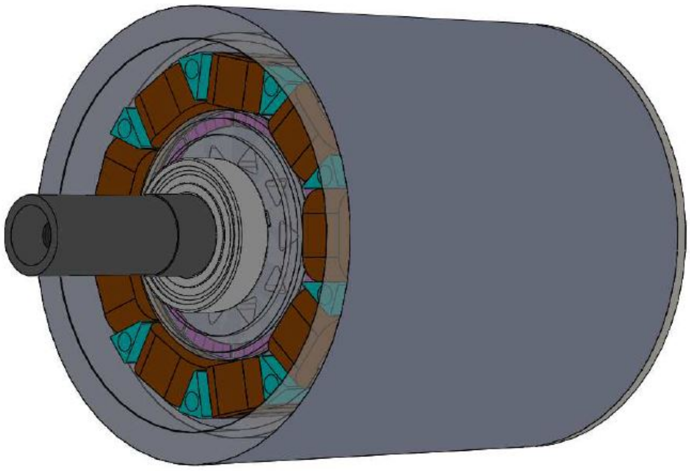

Fig. C.2 Electrical motor with direct cooling system

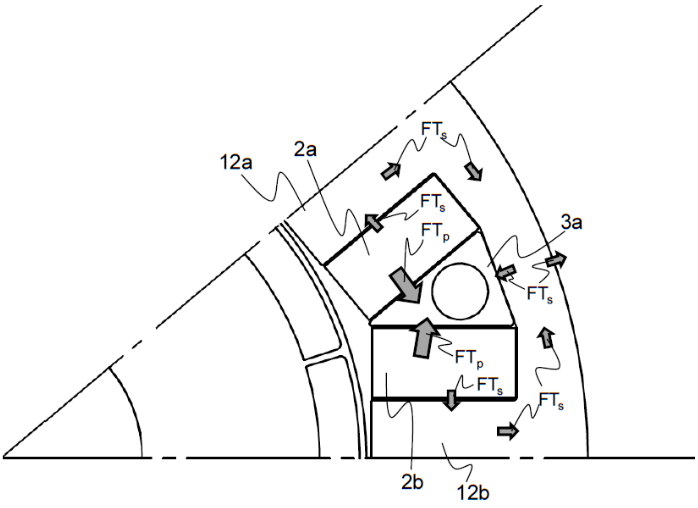

Fig. C.3 Thermal fluxes in the system

References

[1] P. Guglielmi, M. Diana, G. Piccoli, and V. Cirimele. Multi-n-phase electric drives for traction applications. In *Electric Vehicle Conference (IEVC), 2014 IEEE International*, pages 1–6, Dec 2014.

[2] E. Levi. Multiphase electric machines for variable-speed applications. *Industrial Electronics, IEEE Transactions on*, 55(5):1893 –1909, may 2008.

[3] L. Parsa. On advantages of multi-phase machines. In *Industrial Electronics Society, 2005. IECON 2005. 31st Annual Conference of IEEE*, pages 6 pp.–, Nov 2005.

[4] E. Fornasiero, N. Bianchi, and S. Bolognani. Rotor losses in fractional-slot three-phase and five-phase pm machines. In *Electrical Machines (ICEM), 2010 XIX International Conference on*, pages 1–5, Sept 2010.

[5] C.L. Ferreira and R.W.G. Bucknall. Modelling and real-time simulation of an advanced marine full-electrical propulsion system. In *Power Electronics, Machines and Drives, 2004. (PEMD 2004). Second International Conference on (Conf. Publ. No. 498)*, volume 2, pages 574–579 Vol.2, March 2004.

[6] F. Caricchi, F. Crescimbini, and O. Honrati. Modular axial-flux permanent-magnet motor for ship propulsion drives. *IEEE Transactions on Energy Conversion*, 14(3):673–679, Sep 1999.

[7] T. McCoy and M. Bentamane. The all electric warship: An overview of the u.s. navy's integrated power system development programme. *Conf. ELECSHIP*, page 1–4, 1998.

[8] A Tessarolo, S Castellan, and R Menis. Feasibility and performance analysis of a high power drive based on four synchro-converters supplying a twelve-phase

synchronous motor. In *2008 IEEE Power Electronics Specialists Conference*, 2008.

[9] D. Vizireanu, X. Kestelyn, S. Brisset, P. Brochet, and E. Semail. Experimental tests on a 9-phase direct-drive pm axial-flux synchronous generator. *ICEM 2006*, (paper reference no 509), 2006.

[10] S. Brisset, D. Vizireanu, and P. Brochet. Design and optimization of a nine-phase axial-flux pm synchronous generator with concentrated winding for direct-drive wind turbine. *Industry Applications, IEEE Transactions on*, 44(3):707–715, May 2008.

[11] R. Bojoi, A. Cagnagnino, A Tessarolo, and S Vaschetto. Multiphase electrical machines and drives in the transportation electrification. In *Research and Technologies for Society and Industry (RTSI) 2015 IEEE 1th International Conference*, Sept 2015.

[12] A. Bruyere, E. Semail, A. Bouscayrol, F. Locment, J.M. Dubus, and J.C. Mipo. Modeling and control of a seven-phase claw-pole integrated starter alternator for micro-hybrid automotive applications. In *Vehicle Power and Propulsion Conference, 2008. VPPC '08. IEEE*, pages 1–6, Sept 2008.

[13] Mehdi T. Abolhassani. A novel multiphase fault tolerant high torque density permanent magnet motor drive for traction application. *Electric Machines and Drives, IEEE International Conference*, 2005.

[14] J. Riveros, B. Bogado, J. Prieto, F. Barrero, S. Toral, and M. Jones. Multiphase machines in propulsion drives of electric vehicles. In *Proceedings of 14th International Power Electronics and Motion Control Conference EPE-PEMC 2010*, pages T5–201–T5–206, Sept 2010.

[15] R. Bojoi, A. Cavagnino, M. Cossale, A. Tenconi, and S. Vaschetto. Design trade-off and experimental validation of multiphase starter generators for 48v mini-hybrid powertrain. In *Electric Vehicle Conference (IEVC), 2014 IEEE International*, pages 1–7, Dec 2014.

[16] R. Bojoi, A. Cavagnino, M. Cossale, and A. Tenconi. Multiphase starter generator for 48v mini-hybrid powertrain: Design and testing. In *Power*

Electronics, Electrical Drives, Automation and Motion (SPEEDAM), 2014 International Symposium on, pages 1319–1324, June 2014.

[17] L. Parsa, H.A. Toliyat, and A. Goodarzi. Five-phase interior permanent-magnet motors with low torque pulsation. *Industry Applications, IEEE Transactions on*, 43(1):40–46, Jan 2007.

[18] L. Parsa and Taehyung Kim. Reducing torque pulsation of multi-phase interior permanent magnet machines. In *Industry Applications Conference, 2006. 41st IAS Annual Meeting. Conference Record of the 2006 IEEE*, volume 4, pages 1978–1983, Oct 2006.

[19] F. Scuiller, J. Charpentier, and E. Semail. Multi-star multi-phase winding for a high power naval propulsion machine with low ripple torques and high fault tolerant ability. In *Vehicle Power and Propulsion Conference (VPPC), 2010 IEEE*, pages 1–5, Sept 2010.

[20] Y. Burkhardt, A. Spagnolo, P. Lucas, M. Zavesky, and P. Brockerhoff. Design and analysis of a highly integrated 9-phase drivetrain for ev applications. In *Electrical Machines (ICEM), 2014 International Conference on*, pages 450–456, Feb 2014.

[21] B. Aslan, E. Semail, J. Korecki, and J. Legranger. Slot/pole combinations choice for concentrated multiphase machines dedicated to mild-hybrid applications. In *IECON 2011 - 37th Annual Conference on IEEE Industrial Electronics Society*, pages 3698–3703, Nov 2011.

[22] L. Parsa and H.A. Toliyat. Five-phase permanent-magnet motor drives. *Industry Applications, IEEE Transactions on*, 41(1):30–37, Jan 2005.

[23] J.M. Apsley, S. Williamson, A.C. Smith, and M. Barnes. Induction motor performance as a function of phase number. *Electric Power Applications, IEE Proceedings -*, 153(6), November 2006.

[24] S. Williamson and S. Smith. Pulsating torque and losses in multiphase induction machines. In *Industry Applications Conference, 2001. Thirty-Sixth IAS Annual Meeting. Conference Record of the 2001 IEEE*, volume 2, pages 1155–1162 vol.2, Sept 2001.

[25] P. Guglielmi, M. Diana, G. Piccoli, and V. Cirimele. Multi-n-phase electric drives for traction applications. In *Electric Vehicle Conference (IEVC), 2014 IEEE International*, pages 1–6, Dec 2014.

[26] M.T. Abolhassani. A novel multiphase fault tolerant high torque density permanent magnet motor drive for traction application. In *Electric Machines and Drives, 2005 IEEE International Conference on*, pages 728–734, May 2005.

[27] Michela Diana, Riccardo Ruffo, and Paolo Guglielmi. Pwm carrier displacement in multi-n-phase drives: An additional degree of freedom to reduce the dc-link stress. *Energies*, 11(2), 2018.

[28] Freddy Magnussen and Chandur Sadarangani. Winding factors and joule losses of permanent magnet machines with concentrated windings. *Electric Machines and Drives Conference,IEMDC 03*, 2003.

[29] R. H. Nelson and P. C. Krause. Induction machine analysis for arbitrary displacement between multiple winding sets. *IEEE Transactions on Power Apparatus and Systems*, PAS-93(3):841–848, May 1974.

[30] R. Bojoi, F. Farina, G. Griva, F. Profumo, and A. Tenconi. Direct torque control for dual three-phase induction motor drives. *Industry Applications, IEEE Transactions on*, 41(6):1627 – 1636, nov.-dec. 2005.

[31] F. Locment, E. Semail, and F. Piriou. Design and study of a multiphase axial-flux machine. *IEEE Transactions on Magnetics*, 42(4):1427–1430, April 2006.

[32] M. Diana, P. Guglielmi, and A. Vagati. Very low torque ripple multi-3-phase machines. In *IECON 2016 - 42nd Annual Conference of the IEEE Industrial Electronics Society*, pages 1750–1755, Oct 2016.

[33] Yi Sui, Ping Zheng, Fan Wu, Bin Yu, Pengfei Wang, and Jiawei Zhang. Research on a 20-slot/22-pole five-phase fault-tolerant pmsm used for four-wheel-drive electric vehicles. *Energies*, 7(3):1265–1287, 2014.

[34] E. Fornasiero, N. Bianchi, and S. Bolognani. Rotor losses in fractional-slot three-phase and five-phase pm machines. In *Electrical Machines (ICEM), 2010 XIX International Conference on*, pages 1–5, Sept 2010.

[35] Michela Diana, Paolo Guglielmi, Giovanni Piccoli, and Stefan George Rosu. Multi-n-phase smpm drives. In *Electric Machines Drives Conference (IEMDC), 2015 IEEE International*, pages 1011–1017, May 2015.

[36] Y. Burkhardt, A. Spagnolo, P. Lucas, M. Zavesky, and P. Brockerhoff. Design and analysis of a highly integrated 9-phase drivetrain for ev applications. In *Electrical Machines (ICEM), 2014 International Conference on*, pages 450–456, Sept 2014.

[37] J. Cros and P. Viarouge. Synthesis of high performance pm motors with concentrated windings. *Energy Conversion, IEEE Transactions on*, 17(2):248–253, Jun 2002.

[38] M. Diana, P. Guglielmi, G. Piccoli, and S. G. Rosu. Multi-n-phase smpm drives. In *2015 IEEE International Electric Machines Drives Conference (IEMDC)*, pages 1011–1017, May 2015.

[39] A. Tessarolo, L. Branz, and C. Bruzzese. A compact analytical expression for the load torque in surface permanent-magnet machines with slotless stator design. In *Electrical Machines Design Control and Diagnosis (WEMDCD), 2013 IEEE Workshop on*, pages 8–17, March 2013.

[40] A.E. Fitzgerald, Jr. Kingsley, C, and S.D. Umans. Electric machinery.

[41] Seok-Hee Han, T.M. Jahns, W.L. Soong, M.K. Guven, and M.S. Illindala. Torque ripple reduction in interior permanent magnet synchronous machines using stators with odd number of slots per pole pair. *Energy Conversion, IEEE Transactions on*, 25(1):118–127, March 2010.

[42] A.M. EL-Refaie. Fractional-slot concentrated-windings synchronous permanent magnet machines: Opportunities and challenges. *Industrial Electronics, IEEE Transactions on*, 57(1):107–121, Jan 2010.

[43] M. Diana, P. Guglielmi, and A.Vagati. A novel multi-n-phase machine model. In *International Conference on Electrical Machines (ICEM 16)*, 2016.

[44] Florence Libert and Juliette Soulard. Investigation on pole-slot combinations for permanent-magnet machines with concentrated windings.

[45] B. Aslan, E. Semail, J. Korecki, and J. Legranger. Slot/pole combinations choice for concentrated multiphase machines dedicated to mild-hybrid applications. In *IECON 2011 - 37th Annual Conference on IEEE Industrial Electronics Society*, pages 3698–3703, Nov 2011.

[46] Z. Q. Zhu, M. L. Mohd Jamil, and L. J. Wu. Influence of slot and pole number combinations on unbalanced magnetic force in pm machines with diametrically asymmetric windings. *IEEE Transactions on Industry Applications*, 49(1):19–30, Jan 2013.

[47] https://www.hbm.com/en. 2017. *In: On-line available*, 153(4):535 – 543, July 2017.

[48] R. Ruffo, V. Cirimele, M. Diana, M. Khalilian, A. La Ganga, and P. Guglielmi. Sensorless control of the charging process of a dynamic inductive power transfer system with interleaved nine-phase boost converter. *IEEE Transactions on Industrial Electronics*, pages 1–1, 2018.

[49] R. Burkart and J.W. Kolar. Component cost models for multi-objective optimizations of switched-mode power converters. In *Energy Conversion Congress and Exposition (ECCE), 2013 IEEE*, pages 2139–2146, Sept 2013.

[50] G. J. Su and L. Tang. A segmented traction drive system with a small dc bus capacitor. In *2012 IEEE Energy Conversion Congress and Exposition (ECCE)*, pages 2847–2853, Sept 2012.

[51] J. S. Kim and S. K. Sul. New control scheme for ac-dc-ac converter without dc link electrolytic capacitor. In *Power Electronics Specialists Conference, 1993. PESC '93 Record., 24th Annual IEEE*, pages 300–306, Jun 1993.

[52] J.W. Kolar and S.D. Round. Analytical calculation of the rms current stress on the dc-link capacitor of voltage-pwm converter systems. *Electric Power Applications, IEE Proceedings*, 153(4):535 – 543, July 2006.

[53] M. L. Gasperi. Life prediction modeling of bus capacitors in ac variable-frequency drives. *IEEE Transactions on Industry Applications*, 41(6):1430–1435, Nov 2005.

[54] P. D. Ziogas, Y. G. Kang, and V. R. Stefanovic. Rectifier-inverter frequency changers with suppressed dc link components. *IEEE Transactions on Industry Applications*, IA-22(6):1027–1036, Nov 1986.

[55] M. Lazzari, F. Profumo, A. Tenconi, and G. Grieco. Analytical and numerical computation of rms current stress on the dc link capacitor in multiphase voltage source pwm inverters. *EPE 2001*, 2001.

[56] F. D. Kieferndorf, M. Forster, and T. A. Lipo. Reduction of dc-bus capacitor ripple current with pam/pwm converter. *IEEE Transactions on Industry Applications*, 40(2):607–614, March 2004.

[57] B. S. Umesh and K. Sivakumar. Pole-phase modulated multiphase induction motor drive with reduced torque ripple and improved dc link utilization. *IEEE Transactions on Power Electronics*, 32(10):7862–7869, Oct 2017.

[58] B. Basler, T. Greiner, and P. Heidrich. Reduction of dc link capacitor stress for double three-phase drive unit through shifted control and phase displacement. In *2015 IEEE 11th International Conference on Power Electronics and Drive Systems*, pages 887–889, June 2015.

[59] D. Glose and R. Kennel. Carrier-based pulse width modulation for symmetrical six-phase drives. *IEEE Transactions on Power Electronics*, 30(12):6873–6882, Dec 2015.

[60] B. Basler and T. Greiner. Power loss reduction of dc link capacitor for multiphase motor drive systems through shifted control. In *2015 9th International Conference on Power Electronics and ECCE Asia (ICPE-ECCE Asia)*, pages 2451–2456, June 2015.

[61] G. J. Capella, J. Pou, S. Ceballos, G. Konstantinou, J. Zaragoza, and V. G. Agelidis. Enhanced phase-shifted pwm carrier disposition for interleaved voltage-source inverters. *IEEE Transactions on Power Electronics*, 30(3):1121–1125, March 2015.

[62] S. Haghbin and T. Thiringer. Dc bus current harmonics of a three-phase pwm inverter with the zero sequence injection. In *2014 IEEE Transportation Electrification Conference and Expo (ITEC)*, pages 1–6, June 2014.

[63] Chiao-Chien Lin and Ying-Yu Tzou. An innovative multiphase pwm control strategy for a pmsm with segmented stator windings. In *Applied Power Electronics Conference and Exposition (APEC), 2015 IEEE*, pages 270–275, March 2015.

[64] A. Patzak and D. Gerling. Design of a multi-phase inverter for low voltage high power electric vehicles. In *Electric Vehicle Conference (IEVC), 2014 IEEE International*, pages 1–7, Dec 2014.

[65] H. Wen, W. Xiao, X. Wen, and P. Armstrong. Analysis and evaluation of dc-link capacitors for high-power-density electric vehicle drive systems. *IEEE Transactions on Vehicular Technology*, 61(7):2950–2964, Sept 2012.

[66] A. Vagati, M. Pastorelli, G. Francheschini, and S. C. Petrache. Design of low-torque-ripple synchronous reluctance motors. *IEEE Transactions on Industry Applications*, 34(4):758–765, Jul 1998.

[67] N. Bianchi, A. Castagnini, P. S. Termini, and G. Secondo. The nature of the torque ripple in fractional-slot synchronous pmarel machines. In *2016 IEEE Energy Conversion Congress and Exposition (ECCE)*, pages 1–8, Sept 2016.

[68] A Vagati. Synchronous reluctance electrical motor having a low torque-ripple design, 07 1995.

[69] A. Tessarolo, M. Mezzarobba, and M. Degano. Analytical calculation of air-gap armature reaction field including slotting effects in fractional-slot concentrated-coil spm multiphase machines. In *2011 International Conference on Power Engineering, Energy and Electrical Drives*, pages 1–6, May 2011.

[70] A. Tessarolo and M. Mezzarobba. On the computation of rotor losses through a set of harmonic finite element analyses in fractional-slot concentrated-coil permanent-magnet machines. In *2011 IEEE EUROCON - International Conference on Computer as a Tool*, pages 1–4, April 2011.

[71] A. Tessarolo, F. Luise, S. Pieri, A. Benedetti, M. Bortolozzi, and M. De Martin. Design for manufacturability of an off-shore direct-drive wind generator: An insight into additional loss prediction and mitigation. *IEEE Transactions on Industry Applications*, 53(5):4831–4842, Sept 2017.

[72] A. Tessarolo, M. Bortolozzi, and M. Mezzarobba. On the validity of the harmonic superposition principle for computing rotor eddy current losses in permanent magnet machines. In *2012 XXth International Conference on Electrical Machines*, pages 1369–1373, Sept 2012.

[73] G. Pellegrino, P. Guglielmi, A. Vagati, and F. Villata. Core losses and torque ripple in ipm machines: Dedicated modeling and design tradeoff. *IEEE Transactions on Industry Applications*, 46(6):2381–2391, Nov 2010.

[74] I. Marongiu and A. Vagati. Improved modelling of a distributed anisotropy synchronous reluctance machine. In *Conference Record of the 1991 IEEE Industry Applications Society Annual Meeting*, pages 238–243 vol.1, Sept 1991.

[75] R. Ruffo and P. Guglielmi. Simple parameters estimation and precise overvoltage simulation in long cable connected drives. In *IECON 2016 - 42nd Annual Conference of the IEEE Industrial Electronics Society*, pages 4362–4367, Oct 2016.